

**Creating a dense sample of ultracold YO molecules in an  
optical lattice**

by

**Yewei Wu**

B.S., Tsinghua University, 2014

M.S., University of Colorado, 2017

A thesis submitted to the  
Faculty of the Graduate School of the  
University of Colorado in partial fulfillment  
of the requirements for the degree of  
Doctor of Philosophy  
Department of Physics  
2021

Committee Members:

Jun Ye, Chair

James K. Thompson

David J. Nesbitt

Konrad W. Lehnert

Gregory B. Rieker

Wu, Yewei (Ph.D., Physics)

Creating a dense sample of ultracold YO molecules in an optical lattice

Thesis directed by Prof. Jun Ye

Ultracold molecules offer a new platform for quantum chemistry, strongly correlated quantum systems, quantum information processing, and precision tests of fundamental physics. Their rich internal structure and strong anisotropic dipolar interaction provide the tools for new physics and chemistry studies. However, due to the additional ro-vibrational degrees of freedom, controlling of molecules becomes very challenging. The past few years have witnessed a rapid progress of laser cooling and trapping of molecules realized by several groups around the world.

In this thesis, we show an enhanced slowing efficiency for YO molecular beams by an improved laser coupling regime. With enough number of slowed molecules, we demonstrate the first creation of RF and DC MOT of YO, which makes YO the first oxide molecule trapped in MOT. We systematically study various types of MOT and the gray molasses cooling of YO, achieving a temperature of  $4 \mu\text{K}$ , 25 times colder than the Doppler limit. The robust cooling against large magnetic field allows us to develop a novel scheme to significantly compress the molecular cloud below mm. With a compressed cloud, we are able to efficiently load molecules into a 1D optical lattice for further cooling and compression. A factor of 220 and 95 increase in density and phase space density are realized compared to the cloud before loading, creating a molecular sample with the highest phase space density to date by direct laser cooling. By adiabatically ramping down the lattice depth,  $1.0(2) \mu\text{K}$  is achieved, which is the lowest temperature realized by direct laser cooling of molecules. With a long lattice lifetime of 850(70) ms, the study of YO-YO interaction is within reach.

## Dedication

To Claire.

## Acknowledgements

There are so many people who made this work possible. Although it's guaranteed that I'm not able to show my appreciation in a few sentences, I'll still give it a try.

I would like to thank first and foremost my advisor, Jun Ye, for his guidance and mentorship. He not only helped me on research, but also guide me to think and work as a physicist. Jun provides a great science environment for every young graduate student to grow in his lab. His passion, optimism, energy and knowledge of science have a profound impact on everyone, which is the key to our experimental success. Somehow, he could always manage to get enough funding to support all of our brave ideas. Apparently, no one has found his treasure chest yet.

I also had a great team working on the YO experiment. When I joined the group, I had a short overlap with Bo Yan, Mark Yeo and Matt Hummon. Bo Yan is an enthusiastic and interesting person. He always had a smile on his face and would encourage everyone when the experiment wasn't working properly. Mark Yeo is an expert in frequency comb and dye laser, without which the experiment couldn't continue at all. Matt Hummon is an excellent teacher who showed me how all apparatus work in the lab. For the most part of my Ph.D., I had the privilege of working with Alejandra L. Collopy, Shiqian Ding and Ian A. Finneran. Alejandra L. Collopy was instrumental in building up the 3D MOT apparatus. She designed the first RF MOT of YO and solved lots of experimental problems. Shiqian Ding was the game changer of the experiment. He always had his eye open on every details and was brave enough for new upgrades, without which the experiment couldn't have proceeded smoothly. I want to say a big thank you to you for all these years and wish you best of luck in Tsinghua. Ian A. Finneran is a true microwave expert that could generate

all crazy microwaves to fry our molecules. It's unfortunate that I'm unable to use your circuits for our SWAP MOT idea but I'm sure the next generation would benefit from all your works. Justin Burau is the young graduate student in the lab who became really experienced in the past two years. I'm confident to leave the experiment to him and I believe he'll bring the experiment to a crazy high level. Also, I would like to welcome Kameron Mehling who just joined the lab last year. He is a good talker, body builder and very energetic person. He has a curious mind which is the prerequisite for a good scientist and I really enjoy all his questions.

Ye group has people working on various front of science. It's really helpful to share knowledges, ideas and equipment with them. I'd like to thank Hao Wu, David Reens, Tim Langen, Chengyi Luo and Lee Liu for great advice and useful discussions.

I must also thank all the fantastic staff here in JILA. All of our experiment apparatuses have the hard work of our machinists and electronic engineers. Thanks to Hans Green, Todd Asnicar, Kim Hagen, Kyle Thatcher, Calvin Schwadron, James Urich, Terry Brown, Carl Sauer, J.R. Raith and David Alchenberger.

I'd like to thank my family for their support and understanding. In particular, I'm really fortunate to meet my wife in Boulder, she has made me a better person. No matter what I decide to do, she is always behind me. I can't wait for our life together after graduation.

## Contents

<b>Chapter</b>	
<b>1</b> Introduction	1
1.1 Why Cold Polar Molecules? . . . . .	1
1.2 Productions of Ultracold Polar Molecules . . . . .	2
1.3 About This Thesis . . . . .	3
<b>2</b> YO Level Structure	5
2.1 Molecular Structure of Diatomic Molecules . . . . .	5
2.1.1 Angular Momentum Coupling-Hund's Cases . . . . .	6
2.1.2 Labeling of Molecular States . . . . .	7
2.1.3 Vibrational Energy Levels . . . . .	8
2.1.4 Rotational Energy Levels . . . . .	8
2.1.5 $\Lambda$ Doubling . . . . .	8
2.2 Interaction with External Fields . . . . .	9
2.2.1 Under Magnetic Field - Zeeman Effect . . . . .	9
2.2.2 Interaction with Laser Beams . . . . .	9
2.3 YO . . . . .	11
<b>3</b> Cryogenic Buffer Gas Source	14
3.1 $Y_2O_3$ Two-stage Buffer Gas Source . . . . .	14
3.1.1 Charcoal Sorbs . . . . .	16

3.2	Y <sub>2</sub> O <sub>3</sub> Single-stage Buffer Gas Source . . . . .	18
3.2.1	Cell Heating . . . . .	19
3.2.2	Coating Cell Surface with Y <sub>2</sub> O <sub>3</sub> Nanopowder . . . . .	19
3.2.3	Cell Performance . . . . .	22
3.3	Y + O <sub>2</sub> (O <sub>3</sub> ) Source . . . . .	23
3.4	Next Generation of YO Source . . . . .	25
3.4.1	Molecule Yield Fluctuation . . . . .	25
3.4.2	Limited Pumping and Accessibility . . . . .	27
3.4.3	1 K System . . . . .	27
<b>4</b>	<b>Laser Slowing</b>	<b>31</b>
4.1	Laser Slowing YO . . . . .	31
4.2	Γ/13 Slowing Scheme . . . . .	32
4.2.1	Γ/13 Repumping Scheme . . . . .	32
4.2.2	Detection Method . . . . .	34
4.2.3	Performance . . . . .	35
4.3	Γ/8 Slowing Scheme with N=2 Decoupled . . . . .	35
4.3.1	Repumping Scheme . . . . .	36
4.3.2	Spectroscopy for Γ/8 Scheme . . . . .	37
4.3.3	Slowing Setup and Performance . . . . .	37
4.4	Slowing Scheme with A' <sup>2</sup> Δ <sub>3/2</sub> Repumped . . . . .	41
<b>5</b>	<b>3D Magneto-Optical Trap of Yttrium Monoxide</b>	<b>42</b>
5.1	Magneto-optical Trapping Theory . . . . .	42
5.1.1	Type II MOT . . . . .	44
5.2	Experiment Setup for RF MOT . . . . .	44
5.2.1	RF MOT Coils . . . . .	44
5.2.2	First 3D RF MOT Coil Design . . . . .	45

5.2.3	New RF MOT Coil Design . . . . .	47
5.2.4	Driving RF Coil . . . . .	47
5.2.5	Cooling the Coil . . . . .	48
5.2.6	Reducing the Scattered Light . . . . .	49
5.2.7	Detection system for RF MOT . . . . .	50
5.3	RF MOT Performance . . . . .	51
5.3.1	1D RF MOT . . . . .	51
5.3.2	3D RF MOT . . . . .	52
5.4	Molecule Loss by Parity Mixing . . . . .	56
5.4.1	N=3 Spectroscopy . . . . .	58
5.4.2	N=3 Performance . . . . .	58
5.5	DC MOT . . . . .	59
5.5.1	DC MOT Performance . . . . .	60
5.5.2	Detailed DC MOT Characterization . . . . .	62
5.5.3	Collision with Background Gas in DC MOT . . . . .	64
5.5.4	Remaining Issues in MOT Beams . . . . .	65
5.5.5	Limited MOT Lifetime at High Magnetic Field Gradient . . . . .	66
5.5.6	New Trapping Scheme . . . . .	67
<b>6</b>	<b>Sub-Doppler Cooling and Compressed Trapping of Molecules</b>	<b>69</b>
6.1	Gray Molasses Cooling . . . . .	69
6.1.1	Gray Molasses Cooling Theory . . . . .	70
6.1.2	Gray Molasses Cooling of YO . . . . .	71
6.2	$\Lambda$ -Enhanced Gray Molasses Cooling . . . . .	73
6.2.1	$\Lambda$ -Enhanced Gray Molasses Cooling Theory . . . . .	73
6.2.2	$\Lambda$ -Enhanced Gray Molasses Cooling of YO . . . . .	74
6.3	Compressed Trapping of YO . . . . .	78



6.3.1	Gray Molasses Cooling with Magnetic Field . . . . .	78
6.3.2	Robust Cooling with Magnetic Field . . . . .	79
6.3.3	A Novel Compression Method . . . . .	81
<b>7</b>	<b>Optical Trapping of Molecules</b>	<b>83</b>
7.1	Optical Dipole Trap(ODT) Theory . . . . .	83
7.1.1	Molecule Interacts with Laser . . . . .	84
7.1.2	Gaussian Beam Profile . . . . .	85
7.2	689 nm ODT . . . . .	87
7.2.1	Experiment Setup . . . . .	87
7.2.2	Discussion . . . . .	88
7.3	1064 nm ODT . . . . .	89
7.3.1	Experiment Setup . . . . .	89
7.3.2	Loading and Cooling inside ODT . . . . .	93
7.3.3	ODT Lifetime . . . . .	94
7.4	1064 nm Optical Lattice . . . . .	95
7.4.1	Loading and Cooling inside Lattice . . . . .	96
7.4.2	Lattice Characterization . . . . .	97
7.4.3	Molecule Loss with Low Intensity GMC Beams . . . . .	99
7.4.4	Heating at Low Intensity . . . . .	102
7.4.5	Ramping Down the Lattice . . . . .	103
7.4.6	Noise-induced Heating . . . . .	105
	<b>Bibliography</b>	<b>107</b>
	<b>Appendix</b>	
<b>A</b>	<b>YO Molecular Structures and Spectroscopy</b>	<b>119</b>

A.1	$X^2\Sigma^+ \rightarrow A^2\Pi_{1/2}$ Transition(v=0)	119
A.2	$X^2\Sigma^+ \rightarrow A'^2\Delta_{3/2}$ Transition	122
<b>B</b>	Dye Lasers - How to Make it Happy	124
B.1	Why Dye Laser	124
B.2	Sirah Matisse DR 2 Laser	125
<b>C</b>	Magnetic Coil	127
<b>D</b>	Compression Timing Diagram	131

## Figures

### Figure

2.1	Hund's Cases (a) and (b).	6
2.2	Ground State Zeeman Structure.	10
2.3	YO Energy Levels.	12
3.1	First Version of Cryogenic Buffer Gas Cell.	15
3.2	Schematic of Buffer Gas Cell.	17
3.3	Performance of Single vs Two Stage Cell.	18
3.4	Cell Heating Effect.	20
3.5	Ablation Target and In-vacuum Shutter.	20
3.6	Coating Cell with YO Nanopowder.	21
3.7	Cell Performance with/out Nanopowder.	21
3.8	Coating on Ablation Window.	22
3.9	Modified Cell with $O_2/O_3$ .	23
3.10	Comparison of $Y+O_2(O_3)$ with $Y_2O_3$ Cell.	24
3.11	Molecule Yield at Different Temperature.	26
3.12	Measurement of Molecule Yield at Different Temperature.	26
3.13	Limited Pumping and Accessibility.	28
3.14	Exploded-view of 1 K Cell.	29
3.15	1 K Pot Drawing.	30

4.1	$\Gamma/13$ Slowing Scheme. . . . .	33
4.2	Doppler Sensitive Detection Method. . . . .	34
4.3	Slowing Result with Two Stage Cell. . . . .	35
4.4	Slowing Improvement by Increasing Deceleration. . . . .	36
4.5	$\Gamma/8$ and $\Gamma/5$ Repumping Scheme. . . . .	38
4.6	Spectroscopy for $\Gamma/8$ Scheme. . . . .	38
4.7	Slowing Setup. . . . .	39
4.8	$\Gamma/8$ Performance. . . . .	40
4.9	Slowing Scheme with $A'^2\Delta_{3/2}$ Repumped. . . . .	41
5.1	Type I and Type II MOT. . . . .	43
5.2	Different MOT Coil Designs. . . . .	46
5.3	RF Coil Electronics. . . . .	47
5.4	RF Coil Performance. . . . .	48
5.5	Custom Vacuum Viewport. . . . .	49
5.6	MOT Detection Layout. . . . .	51
5.7	1D RF MOT Performance. . . . .	52
5.8	3D RF MOT Setup. . . . .	53
5.9	Overslowing. . . . .	54
5.10	RF MOT Characterisation. . . . .	55
5.11	RF MOT Temperature. . . . .	55
5.12	MOT Lifetime versus Power. . . . .	57
5.13	Parity Mixing. . . . .	58
5.14	N=3 Performance. . . . .	59
5.15	DC MOT Setup. . . . .	60
5.16	DC MOT Contribution. . . . .	61
5.17	DC RF MOT Comparison. . . . .	62

5.18	MOT at Different Intensities. . . . .	63
5.19	MOT at Different Magnetic Field and Detuning. . . . .	63
5.20	Limit of MOT Lifetime. . . . .	64
5.21	MOT Shape Affected by Beam Alignment. . . . .	65
5.22	Compressed MOT. . . . .	66
5.23	New Trapping Scheme . . . . .	68
6.1	Sub-Doppler Cooling Theory. . . . .	71
6.2	DC MOT Setup. . . . .	72
6.3	VSCPT Theory. . . . .	73
6.4	Temperature vs $\delta$ in Small Range. . . . .	74
6.5	Temperature vs $\delta$ in Large Range. . . . .	75
6.6	Raman Detuning Scan Different Parameters. . . . .	77
6.7	Characterisation of GMC. . . . .	78
6.8	Cancellation coil. . . . .	79
6.9	B Field Cancellation. . . . .	79
6.10	Temperature under Bias Magnetic Field. . . . .	80
6.11	Compression of Molecular Cloud. . . . .	82
7.1	Trap Depth vs Wavelength . . . . .	85
7.2	Gaussian Beam Profile and Light Shift . . . . .	86
7.3	Trap Tilt . . . . .	87
7.4	1064 nm Beam Preparation . . . . .	88
7.5	Fiber End Cap . . . . .	89
7.6	ODT and Lattice Setup . . . . .	91
7.7	Trapping Beam Alignment . . . . .	92
7.8	ODT Optimization . . . . .	92
7.9	ODT with Different Raman Detuning $\delta$ . . . . .	93

7.10 ODT with Different Intensity . . . . .	94
7.11 ODT Lifetime . . . . .	95
7.12 Lattice Loading Parameters . . . . .	97
7.13 Lattice Trapping Frequency . . . . .	98
7.14 Lattice parameters. . . . .	99
7.15 Lattice Loss. . . . .	100
7.16 Lattice loss curve . . . . .	101
7.17 Lattice Heating at Low Intensity. . . . .	102
7.18 Ramping Down the Lattice. . . . .	104
7.19 Relative Intensity Noise Spectrum and E-folding Time. . . . .	106
A.1 N=0 to J=0.5 Spectroscopy. . . . .	119
A.2 N=1 to J=0.5 Spectroscopy. . . . .	120
A.3 N=1 to J=1.5 Spectroscopy. . . . .	120
A.4 N=2 to J=1.5 Spectroscopy. . . . .	120
A.5 N=2 to J=2.5 Spectroscopy. . . . .	121
A.6 N=3 to J=2.5 Spectroscopy. . . . .	121
A.7 Delta State Lifetime. . . . .	122
A.8 Delta State Spectroscopy. . . . .	123
B.1 Dye Layout . . . . .	125
C.1 Calculated Coil Performances. . . . .	127
D.1 Compression Timing Diagram. . . . .	131

# Chapter 1

## Introduction

The study of ultracold atoms has been a major topic in the atomic physics community for more than 4 decades since the advent of laser cooling and trapping techniques. The study of trapping and cooling atoms to ultralow temperatures has resulted in several Nobel Prizes. Ultracold atoms provide a powerful platform for studying quantum degenerate gases [1, 2], strongly correlated systems [3], quantum information [4, 5, 6, 7], quantum sensing [8] and ultra-precise atomic clocks [9].

### 1.1 Why Cold Polar Molecules?

Some atoms have optimal structures, making them relatively easy to cool and trap. The weak long range interaction makes them an ideal candidate for metrology applications. Compared with atoms, molecules have rich internal structure and strong anisotropic interaction due to the body fixed electric-dipole moment. Therefore, ultracold polar molecules [10, 11] provide opportunities for many important applications ranging from quantum simulation [12, 13, 14, 15, 16] to precision tests of fundamental physics [17, 18]. Some of these applications, particularly in quantum information processing [12, 13, 19], many body quantum system simulation [20] and quantum-state-controlled chemistry [21, 22], demand a high phase space density. As a result, the generation of ultracold molecules has become a popular topic and lots of molecules have been cooled and trapped over the past decade.

Controlling how molecules interact with each other has become increasingly popular in recent years. For example, collisional losses in ultracold gases of alkali-metal dimers [23, 24, 25, 26] is

poorly understood. The recent observation of suppression of loss as KRb Fermi molecules enter quantum degeneracy also awaits theory explanations. Theory predicts the presence of a reaction complex, in the process called sticky collisions [27]. It's only recently that bimolecular reactions and intermediate complex have been observed directly [28]. More experiments are also focusing on state controlled collisions [21, 29]. By controlling external fields [30], reactions can be enhanced or suppressed [31, 32]. For example, the elastic-inelastic ratio can be tuned by the external field to enhance the evaporation cooling efficiency, which has led to a degenerate gas in 2D [33].

Molecules are also great tools for precision measurements, particularly in searching for the permanent electric dipole moments of the electron (eEDM) [34, 35, 36, 37]. Based on the Standard Model, the weak interaction does not preserve the CP-symmetry, implying an uneven charge distribution over the electron, which means the electron has a permanent electric dipole moment. The discovery of an eEDM would imply the violation of time reversal invariance. Compared to atoms [34], polar molecules can enhance the detection sensitivity due to its large internal electric field. The current upper bound of the eEDM is set by the measurements using polar molecules [36, 37, 38, 39].

## 1.2 Productions of Ultracold Polar Molecules

The productions of atoms and molecules for cooling experiments are fundamentally different. For example, alkali atoms are initially produced from a metal dispenser, where the dispenser can be heated to produce a high vapor pressure. This atomic vapor can be used directly for laser cooling. As for molecules, due to the thermal distribution, they are distributed among many rotational and vibrational states separated by tens of GHz and several THz. These large separations require multiple lasers to address molecules across all these states, which is an impossible mission. Therefore, the goal is to produce a high flux of molecules at a single quantum state. This is accomplished in two ways: indirect cooling, where molecules are assembled from ultracold atoms, and direct cooling, where cooling is directly applied on a molecular species. With indirect methods, several ultracold molecules have been produced [23, 24, 25, 26, 40, 41, 42]. Among these molecules, KRb has been brought to quantum degeneracy very recently [43] and has enabled the study of



dipolar evaporation [33] and collisional shielding [44]. Besides assembling bi-alkalis, there has been a rapid progress in direct laser cooling and trapping of molecules. A typical and general method to create cold molecules is called buffer gas cooling [45]. This technique relies on the elastic collisions between molecules and a buffer gas to cool both internal and external degrees of freedom of the molecules. With helium as the buffer gas, most molecules can be cooled such that the majority of the population resides at the lowest ro-vibraitonal states. Nowadays, the cryogenic buffer gas cell has become the standard source for direct cooling and trapping of molecules [45, 46].

With molecules generated at  $\sim$ K from the buffer gas source, there are many ways to further cool the molecules, which could be summarized in two categories depending on the evolution of the phase space density. One "cooling" technique doesn't change the phase space density, it works by periodically converting the kinetic energy into potential energy, such as in a Stark/Zeeaman decelerator [47, 48, 49, 50, 51] and centrifugal decelerator [52]. Direct laser cooling is another technique, where the entropy is taken away by the photons. However, laser cooling is limited to molecules with diagonal transitions [53], optimized angular momentum selection rules [54] and attainable high power lasers for the transition wavelength. Starting from two proposed papers on vibration and rotation closures for cooling [53, 54], the past few years have witnessed a rapid advancement in laser cooling and trapping molecules. Magneto-optical traps have been demonstrated for diatomic molecules such as SrF [55], CaF [56, 57], YO [58, 59] and even polyatomic molecules CaOH [60]. Sisyphus-type gray molasses cooling(GMC) together with velocity-selective coherent population trapping was used to cool molecules to  $\mu$ K [59, 61, 62]. Recently, these molecules have been loaded into the magnetic traps [63, 64, 65], optical dipole traps [61] and optical tweezer arrays [66, 67, 68] for collisional studies.

### 1.3 About This Thesis

In this thesis, we will discuss the production, slowing, trapping and cooling of YO. In Chapter 2, we will introduce the molecular structure and basic properties of YO relevant to this work. Buffer gas cooling of YO and various upgrades are detailed in Chapter 3. Chapter 4 will discuss different

slowing mechanisms. In Chapter **5**, we compare RF and DC MOT performances. Chapter **6** will detail the sub-Doppler cooling of YO and the special compression protocol tailored by the unique YO structure. Chapter **7** will cover the loading and cooling into a 1-D optical lattice together with the creation of the molecular sample with the highest phase space density and the lowest temperature by direct laser cooling.

## Chapter 2

### YO Level Structure

Understanding the molecular structure and interaction with external fields is critical for slowing, cooling and trapping molecules [53]. Compared with atoms, "a diatomic molecule is one atom too many", said Arthur Schawlow. The extra atom in a diatomic molecule introduces two additional degrees of freedom, vibration and rotation, creating a complex structure. Therefore, only molecules with diagonal energy levels can be directly laser cooled. In this chapter, we introduce the molecular structure of diatomics and discuss the YO energy levels relevant to this work since it is been described in detail [69].

#### 2.1 Molecular Structure of Diatomic Molecules

In a diatomic molecule, the nuclei are much heavier than the electrons, thus their wave functions can be treated independently. In molecular spectroscopy, it means the electronic, vibrational and rotational degrees of freedom are decoupled and could be written in this approximation:

$$H = H_e + H_{vib} + H_{rot} + H_{SO} + H_{SR} + H_{HFS} + H_{\Lambda}$$

where  $H_e, H_{vib}, H_{rot}, H_{SO}, H_{SR}, H_{HFS}, H_{\Lambda}$  are the electronic, vibrational, rotational, spin-orbit, spin-rotation, hyperfine and  $\Lambda$ -doubling components of the Hamiltonian. These terms are generally well separated in energy scale, with electronic energy level spacings of 100's THz, vibration at THz level and rotational at the 10's of GHz level.

### 2.1.1 Angular Momentum Coupling-Hund's Cases

Diatomic molecules share some similarities with atoms, such as electronic spin  $\mathbf{S}$ , electronic orbital angular momentum  $\mathbf{L}$  and total angular momentum  $\mathbf{J}=\mathbf{L}+\mathbf{S}$ . Beyond this, diatomic molecules also have their rotational degrees of freedom. Unlike atoms with spherical symmetry, diatomic molecules possess axial symmetry with respect to their internuclear axis. Although most angular momenta are coupled to each other, it is useful to simplify the problem in cases where angular momenta are coupled in a prescribed order according to their coupling energy. The angular momentum coupling of diatomic molecules can be categorized into Hund's cases [70], proposed by Friedrich Hund. Here we describe the two most common cases, both of which describe the YO states related to this work.

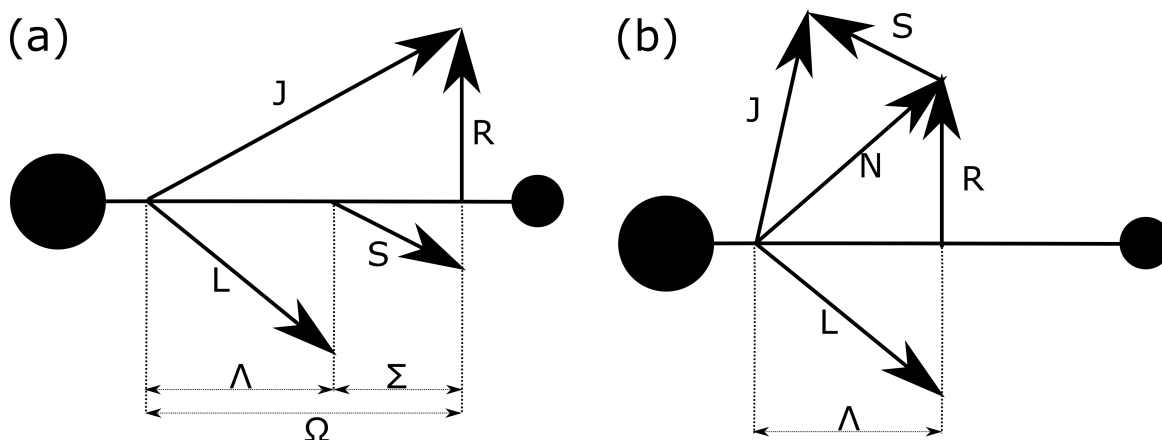


Figure 2.1: Angular momentum coupling diagram for Hund's cases (a) and (b).

#### 2.1.1.1 Hund's Case (a)

Figure 2.1 (a) shows the angular momentum coupling diagram for Hund's case (a). In this case, the electron orbital angular momentum  $\mathbf{L}$  is strongly coupled to the internuclear axis under the electrostatic interactions and electron spin  $\mathbf{S}$  is strongly coupled to  $\mathbf{L}$  through spin-orbit coupling. Their projections onto the internuclear axis are labeled as  $\Lambda$ ,  $\Sigma$  and the sum is  $\Omega$ . This cumulative projection then couples with the rotation of the nuclei  $\mathbf{R}$ , forming the total angular momentum

$\mathbf{J}=\mathbf{R}+\Omega$ . This case describes the  $A^2\Pi_{1/2}$  and  $A'^2\Delta_{3/2}$  states, two excited states of YO involved in our laser cooling scheme.

### 2.1.1.2 Hund's Case (b)

In Hund's case (b), shown in Figure 2.1 (b), electron orbital angular momentum  $\mathbf{L}$  still couples to the internuclear axis. However, the electron spin  $\mathbf{S}$  isn't coupled because the spin-orbit coupling is weak. Thus,  $\Lambda$  couples to  $\mathbf{R}$  to form  $\mathbf{N}=\mathbf{R}+\mathbf{L}$  and eventually coupled with  $\mathbf{S}$  to form  $\mathbf{J}=\mathbf{N}+\mathbf{S}$ . YO ground state  $X^2\Sigma^+$  is a special Hund case (b) as  $\mathbf{L}$  is zero. The electron  $\mathbf{S}$  and nuclear spin  $\mathbf{I}$  are strongly coupled by the Fermi contact interaction, forming an intermediate angular momentum  $\mathbf{G}=\mathbf{I}+\mathbf{S}$ . Then it couples with molecular rotation  $\mathbf{N}$  through spin-rotation interaction yielding  $\mathbf{F}=\mathbf{G}+\mathbf{N}$ .

### 2.1.2 Labeling of Molecular States

It is standard to denote electronic energy levels of diatomic molecules by letters, with X always denoting the ground state. Electronically excited states are labeled by capital letters(A,B,C...) in the order of the energy of the states. Sometimes, the letter ordering doesn't follow the energy levels when a lower state was found after the other states. In addition to the letter, electronic energy levels are labeled by the molecular notation

$${}^{2S+1}\Lambda_{|\Omega|}^{+/-}$$

where +/- denotes the reflection symmetry through an arbitrary plane along the internuclear axis. Similar to atomic states where  $J=0,1,2,3$  are labeled as S,P,D,F, molecular states with  $\Lambda=0,1,2,3$  are labeled as  $\Sigma, \Pi, \Delta, \Phi$ . Therefore, the electronic ground state of YO is labeled as  $X^2\Sigma^+$  and the "lowest" excited state is labeled as  $A^2\Pi_{1/2}$ . It is worth mentioning the lowest excited state is actually  $A'^2\Delta_{3/2}$ , and it is labeled as  $A'$  since it was discovered after the  $A^2\Pi_{1/2}$  state.

### 2.1.3 Vibrational Energy Levels

The vibrational levels can be approximated as a harmonic oscillator with additional terms representing the anharmonicity [71].

$$E_{vib} = \omega_e(v + \frac{1}{2}) - \omega_e x_e(v + \frac{1}{2})^2 + \omega_e y_e(v + \frac{1}{2})^3 + \dots$$

where  $v$  is the vibrational quantum number,  $\omega_e$  is the vibrational constant and  $x_e, y_e$  are anharmonic constants.

### 2.1.4 Rotational Energy Levels

The rotation of a diatomic molecule can be approximated as a rigid rotor with additional terms representing the centrifugal distortion. It can be described as

$$E_{rot} = B_v R(R + 1) - D_v R^2(R + 1)^2 + H_v R^3(R + 1)^3 + \dots$$

where  $\mathbf{R}$  is the rotational quantum number, and  $B_v, D_v, H_v$  depend on vibrational level  $v$ .

$$B_v = B_e - \alpha_e(v + \frac{1}{2}) + \gamma_e(v + \frac{1}{2})^2 + \dots$$

These parameters represent the coupling between rotational and vibrational motion [72].

### 2.1.5 $\Lambda$ Doubling

In Hund's case (a), as  $\mathbf{L}$  may precess about the internuclear axis in two directions (clockwise / counter clockwise), its projection onto the internuclear axis can be  $\pm\Lambda$ . These two manifolds are degenerate if the molecule is not rotating, however, this degeneracy breaks down due to the molecular rotation. The splitting between these manifolds is called  $\Lambda$  doubling and it scales with  $J$ . For Hund's case (a) molecules in  ${}^2\Pi_{1/2}$  state, the  $\Lambda$  splitting is

$$|E_\Lambda| = (p + 2q)(J + 1/2)$$

where  $p, q$  are the  $\Lambda$  doubling parameters and the sign depends on the spin-orbit interaction.  $\Lambda$  doubling creates an opposite parity state close to the excited state. For example, the splitting

between  $A'^2\Delta_{3/2}$   $J' = 3/2(-)$  and  $J' = 3/2(+)$  state is so small ( $\sim 0.2$  MHz) that these two states are totally mixed, causing decays to unrepumped states. This will be discussed in Chapter 4.

## 2.2 Interaction with External Fields

### 2.2.1 Under Magnetic Field - Zeeman Effect

In the presence of an external magnetic field, the spectral line of an atom(molecule) splits into several components. These energy shifts are due to the Zeeman effect. The Hamiltonian is given by [71]

$$H_z = g_s\mu_B S \cdot B + g_L\mu_B L \cdot B - g_I\mu_N I \cdot B$$

where  $g_s \approx 2$ ,  $g_N \approx 1$ ,  $g_I \approx 5.6$ ,  $\mu_B$ ,  $\mu_N \approx \frac{\mu_B}{1836}$  are electron spin, orbit, nuclear g factors, Bohr magneton and nuclear magnetic moment. The Zeeman shifts of  $X^2\Sigma^+$  state are plotted in Figure 2.2.

The Zeeman shift of  $A^2\Pi_{1/2}$  is calculated to be

$$E_{z,\pm} = \pm \frac{1}{3}(g'_l - g_r^{\prime})\mu_B B_z M_F$$

where  $\pm$  refers to the parity of the  $\Lambda$  doublet. The  $g'_l$  and  $g_r^{\prime}$  parameters depend on  $\Lambda$  doubling parameters p and q as follows [73, 74]

$$g'_l = \frac{p}{2B_\Pi} \quad g_r^{\prime} = -\frac{q}{B_\Pi}$$

where  $B_\Pi$  is the rotational constant of  $A^2\Pi_{1/2}$  state. As we can see in Figure 2.2,  $F=1$ ,  $m_F=1$  states have the maximum Zeeman shift among all manifolds in  $A^2\Pi_{1/2}$  state, which is a factor of 15 smaller than the largest Zeeman shift in the  $X^2\Sigma^+$  ground state.

### 2.2.2 Interaction with Laser Beams

When a laser beam interacts with a molecule, the electric field of the light will cause a change of the molecular energy for different internal states. These molecular energy shifts due to the AC

fields are called AC Stark shifts, which will be detailed in Chapter 7. Here we review some basic parameters in molecule laser interactions.

Despite the complexity of the multi-state molecule, it is useful to use a simple rate model [75, 76] to predict some properties. In the model, there are  $n_g$  ground states that are directly coupled to  $n_e$  excited states, thus the steady-state scattering rate is

$$R_{sc} = \Gamma \frac{n_e}{(n_g + n_e) + 2\sum_{j=1}^{n_g} (1 + 4\Delta_j^2/\Gamma^2) I_{s,j}/I_j}, \quad I_{s,j} = \frac{\pi h c \Gamma}{3\lambda_j^3}$$

where  $\Gamma$ ,  $\Delta_j$ ,  $I_{s,j}$ ,  $\lambda_j$ ,  $I_j$  are excited state decay rate, single-photon detuning, two-level saturation intensity, light wavelength and intensity for transition  $j$ . Assuming all transitions have similar

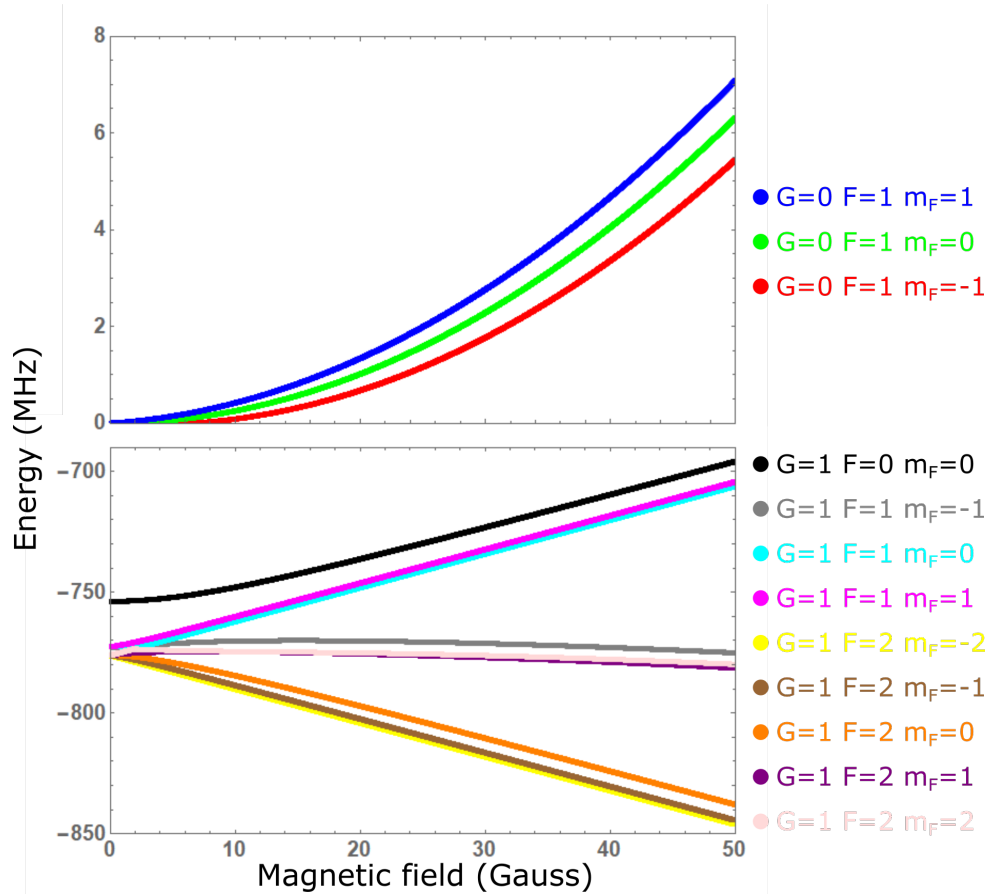


Figure 2.2: Zeeman structure of ground state  $X^2\Sigma^+$   $N=1$ .



values for  $\Delta$ ,  $I_s$  and total light intensity  $I_0$ , the equation can be simplified as

$$R_{sc} = \frac{\Gamma_{eff}}{2} \frac{s_{eff}}{1 + s_{eff} + 4\Delta^2/\Gamma^2}, \quad \Gamma_{eff} = \frac{2n_e}{n_g + n_e}\Gamma, \quad s_{eff} = \frac{2(n_g + n_e)}{n_g^2} \frac{I_0}{I_s}, \quad I_{s,eff} = \frac{n_g^2}{2(n_g + n_e)} I_s$$

where the  $\Gamma_{eff}$ ,  $s_{eff}$  and  $I_{s,eff}$  are effective linewidth, effective saturation rate and effective saturation intensity. One difficulty for slowing molecules is the low scattering rate caused by coupling with many ground states, which will be detailed in the Chapter 4.

## 2.3 YO

$^{89}\text{Y}^{16}\text{O}$  was chosen for several reasons. The main transition ( $X^2\Sigma^+ \rightarrow A^2\Pi_{1/2}$ ) is strong ( $\Gamma = 2\pi \times 4.8$  MHz), thus a fast photon scattering is possible. YO has very diagonal vibrational branchings such that molecules could scatter more than  $10^6$  photons while repumping only the three lowest vibrational states. All transition wavelengths are accessible in the visible region where commercial laser diodes or other systems are available. The dipole moment (4.45(7) D) [77], between the two rotation states in  $X^2\Sigma^+$ , is reasonable for dipolar interactions. Because of the strong coupling between nuclear and electronic spin, YO molecules aren't sensitive to external magnetic field. This magnetic insensitivity enables the spatial compression of molecular cloud and the realization of stable cooling, which will be detailed in Chapter 6. The relevant energy levels and decays for the discussion in this thesis are shown in Figure 2.3.

A large amount of prior spectroscopy [78, 79, 80, 81, 82, 83, 84, 85, 86, 87, 88] had been done on YO, which greatly simplified our spectroscopy measurement. The detailed energy levels have been discussed previously [69]. The spectroscopies taken by us are shown in Appendix A, so here we highlight only the most salient features.

The ground and excited state of the cycling transition are  $N=1(-)$  of  $X^2\Sigma^+$  and  $J' = 1/2(+)$  of  $A^2\Pi_{1/2}$ , while the rest of the states are repumped back using microwave or lasers. The  $N=1$  state is chosen to limit the decay back to  $N=1$  state. Decay to other rotational levels are forbidden by parity and angular momentum selection rules [54]. The vibrational branchings are addressed by repumping  $X^2\Sigma^+$   $v=1$  state directly back to the  $A^2\Pi_{1/2}$   $v=0$  state, while the  $X^2\Sigma^+$   $v=2$  state

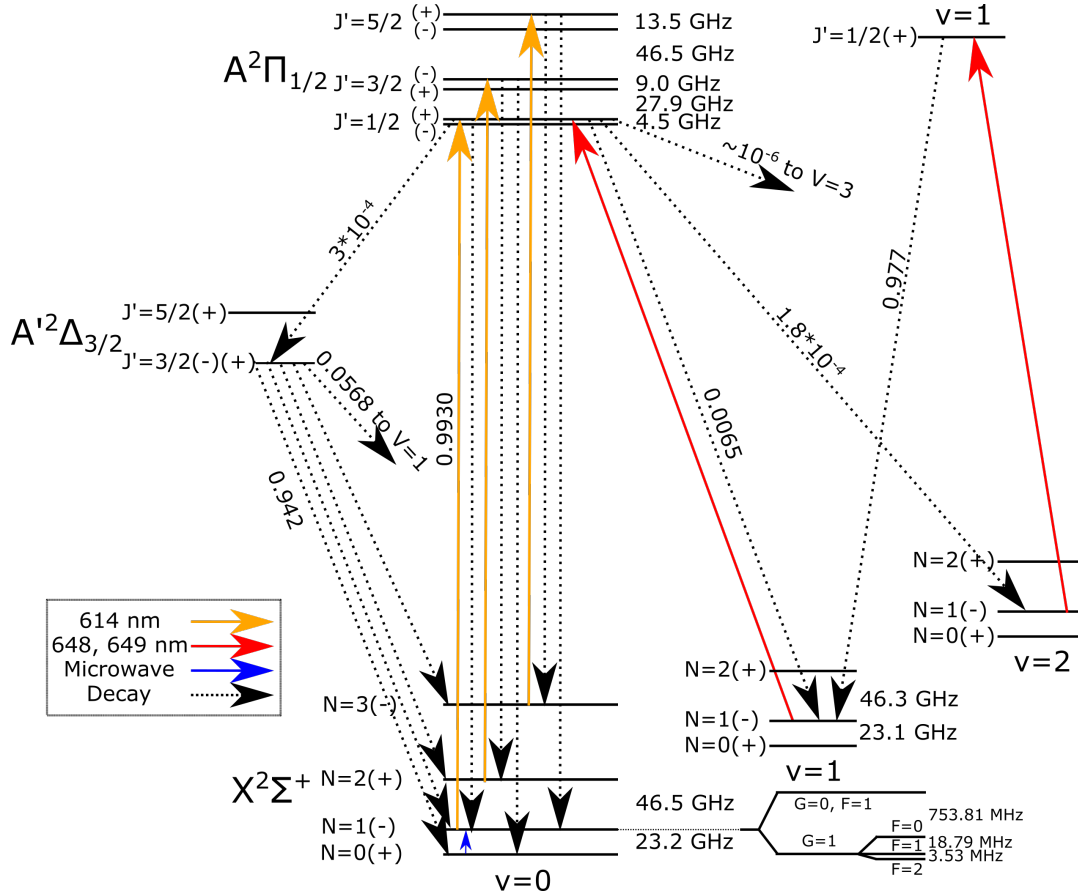


Figure 2.3: YO energy levels relevant in this thesis.

is repumped using a two step process. It first goes up to  $A^2\Pi_{1/2}$   $v=1$  state, which predominantly decays to the  $X^2\Sigma^+$   $v=1$  state, and then gets repumped back to  $v=0$  by  $v=1$  repumping laser. The nuclear spin gives rise to hyperfine structure, splitting the ground state into 4 manifolds. These hyperfine states are addressed with AOM sidebands.

Ideally, with only three lasers covering  $X^2\Sigma^+(v=0, N=1) \rightarrow A^2\Pi_{1/2}(v=0, J'=1/2)$ ,  $X^2\Sigma^+(v=1, N=1) \rightarrow A^2\Pi_{1/2}(v=0, J'=1/2)$  and  $X^2\Sigma^+(v=2, N=1) \rightarrow A^2\Pi_{1/2}(v=1, J'=1/2)$  transitions, YO could scatter more than  $10^6$  photons. However, molecules on the main excited state  $A^2\Pi_{1/2}$  has a  $\sim 3 \times 10^{-4}$  chance of decaying to an intermediate state  $A'^2\Delta_{3/2}(J'=3/2(-))$  and then decay to  $N=0(+)$  or  $N=2(+)$  of  $X^2\Sigma^+$  ground state. This two photon process flips the parity of the molecule, causing molecular loss after 3000 photon scatterings. This is not acceptable

even for molecular slowing, thus extra lasers and microwave are installed to plug the leak. Different repumping schemes will be discussed thoroughly in Chapter 4.

## Chapter 3

### Cryogenic Buffer Gas Source

To directly slow, cool and trap molecules, a cold and bright source is required. Molecules need to be prepared at the low temperature where most of them are residing in the lowest vibrational and rotational states. The two main sources to create cold molecules are supersonic expansion jets and buffer gas cooled beams. Supersonic expansion generates rotationally and vibrationally cold molecules but the forward velocity is hundreds of m/s, which requires lots of photon scatterings and a long slowing distance. These are hard to achieve for molecules without a very diagonal structure. Therefore, YO molecules are produced in a cryogenic buffer gas cell [45, 89]. In this chapter, I'll introduce basic principles of buffer gas cooling, briefly review our initial setup, introduce the enhancements and the new design for operating at lower temperature.

#### 3.1 $\text{Y}_2\text{O}_3$ Two-stage Buffer Gas Source

This is the first version we had for our 2D magneto-optical trap and rotational microwave mixing experiment [90, 91]. It's well documented previously [69], so here we introduce it very briefly.

Molecules are first generated by chemical reaction or laser ablation. In our case, the hot molecules from laser ablation are cooled by buffer gas helium to  $\sim 4\text{K}$  through elastic collisions. Both He and YO escape from the cell through a small aperture, while He is absorbed later by cryogenic charcoal sorbs. Depending on the buffer gas flow rates and cell geometry, different hydrodynamic regimes could be used to produce a YO beam [45]. It's also found that the forward velocity increases

linearly with gas flow, which is called the boosting effect [45]. This is not desirable for slowing the molecules. Thus, for this setup, we operate in the effusive regime to realize the slowest forward velocity of the molecules. A leaky second stage is also added to further slow down the molecules by creating an intermediate region where molecules experience several collisions on its way out.

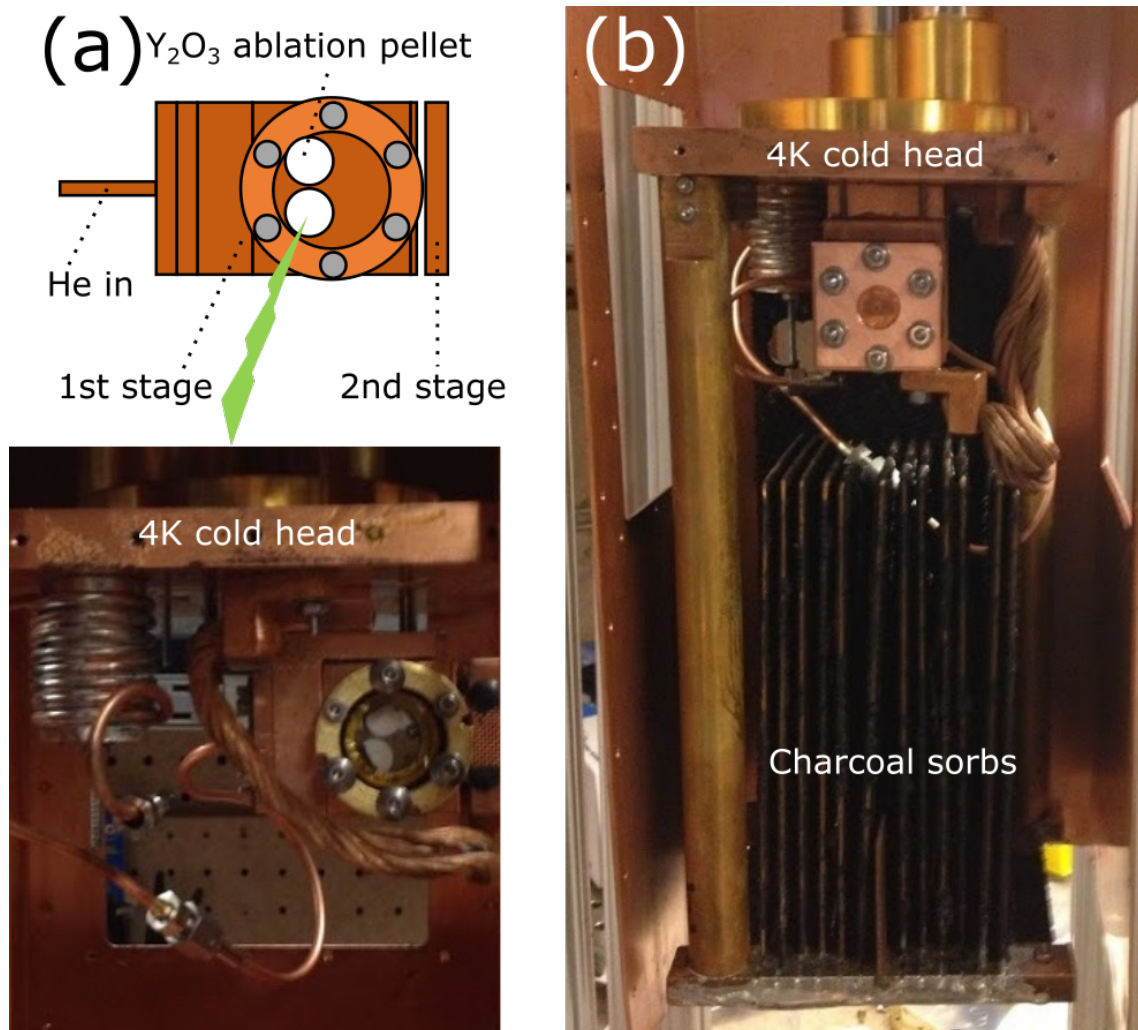


Figure 3.1: (a). Side view of two stage buffer gas cell. Helium is cooled to 4K by the copper bobbin before entering the cell. (b). Front view of two stage buffer gas cell and charcoal sorbs. Four charcoal panels are typically installed on the 4K cold head to absorb the unwanted helium.

Figure 3.1 shows the two stage buffer gas cell and charcoal sorbs underneath the cell. Typically, there are four charcoal panels installed on the 4K cold head to absorb the unwanted helium, which is not shown in this figure. The 1st stage of the cell is made out of a 1.5"  $\times$  1.5"  $\times$  1.25"

long oxygen-free high thermal conductivity (OFHC) copper block. The cell cavity is formed by two through holes of 0.85" diameter. The beam exists through a  $\sim 3$  mm aperture in the front. The second stage is made out of a 1.5"  $\times$  1.5"  $\times$  0.38" long OFHC copper block, standing off 2.8 mm away from the first stage. In addition, two rectangular vents on the side of the second stage provide additional leakage and the exit aperture is 9 mm in diameter. These leakages creates a intermediate region which holds a pressure between the 1st stage and low vacuum region. Our second stage is very similar to the design from the Doyle group in Harvard [92].

In order to keep the temperature at 4 K, cell and charcoal sorbs are directly anchored to the 4 K stage of a two-stage pulse tube cryocooler(Cryomech PT410). The cooling capacities at 40 K and 4.2 K stages are 40 W and 1 W. Therefore, if the cell and charcoals are directly exposed to vacuum chamber at room temperature, the heat load from black body radiation would be  $\sim 4.5$  W, which overwhelms the 4 K stage cooling capacity. We therefore apply two layers of radiation shielding, as shown in Figure 3.2. The inner shield is thermally anchored to the 4 K stage and the outer shield is thermally connected to the 40 K stage to block the radiation from the chamber at room temperature. The heat load on cell and charcoal sorbs is reduced from 4.5 W to 1.4 mW, negligible compared to the cooling capacity of the 4 K stage.

### 3.1.1 Charcoal Sorbs

As we mentioned above, both He and YO escape from the cell through a small aperture after elastic collisions. Helium exiting from the aperture needs to be pumped away immediately before colliding with YO again. However, enclosing the cell with radiation shields means that the conductance to the external turbo pumps is very low. The typical compression ratio for helium is also low, leading to a poor vacuum. Therefore, the buffer gas would build up and deteriorate the YO beam. The solution is to use cryogenic, activated charcoal as a cryopump [93]. When activated charcoal is cooled below 10 K, it becomes a cryopump for helium with  $\sim 10$  Liter/(s $\cdot$ cm<sup>2</sup>) pumping speed and could hold up to 1 liter(STP) of helium per gram. With activated charcoal(Spectrum Chemical C1221) epoxied(Loctite STYCAST 2850FT) to the inner surface of 4 K shield and extra

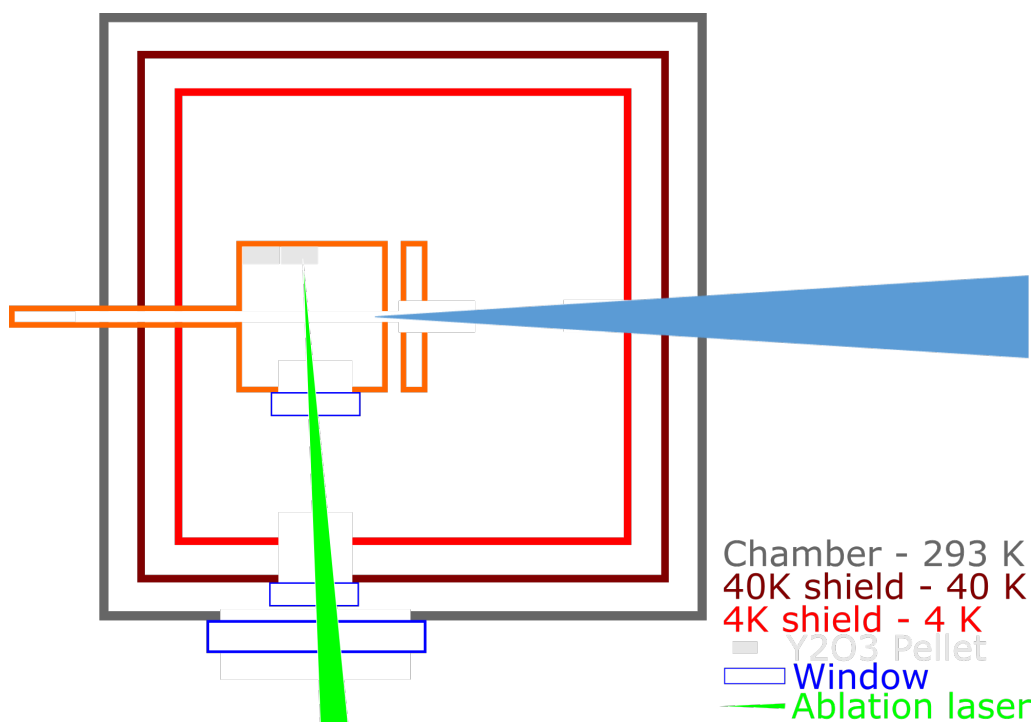


Figure 3.2: Top view of complete buffer gas cell setup.

4 K panels, as shown in Figure 3.1 (b), we achieve a pumping speed of  $\sim 100$  L/s and it should last for weeks under normal gas loads [94, 95]. If the charcoals are saturated with helium, it's necessary to warm up the sorbs above  $\sim 35$  K [96] and pump out the desorbed helium with a mechanical pump.

Initially, our fresh cell worked only for  $\sim 30$  minutes before a warm up, which is much shorter than the estimated runtime we mentioned above. It's because our 4 K enclosure wasn't covered nicely thus the sorb regenerated itself when the desorbing helium bounced off a surface which was significantly hotter than the sorb. A hot helium atom can hit the sorb and cause a few cold helium atoms to desorb, which can then be heated up by the hot surface and release cold atoms again [97]. The cell runtime was significantly improved to several weeks by sealing the 4 K stages with only a 2"-diameter hole for pumping and a 1"-diameter aperture for YO exiting the chamber.

### 3.2 $Y_2O_3$ Single-stage Buffer Gas Source

We never explored the two-stage cell geometries such as the mesh size, spacing and aperture size. Instead, we took away the second stage and made a few changes to get a single-stage cell. The differences are shown in Figure 3.3. As for a single-stage cell, the forward velocity of the molecule beam increases with the helium flow, as predicted [45]. While in a two-stage cell, it remains consistently low since the boosting effect is reduced by the second stage. Removal of the second stage increased the forward velocity by more than 30 m/s, as shown in Figure 3.3 (a), but also increased the molecule number by a factor of 100, as shown in Figure 3.3 (b). The deceleration distance increases by a factor of two, resulting in a diffusion loss of 75%. As a result, the number of slowed molecules increases by more than an order of magnitude by removing the second stage cell. It doubles the number of photon scattering to slow molecules down to rest but it is not a limit to our experiment at the moment. To achieve better thermalization and slower forward velocity, we installed a diffuser and spacer [98] to slow down the helium before it collides with YO. Unfortunately, it didn't make a noticeable difference.

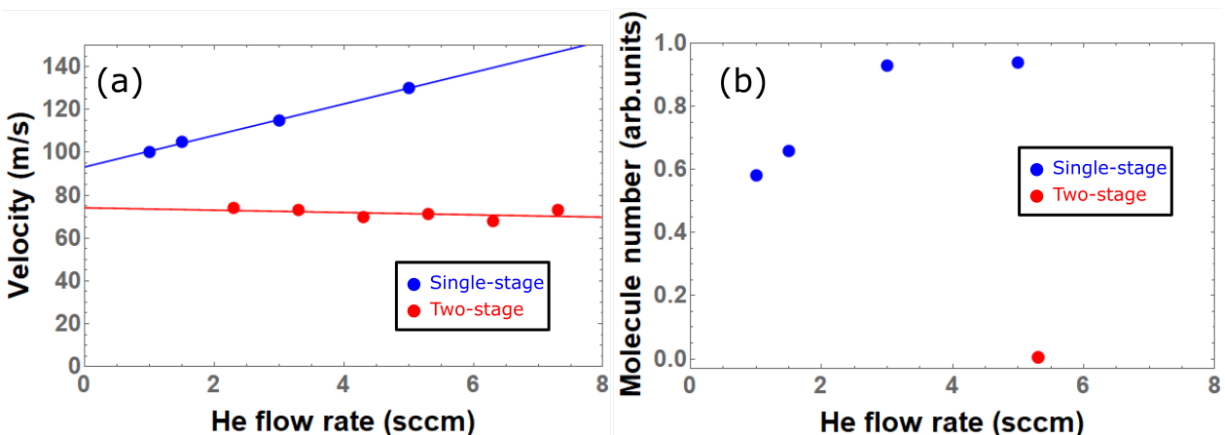


Figure 3.3: Performance of single-stage vs two-stage cell. (a). Forward velocity of molecular beam versus different helium flow rates. The forward velocities of the two-stage cell are independent of helium flow, as the boosting effect is reduced by the second stage. While it increases linearly with the helium flow rate in the single-stage cell, as expected. (b). Molecule yield at different helium flow rates. The leaky second stage reduces the molecule number by a factor of 100.



### 3.2.1 Cell Heating

Previously, the experiment was running at a repetition rate of 10 Hz for fast data acquisition. Then we found that the buffer gas cell generated many more molecules while the ablation is operating at a low repetition rate. As shown in Figure 3.4 (a), three times more molecules are generated per shot at ablation rate of 1.4 Hz than 10 Hz, while the forward velocities are very similar. We've tried ablating at lower repetition frequency but it didn't make any difference. The theory behind this change is due to the heating of the ablation target and the cell. A 5 mJ laser ablating at 10 Hz introduces 50 mW into the 4 K stage, where the cooling capacity is only  $\sim 1$  W. To cool the  $\text{Y}_2\text{O}_3$  ceramic more efficiently, instead of mounting on the ring, as shown in Figure 3.1, where the thermal conductivity is terrible, now the  $\text{Y}_2\text{O}_3$  pellets are directly epoxied on a copper base which is directly mounted on the 4 K cell, as shown in Figure 3.5 (a). This didn't solve the problem, we therefore operated the entire experiment at 1 Hz. Similar molecule reduction is also observed when a  $\sim 20$  mW off-resonant laser is always pointing into the cell, as shown in Figure 3.4 (b). This confirms our theory of molecule loss resulting from incidental heating of the cell. To reduce any possible heating of the cell, our experiment runs at a low rep rate (1 Hz) and two in-vac shutters (Vincent Associates Uniblitz VS14S1T0ECE) were installed to block any laser beams after the molecules have passed the shutter location, as shown in Figure 3.5 (b). The seal is realized by buna-N O-rings and the shutters are thermally heatsunk to the aluminum beambox or vacuum flanges.

### 3.2.2 Coating Cell Surface with $\text{Y}_2\text{O}_3$ Nanopowder

We have experimented with a couple of different cell geometries to generate more and slower molecules. None of these have worked better than our original design. After attempting these alternative designs, we couldn't even recover the molecular beam using our original cell. Eventually, we found that the coating of  $\text{Y}_2\text{O}_3$  powder on the inner side of the buffer gas cell plays an important role.

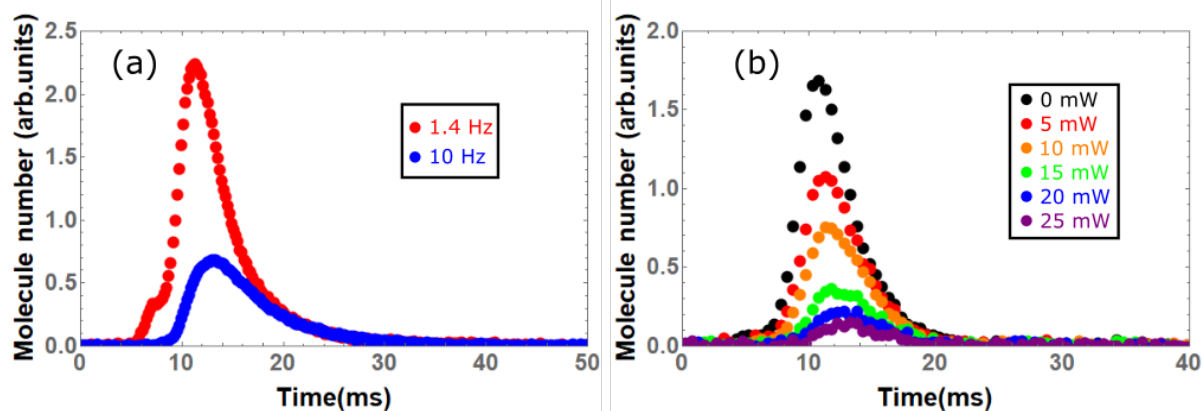


Figure 3.4: Molecule yield affected by cell heating. (a). Molecule yields per shot at different ablation rate. More molecules are generated at low rep rate as less heat is introduced to the cell. (b). Molecule yields at different heating power given by a off-resonant CW laser. It proves our theory that molecule yield is affected by the cell heating.

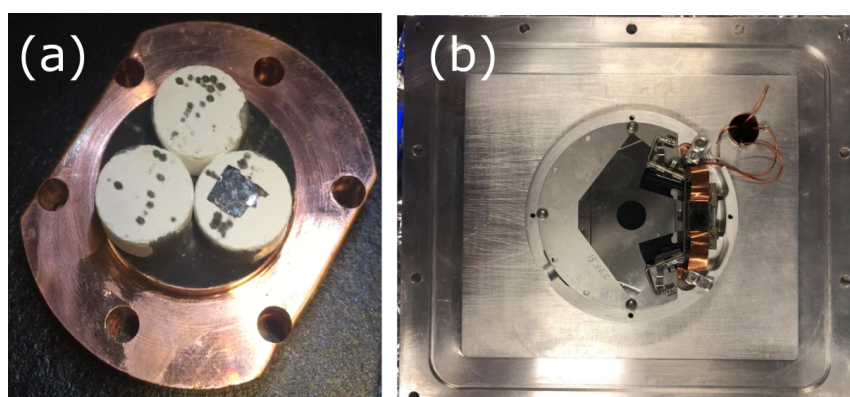


Figure 3.5: (a). Y<sub>2</sub>O<sub>3</sub> pellets exoposed on the copper mount. Laser ablation leaves black marks on the surface. (b). In-vacuum shutter installed on the inner surface of the beambox. There is another one installed  $\sim 15$  cm away.

Unlike CaF [99], Y<sub>2</sub>O<sub>3</sub> cell doesn't accumulate dust after weeks of operation, as shown in Figure 3.6 (a)(b). However, a clean cell doesn't behave the same as a "marinated" cell. There is still a very thin coating affecting the molecule yield. Therefore, we coated the cell by brushing the Y<sub>2</sub>O<sub>3</sub> nanopowder dissolved in isopropanol onto the interior cell surfaces. Currently, we're not able to precisely control the thickness of the coating which affects the molecule yield, as shown in Figure 3.6 (c)-(e), but we're able to repeatedly hit a nearly optimal performance.

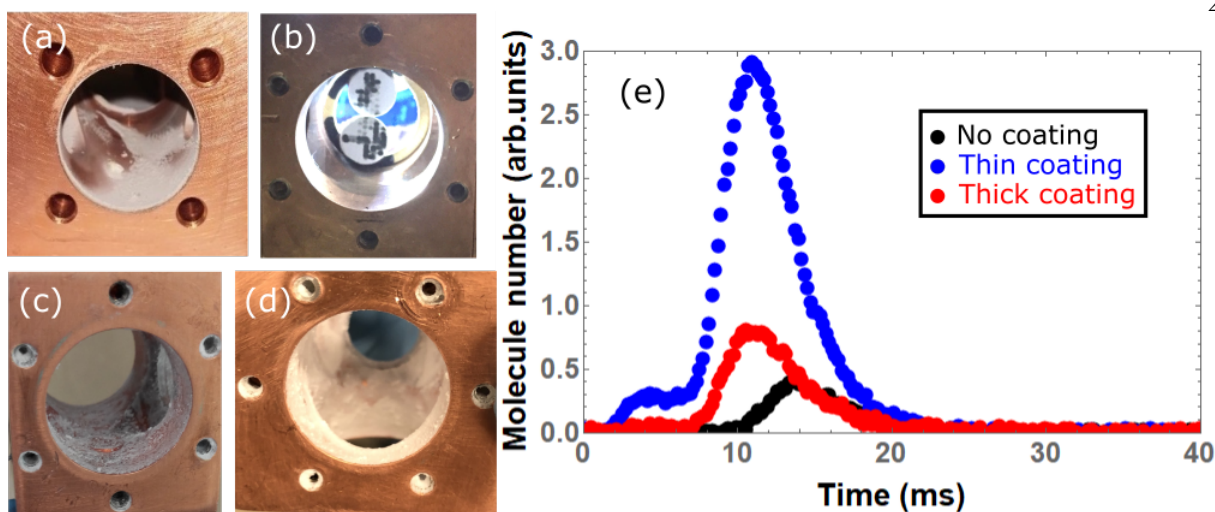


Figure 3.6: (a). CaF<sub>2</sub> cell after two weeks of running. Courtesy of Loic Anderegg. (b). Y<sub>2</sub>O<sub>3</sub> cell after years of operation. (c). Y<sub>2</sub>O<sub>3</sub> cell coated with thin layer of Y<sub>2</sub>O<sub>3</sub> nanopowder(Sigma Aldrich 544892). (d). Y<sub>2</sub>O<sub>3</sub> cell with thick coating. (e). Molecule yields with different coating. The Y<sub>2</sub>O<sub>3</sub> coating on the cell significantly affects the molecule yield, we therefore apply a thin coating to boost up the molecule yield.

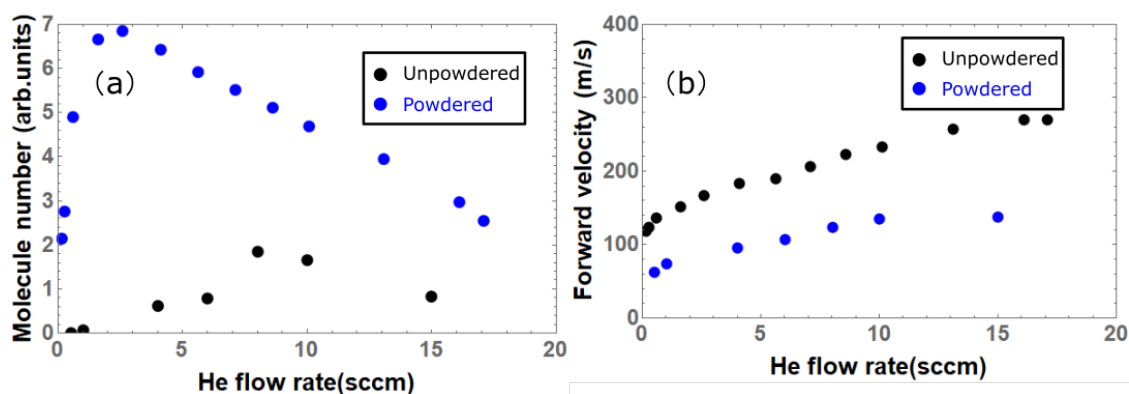


Figure 3.7: Cell behaviour with/without powder. (a).Molecule number. (b). Forward Velocity. With a powdered cell, more molecules with a low forward velocity can be generated at low helium flow rate.

The nanopowder coating also affects the hydrodynamics inside the cell, as shown in Figure 3.7. With coating, the cell can operate at a lower helium flow rate (<2 sccm), creating more molecules at a slower forward velocity. This really helps reducing the pressure at the science chamber. Unfortunately, our knowledge is still empirical and the physics behind this yield enhancement

requires further investigation.

Lower helium flow rates introduce a problem by coating the ablation window. At low helium flow, the molecular plume produced by ablation has a higher chance reaching the ablation window, which contaminates the window and affect the ablation efficiency. This coating can't be removed by the ablation laser, thus the window has to be replaced after two days. To prevent this, a skinny snorkel [98] with the length of 1" is added to move the ablation window farther from the pellets. This resulted in replacing the ablation windows bimonthly.

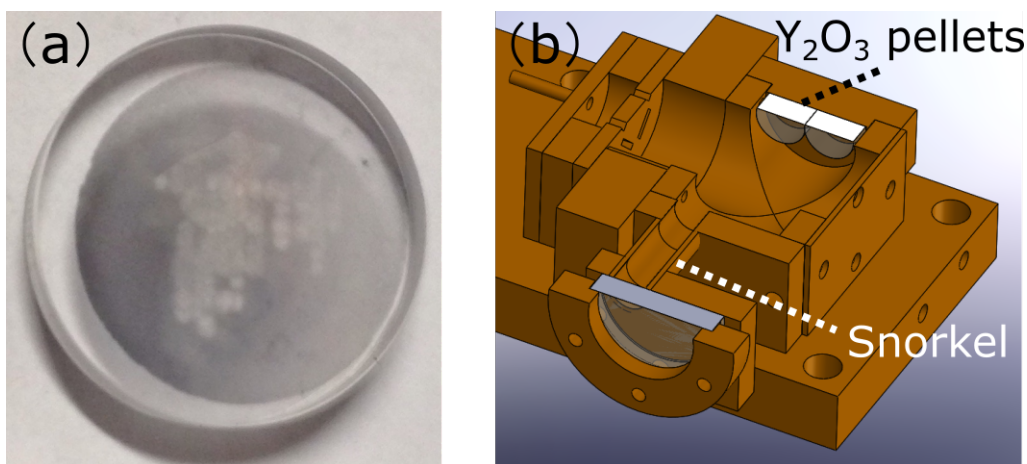


Figure 3.8: (a). Ablation window after weeks of runtime. The window is coated and the coating can not be removed by the ablation laser. (b). A long snorkel is introduced to create a gap between ablation window and target to reduce the coating effect.

### 3.2.3 Cell Performance

For a specific cell geometry, there are several parameters that affect the molecule yield including helium flow rate, ablation energy, ablation focus and ablation spot. For a single stage  $Y_2O_3$  cell with nanopowder coating, we typically operate at low helium flow (0.25 sccm) and high ablation energy (18 mJ), providing  $\sim 10^7$  molecules with the forward velocity of 120 m/s. Higher helium flow and ablation energy will produce more molecules at higher forward velocity, however this increases the slowing distance and thus decreases the useful flux to the MOT region. Furthermore, it is typically ideal to focus the ablation laser on the sample surface where a brightest and slowest

molecule beam is generated.

### 3.3 $Y + O_2(O_3)$ Source

To generate more CaF molecules, Tarbutt group opted for a chemical source using a calcium metal and  $SF_6$  gas [89]. In their setup, the ablation of metals in a buffer gas cell is very reliable and it provides very high fluxes. Using this chemical source, they generated a flux of  $5 \times 10^{10}$  molecules per steradian per pulse in a single rotational state with a mean speed of  $\sim 150$  m/s. Similar increases for YO has been observed by the presence of oxygen at room temperature [100]. So we introduced the  $O_2$  and  $O_3$  into the cell for chemical interaction.  $O_2(O_3)$  sublimates at 54 K ( $\sim 81$  K), so the vapor pressure at  $\sim 100$  K would be high enough to prevent clogging. We sent  $O_2(O_3)$  directly into the cell from a modified back plate, as shown in Figure 3.9 (a). The gas line was designed to have a weak thermal connection to the 40 K shield with a resistive heater epoxied to maintain at  $\sim 120$  K. A thin (1/16" OD) stainless steel tube was used to reduce the thermal conductivity and a thermal diode (Lakeshore DT-670-CU) was installed at the entrance to monitor the temperature. The gas line penetrated through the diffuser, spacer and was isolated from the 4 K cold cell with a small Ultem spacer, as shown in Figure 3.9 (b).

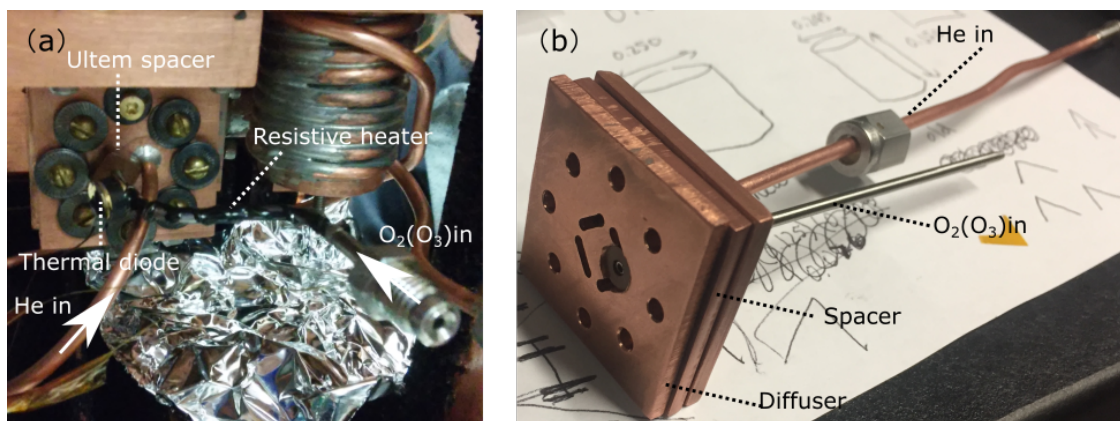


Figure 3.9: Inserting a  $O_2(O_3)$  line into the cell. (a). Back plate of the cell. (b). Modified diffuser, spacer and black plate. A Ultem spacer is used to prevent the  $O_2(O_3)$  from touching the 4K copper. A resistive heater is also epoxied to the line to maintain the temperature at  $\sim 120$  K.

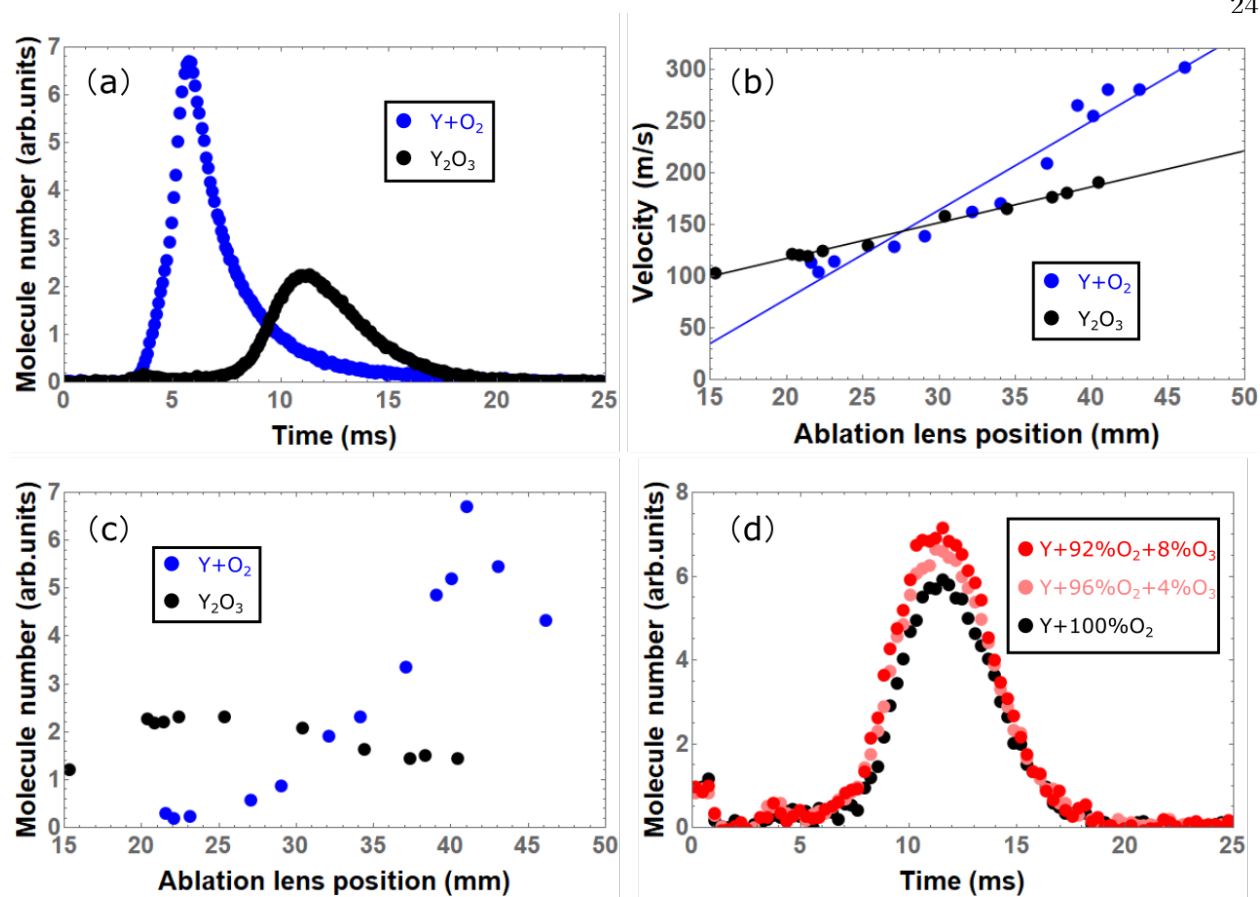


Figure 3.10: Comparison of Y+O<sub>2</sub>(O<sub>3</sub>) with Y<sub>2</sub>O<sub>3</sub> cell. (a). Molecule free flight signal. (b). Molecule forward velocity versus ablation lens position. (c). Molecule number at different ablation lens position. (d). Molecule number at different O<sub>3</sub> levels. Y+O<sub>2</sub>(O<sub>3</sub>) chemical source provide more molecule but at higher forward velocity, which is bad for molecule slowing experiment. The O<sub>3</sub> helps improving the molecule yield, but it is still worse than directly ablating Y<sub>2</sub>O<sub>3</sub> pellet. However, all these were tested without the thin coating mentioned above. A more systematic study with the Y<sub>2</sub>O<sub>3</sub> nanopowder coating is required.

We placed both Y<sub>2</sub>O<sub>3</sub> and Y metal inside the cell to directly compare their yield. Y metal with O<sub>2</sub> provides more but faster YO molecules than Y<sub>2</sub>O<sub>3</sub> pellet, as shown in Figure 3.10 (a). A fast forward velocity is detrimental for slowing, so we scanned the ablation focus for both Y<sub>2</sub>O<sub>3</sub> cell and Y+O<sub>2</sub> cell, as shown in Figure 3.9 (b)(c). For Y+O<sub>2</sub>, it's hard to generate molecules at small forward velocity, which is not ideal for molecule slowing experiment. We also tried more volatile oxidizer like O<sub>3</sub> which may be more reactive with Y metal. As we can see in Figure 3.9 (d), the presence of O<sub>3</sub> helps increase the molecule yield but doesn't change the velocity distribution at all.

It's worth mentioning that the chemical reactions were tested before we realized the importance of the nanopowder coating. So the chemical source needs to be investigated more seriously with the powdered cell. In the end, we didn't use this approach in our experiment but switched back to ablating pure  $\text{Y}_2\text{O}_3$  ceramic pellets.

### 3.4 Next Generation of YO Source

With all the upgrades mentioned above, we could generate  $\sim 10^7$  molecules with the forward velocity of 120 m/s. For the nanopowder coated cell, we found that the molecule yield is decent even at very low helium flow rates (0.25 sccm). A single spot on the  $\text{Y}_2\text{O}_3$  pellet enables  $\sim 10^4$  ablations, so the whole pellet provides hundreds of thousands of shots. In addition, under such a low helium flow rate, the cryogenic sorbs won't saturate for months. Thus, the total runtime of the cell is mainly limited by the coating of the ablation window, which takes about a month. In the next section, I list several drawbacks remaining in the current system and then introduce the next generation of YO buffer gas cell.

#### 3.4.1 Molecule Yield Fluctuation

The spacing between rotational levels is on the order of tens of GHz, as described in Chapter 2. This energy scale is on the thermal scale of a few Kelvin. Figure 3.11 (a) shows the calculated occupation of rotational levels as a function of temperature. Since our experiment focus on  $N=0,1$  and 2 states, to have sufficient population, temperatures of 4 K or less are required, as shown in Figure 3.11 (b). So the cell at lower temperatures could generate more useful molecules.

We measured the dependence of molecular yield on temperature, as shown in Figure 3.12 (a), by turning off or on the pulsetube while ablating molecules. The cell temperature is measured by a thermal diode (Lakeshore DT-670-CU) attached directly under the cell. Molecule number increases with lower temperature at different helium flow rates, which matches the model calculated in Figure 3.11 (b). Due to the nature of the pulsetube, the cell temperature is fluctuating by  $\sim 0.2$  K at  $\sim 1.4$  Hz. If the experiment is not synchronized with the pulsetube, the molecule yield would

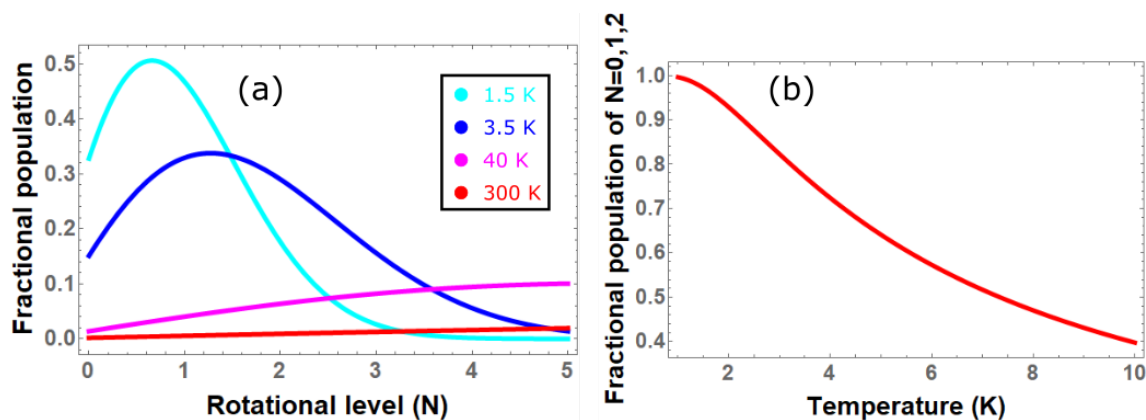


Figure 3.11: Molecule yield at different temperature. (a). Calculated thermal occupation of rotational levels for YO. (b). Calculated occupation of the 3 lowest rotational states ( $N=0,1,2$ ) versus cell temperature. A cell at lower temperature can generate more molecules at  $N=0, 1, 2$  states, which are useful in our experiment.

fluctuate by 20%, as shown in Figure 3.12 (b), resulting in an unstable signal. In our experiment, we synchronized the experiment cycle to the pulsetube cycle to achieve a stable yield. We therefore operate the experiment at 1.4 Hz, the same as pulsetube. The synchronization is realized by monitoring the cell temperature and trigger the experiment at the correct timing.

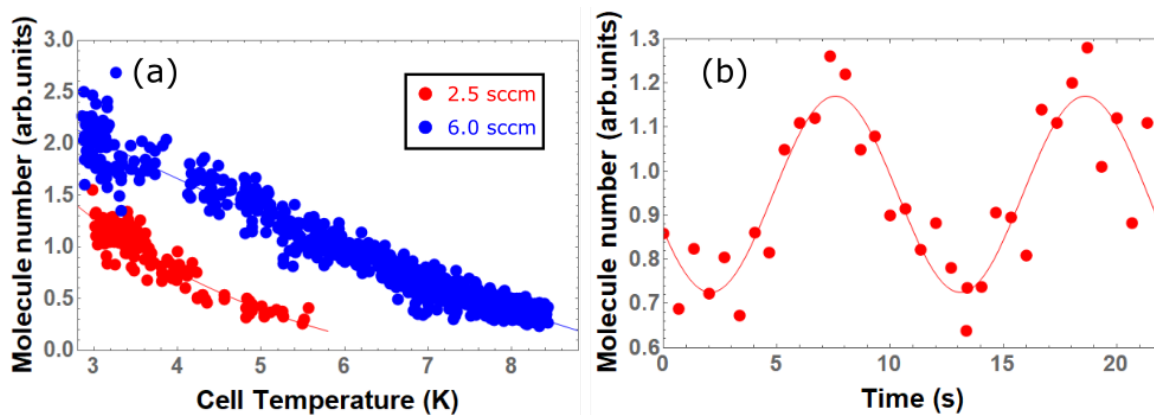


Figure 3.12: Measurement of molecule yield at different cell temperature. (a). Molecule yield at different cell temperature. The molecules yield at 2.5 sccm has a stronger dependence than 6.0 sccm, as the thermalization is better in the latter case. (b). Fluctuation of molecule yield due to the nature of pulsetube. The ablation operates at  $\sim 1.3$  Hz, different from the rep rate of the pulsetube (1.4 Hz).



### 3.4.2 Limited Pumping and Accessibility

As discussed previously in section 3.2.1, two in-vacuum shutters are installed to prevent the cell heating by blocking the laser beams into the cell. In addition, they also help maintain the pressure of the science chamber by blocking the helium. As we can see in Figure 3.13 (a), the science chamber pressure increases with helium flow but remains to be  $\sim 10^{-9}$  Torr. Without these shutters, the pressure would be more than  $10^{-8}$  Torr, limiting the trap lifetime to less than a second. This indicates that the helium exiting the cell is not pumped out sufficiently. It could be improved by installing more cryogenic sorbs in the region between the cell aperture and the front 4 K shield. Currently, they are only  $\sim 5$  cm apart, so more sorbs can't be inserted.

As mentioned above, the cell runtime is currently restricted by the coating on the ablation window, which is also limited by our beam box dimension. A longer snorkel would reduce the amount of YO powder reaching the ablation window, which requires more space between cell and 4 K shields, as shown in Figure 3.13 (b) and (c). The limited space also makes it extremely hard to swap the sample and targets.

Another issue is the copper plates get oxidized overtime thus their reflectivity reduces as well, which eventually increases the heat load into the cell. An oxygen resistant gold coating should be applied to the surface to prevent the copper blackening.

### 3.4.3 1 K System

A new 1 K system is designed to overcome all these problems. In the current setup, the cell is cooled to 4 K directly by the 4 K stage of the cryocooler (Cryomech PT410). In the new setup, the cryogenic buffer gas cell is cooled to 1 K via a thermal connection to a 1 L pot of helium which is pumped by a roughing pump (Edwards XDS 10). With a pumping speed of 10 L/s and a heating rate of 100 mW, the pot temperature is  $\sim 1.4$  K [101]. A 1 L pot of liquid helium provides a runtime of about 7 hours between refills, which should be more than enough for daily operation. At 1.4 K, the new cell generate  $\sim 50\%$  more molecules than the current 4 K cell,

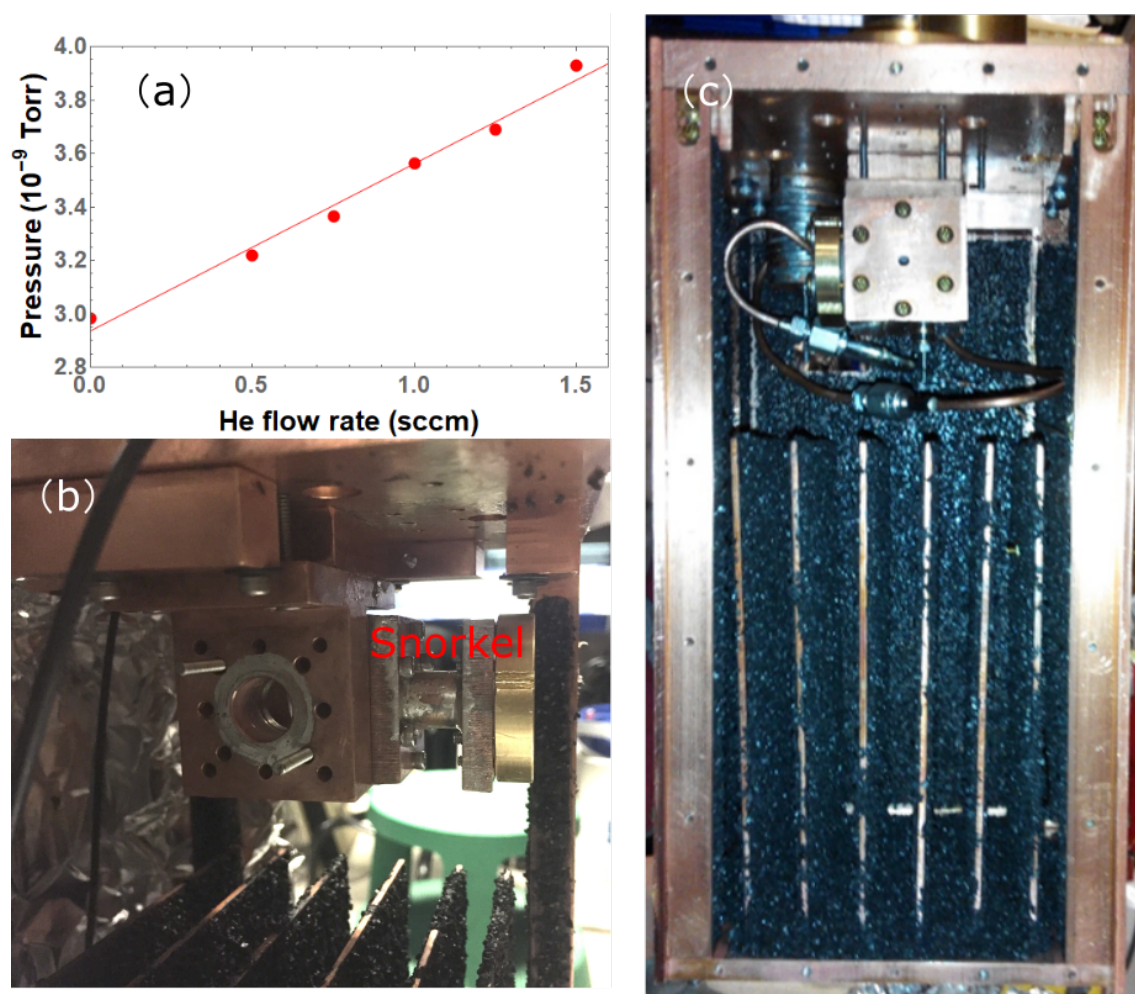


Figure 3.13: (a). Science chamber pressure versus helium flow rate with shutters open 8 ms every second. (b). Back view of the cell, snorkel included. The cell is directly anchored on the 4K cold head. (c). Front view of the cell, snorkel not installed. We can see the space is very limited.

according to the calculation in Figure 3.11 (b). The molecule yield should also be very stable since the cell temperature doesn't fluctuate with the pulsetube. Our experiment timing doesn't need to be synchronized to the pulsetube any more. In addition to the temperature, the cell wouldn't physically oscillate together with the pulsetube as well. Therefore, the cell pointing should be stable, resulting in a much stable and bright source. The 4 K and 40 K pulsetube stages are thermally connected to radiation shields by copper braids(not shown) to decrease the black body radiation onto the cell. The heat loads are estimated to be about 30 mW, 300 mW and 20 W on 1

K, 4 K and 40 K stages. Besides, all shields are supported from the bottom with the thin stainless steel rods isolating the heat exchange between different stages.

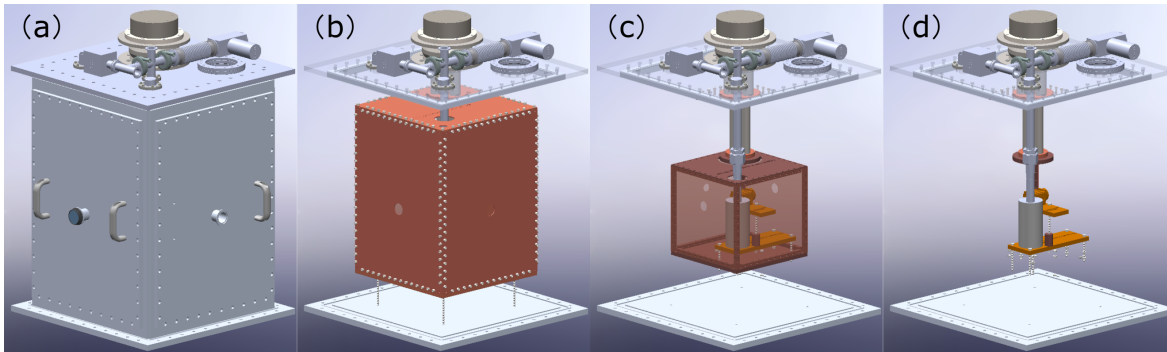


Figure 3.14: Beambox view for each layer. (a). Beambox. (b). 40 K shields. (c). 4 K shields. (d). 1 K pot and cell.

The 1 K design is shown in Figure 3.14 and 3.15. Here I list several features for the new design. In the previous design, the entire 4K and 40K copper enclosures are directly mounted on the pulsetube. As a result, there are  $\sim 20$  kg of copper while the recommended loads are only 5 kg on 4K stage and 10 kg on 40K stage. This can potentially introduce a leak into the system, also it was very hard to access the panels without disassembling everything. A very thin stainless steel rod is used to support most of the things from the bottom. We choose  $\frac{1}{4}$ "-20 threaded rod as a support to reduce possible heat transfer between each layer. Special care is taken in the 1K pot design as it experiences a large temperature gradient from 300 K to 1 K. The 0.065" thick tubing is used to reduce the cross section for low thermal conductance. To increase the pumping performance, a CF 6" flange is designed on the top panel to directly pump out the chamber. A KF 25 flange is left at the corner to pump out the hot helium from the pot, as shown in Figure 3.14 (d). It is worth mentioning that there is 1K system available from Cryomech, which is a closed system that doesn't require filling in helium. We can implement this in the future if we want to simplify our 1 K system. Currently, the new beambox has been made and hopefully it will be assembled pretty soon.

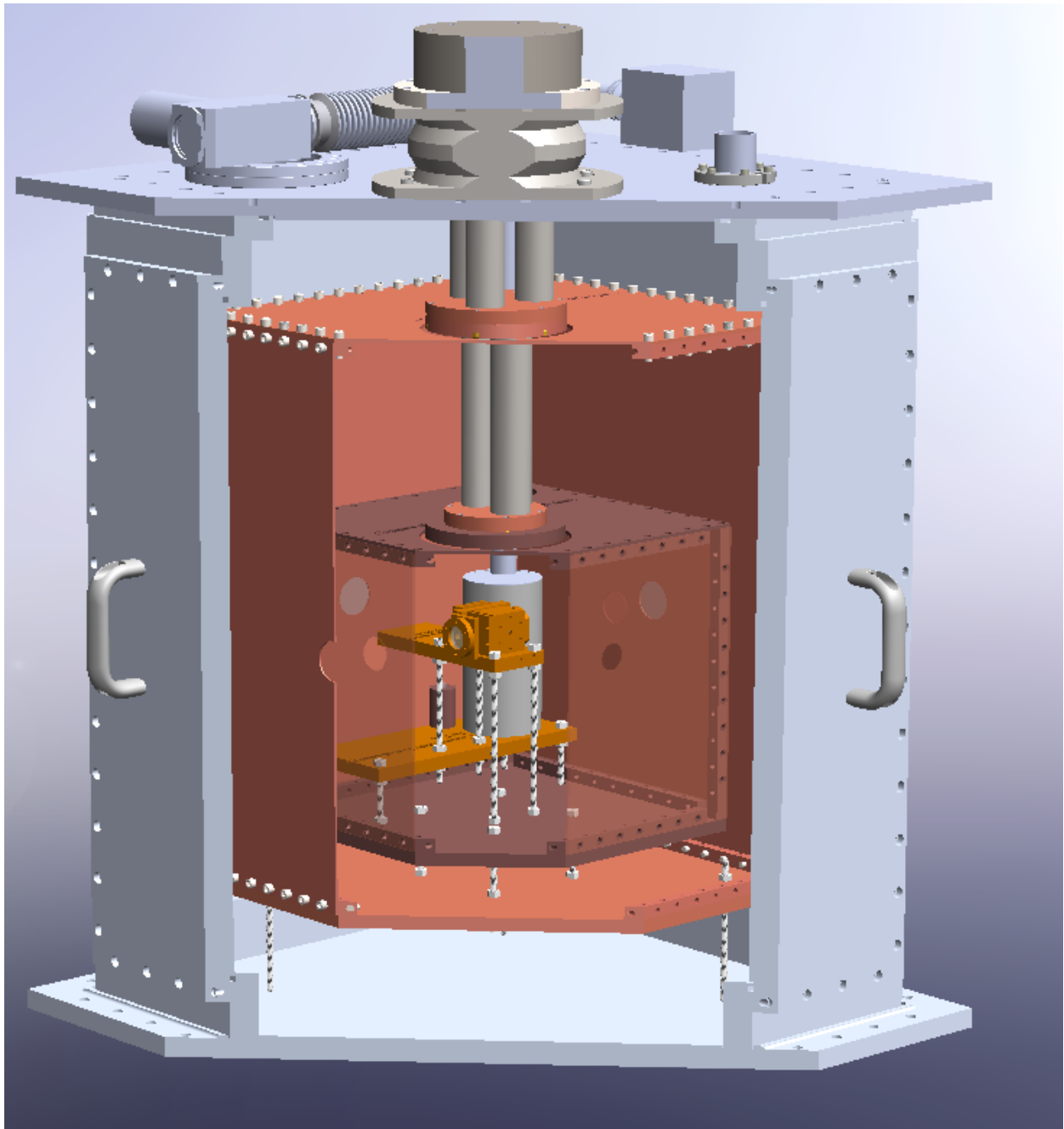


Figure 3.15: Section view of the new beam box.

## Chapter 4

### Laser Slowing

Molecules exiting the buffer gas cell move at  $\sim 120$  m/s. In order to capture molecules into a magneto optical trap(MOT), they need to be slowed down to the MOT capture velocity  $v_c = \sqrt{\frac{hk\gamma D}{m}}$  [102], which is on the order of 5 m/s. In atomic physics experiment, people have developed several techniques to slow atoms but it remains challenging for molecules due to their complex structure. Slowing the molecules down to trappable velocity takes us three years and it remains to be the most inefficient step in the experiment. In this chapter, we introduce the basic slowing theory, slowing setup, detection method, slowing upgrades and a potential scheme with better slowing efficiency.

#### 4.1 Laser Slowing YO

The idea of a radiative scattering force on free atoms being velocity dependent and therefore useful for cooling a gas was proposed in Refs. [103, 104, 105]. The Zeeman slower [106] and chirped slowing [107] are the two main techniques used in the cold atom community. In order to achieve the continuous photon scattering, these techniques adopt different ways to compensate the Doppler shifts since the scattering is strongly velocity dependent. In both cases, a laser beam is directed opposite to an atomic beam.

Zeeman slower is a simple and stable deceleration method, where a tapered magnetic field is employed to cover a range of initial velocities. This works by utilizing a spatially varying magnetic field to compensate the changing Doppler effects by the correspondingly adjusted Zeeman shifts.

The magnetic field is specially designed for specific atomic species thus the atoms are always resonant to the laser beam during the entire deceleration. This design relies on the fact that the atoms have a large Zeeman shift in the excited state and limited number of ground states. Unfortunately, molecules typically don't possess these properties. As shown in Figure 2.2, YO molecules have 12 ground states with distinct Zeeman shifts, which means the molecules can decay into both high and low field seeking states. In addition, the excited state  $A^2\Pi_{1/2}$  has a very small Lande g factor, making the Zeeman slower even harder. In our experiment, we chirp laser frequencies to slow the molecules. Recently, various methods for molecule cooling including, a different type of Zeeman slower and stimulated cooling with adiabatic transfer are proposed [108, 109, 110, 111, 112, 113] to cool molecules more efficiently.

## 4.2 $\Gamma/13$ Slowing Scheme

The generation of molecules from a cryogenic buffer gas cell is described previously in Chapter 3, which provides relatively low initial forward velocities. With a forward velocity of  $\sim 120$  m/s and a recoil velocity of 6.2 mm/s, it takes  $2 \times 10^4$  photon scatterings to slow down to rest, thus a closed cycling transition is required. With two vibrational repumps ( $v=1$  and  $2$ ), molecules can scatter more than  $10^6$  photons before getting dark.

### 4.2.1 $\Gamma/13$ Repumping Scheme

The most relevant details of our  $\Gamma/13$  slowing scheme are shown in Figure 4.1 where the vibrational repumps are not shown for simplicity.  $X^2\Sigma^+ N=1(-)$  and  $A^2\Pi_{1/2} J'=1/2(+)$  are the ground and excited state for the main cycling transition. The  $N=1$  state is chosen to alleviate the need of rotational repumping due to parity and angular momentum selection rules of  $\Delta N=0, \pm 1$  [54]. In this case, the repumping scheme is very simple where only one laser is required on each vibrational level. Therefore, only three lasers are required for slowing molecules. Unfortunately, there is an intermediate level  $A'^2\Delta_{3/2}(J' = 3/2(-))$  lying at a lower energy than the excited state  $A^2\Pi_{1/2}$ , making the cycling transition more complicated. The  $A^2\Pi_{1/2}$  to  $A'^2\Delta_{3/2}$  transition is

electric dipole forbidden, however, it does occur due to the mixing of the nearby  $A^2\Pi_{3/2}$  with the  $A'^2\Delta_{3/2}$  [78], resulting in a  $3 \times 10^{-4}$  chance of decaying to  $A'^2\Delta_{3/2}$  state. Since it is a two photon process, molecules that decay to  $X^2\Sigma^+$  via  $A'^2\Delta_{3/2}$  end in the  $N=0$  or  $2$  levels where it becomes dark to the cooling laser. To maintain the continuous scattering, microwaves are applied to directly mix the  $N=0$  and  $N=2$  states with the  $N=1$  state, depicted as blue arrows in Figure 4.1. Therefore,  $v=0$   $N=0-2$ ,  $v=1$   $N=1$  of  $X^2\Sigma^+$  and  $J'=1/2(+)$  of  $A^2\Pi_{1/2}$  are all directly connected in the main cycling transition. In this scheme, there are 4 manifolds coupled in the excited state ( $n_e = 4$ ) and 48 manifolds involved in the ground state ( $n_g = 48$ ). This results in an effective scattering rate [75, 76]  $\Gamma_{Scatter} = \frac{n_e}{n_g+n_e}\Gamma$  of  $\Gamma/13$ .

In this scheme, there are 4 manifolds coupled in the excited state ( $n_e = 4$ ) and 48 manifolds involved in the ground state ( $n_g = 48$ ). This results in an effective scattering rate [75, 76]  $\Gamma_{Scatter} = \frac{n_e}{n_g+n_e}\Gamma$  of  $\Gamma/13$ .

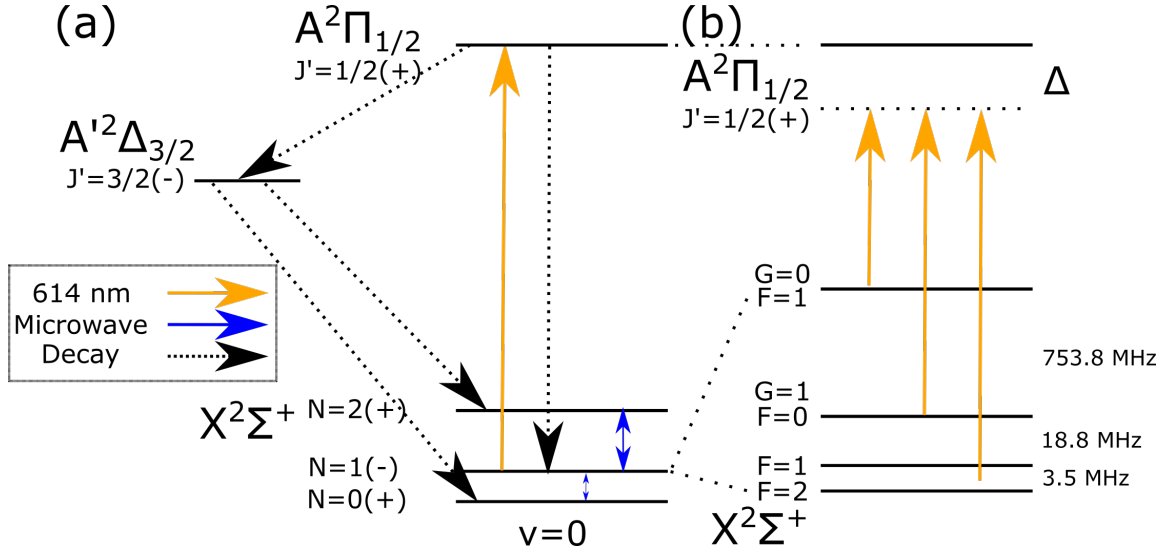


Figure 4.1:  $\Gamma/13$  slowing scheme. (a). Configuration of main slowing beam and microwave repumpers. Vibrational repumpers are not shown for simplicity. (b). Detailed setup for main slowing beams addressing different hyperfine manifolds.

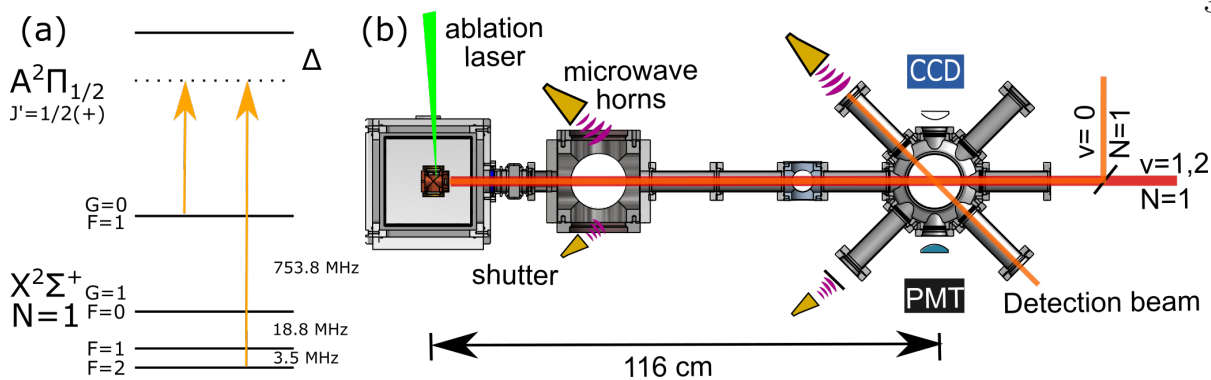


Figure 4.2: Detection method. (a). Single photon detuning  $\Delta$  corresponds to the Doppler shift, which is related to the detection velocity. (b). Experiment apparatus for slowing and velocity sensitive detection. The detection beam is 45 degree with respect to the molecule beam.

#### 4.2.2 Detection Method

The detection of slowed molecules is tricky for the molecules with many hyperfine splittings. The splitting between  $G=0$  and  $G=1$  is 750 MHz, corresponding to 650 m/s at  $45^\circ$  detection. With the multiple hyperfine states of YO separated by 20 MHz ( $\sim 17$  m/s at  $45^\circ$  detection), we apply two lasers detecting  $G=0$  and  $G=1$  states separately, as shown in Figure 4.2 (a). This two-laser detection is sensitive to the distribution of hyperfine states, which would underestimate the speed of molecule by  $\sim 10$  m/s. In experiment, we vary the single photon detuning  $\Delta$  to detect molecules at different velocities. This velocity sensitive light induced fluorescence (LIF) signal is detected by a PMT (Hamamatsu R10699), feeds to a home-built preamplifier and then filtered by a multichannel scaler (Stanford Research Systems SR 430) that sets the threshold for photon counting. The counts are collected by a NI-DAQ card and then processed with Matlab. The PMT collection efficiency is  $\sim 3 \times 10^{-4}$  which is calculated according to the geometry.

The initial slowing result is unstable due to the low slowing efficiency and the unstable molecule yields between shots. To understand the slowing performance, it is crucial to take a velocity distribution of the free molecules and the slowed molecules. This is achieved by modulating the one photon detuning  $\Delta$  at high frequency (1 kHz) and extract the velocity distribution based on the modulation timing.



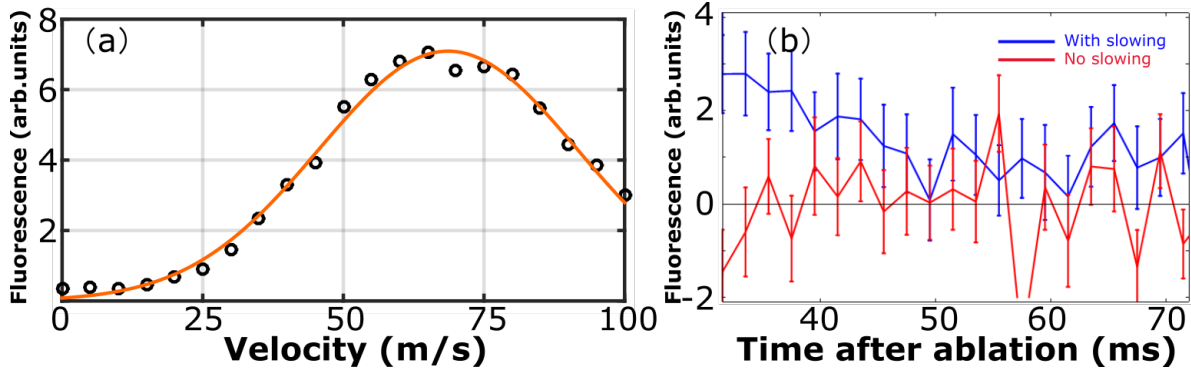


Figure 4.3: Doppler sensitive detection. (a). Initial velocity distribution of the two stage cell. (b). Detecting 10 m/s molecules, slowing beams are off at 33 ms. Our initial slowing with second stage cell is terrible.

### 4.2.3 Performance

The detection method works great for detecting a velocity distribution, the velocity distribution from our two stage cell is shown in Figure 4.3 (a). For optimal slowing to 10 m/s, the slowing laser was applied 5 ms after the ablation pulse and was on for 28 ms. The slowing beams are broadened by EOMs to cover a broader velocity group of molecules. Unfortunately, we're never able to slow more than a hundred of molecules to 10 m/s due to the low initial molecule number and the poor slowing efficiency (<1%) [90], as shown in Figure 4.3 (b). The two stage cell generates  $\sim 4000$  molecules peaked at 70 m/s. The initial molecule number gets boosted up to  $\sim 10^6$  by taking away the second stage together with all the upgrades previously mentioned in Chapter 3. After this upgrade, we're able to slow more than a thousand of molecules to 10 m/s. The low slowing efficiency is primarily due to the the small deceleration rate that is limited by the effective scattering rate of this scheme,  $\Gamma/13$ .

## 4.3 $\Gamma/8$ Slowing Scheme with $N=2$ Decoupled

In order to slow more molecules, we tried to increase the deceleration rate by decoupling states from the cycling transition. With the fixed initial and final velocities, a larger deceleration leads to a shorter slowing distance. In this case, the transverse diffusion is reduced, as shown in

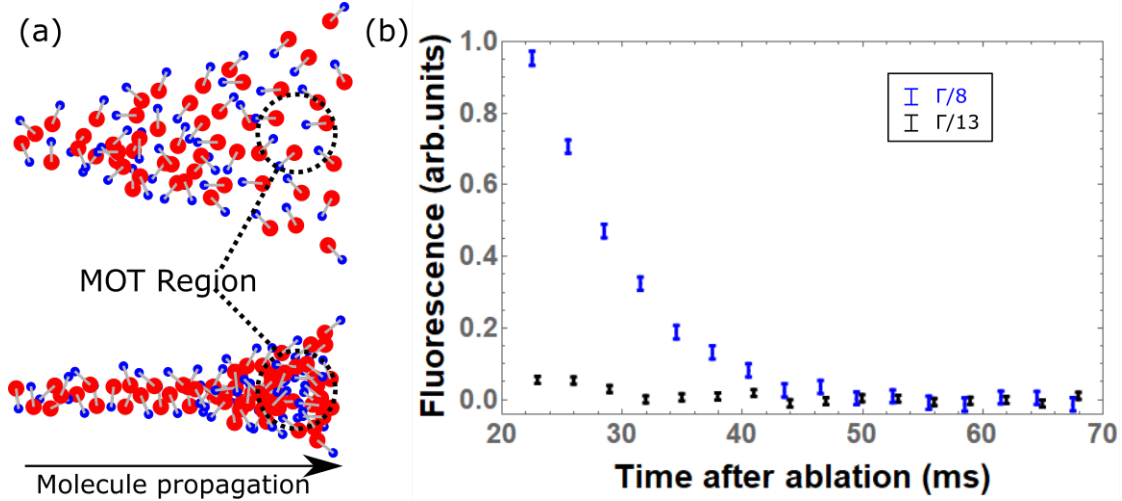


Figure 4.4: (a). Transverse diffusion with different deceleration rate. A high deceleration rate (bottom) reduces the transverse spread, increasing the number of molecules in the MOT region. (b). Detecting 5 m/s molecules at different scattering rate, slowing beams are off at 21 ms. The number of slowed molecules increases by  $\sim 20$  times with  $\Gamma/8$  pumping scheme.

Figure 4.4 (a), resulting in an increased number of molecules captured in the MOT.

### 4.3.1 Repumping Scheme

To increase the effective scattering rate, we decouple the  $X^2\Sigma^+$   $N=2$  from the cycling transition by removing the  $N=1 \leftrightarrow N=2$  microwave but directly optical pumping  $N=2$  to  $A^2\Pi_{1/2}$   $J' = 3/2$ , as shown in Figure 4.5 (a). From Section 2.2.2, we see by decoupling  $N=2$ , we now have 28 ground states ( $n_g = 28$ ) instead of 48, giving us an effective scattering rate  $\Gamma_{Scatter} = \frac{n_e}{n_g+n_e}\Gamma$  of  $\Gamma/8$ . With increased deceleration,  $\sim 20$  times more 5 m/s molecules are slowed than the  $\Gamma/13$  scheme, as shown in Figure 4.4 (b). A further increase could be achieved by decoupling the vibration repumping  $v=1$   $N=1$  state, from the cooling excited state  $A^2\Pi_{1/2}$   $J' = 1/2$  by pumping to  $A^2\Pi_{1/2}$   $J' = 3/2$  state where two  $v=1$  repumps are required, as shown in Figure 4.5 (b). In this scheme, we have 16 ground states ( $n_g = 16$ ) and 4 excited states ( $n_e = 4$ ), resulting in an effective scattering rate  $\Gamma_{Scatter} = \frac{n_e}{n_g+n_e}\Gamma$  of  $\Gamma/5$ . Unfortunately, we've never seriously explored the  $\Gamma/5$  scheme due to the increased number of vibration repumping lasers. It is still worth a try to get

more molecules slowed for the MOT.

### 4.3.2 Spectroscopy for $\Gamma/8$ Scheme

The  $N=1 \rightarrow J' = 3/2$  and  $N=2 \rightarrow J' = 3/2$  spectroscopy is taken to implement the new  $\Gamma/8$  repumping scheme. We excited the ground state molecules with a low intensity laser beam perpendicular to the motion of molecules and then collected the fluorescence. The laser frequency is modulated as described in Section 4.2.2, thus the entire spectrum is obtained in a single experiment. The results are shown in Figure 4.6. In our experiment, the  $N=2$  repumper is set at the right peak in Figure 4.6 (b) for the best slowing performance.

### 4.3.3 Slowing Setup and Performance

A dye laser was used to repump molecules on  $X^2\Sigma^+ N = 2(+)$  state, parking at the right peak shown in Figure 4.5 (b). With increased deceleration rate, the diffusion was suppressed since the slowing distance is reduced by 40%. As a result, the number of slowed molecules increased by a factor of 20, as shown in Figure 4.4 (b).

With so many lasers involved in chirped slowing, it is important to simultaneously sweep all laser frequencies to compensate for the Doppler shifts during the entire slowing. Our main slowing laser and vibrational repumpers are directly locked on an erbium frequency comb to achieve kHz stability. So, there are two ways to modulate these laser frequencies: either chirping lasers together with the comb or modulating them independently. Back in 2015 [90], we modulated the repetition frequency of the frequency comb thus all lasers locked on the comb would be modulated accordingly. This simple method is convenient when the wavelengths are close enough, which is true in our case. Our transition wavelengths are 614 nm, 648 nm and 649 nm. Therefore, the Doppler shifts on each transition are very similar. Considering the flexibility, we switched to a different scheme where the frequency comb remains static but the lasers are modulated by their locking acousto-optic modulators(AOM). A slowing laser setup is shown above in Figure 4.7. The detailed locking schemes are discussed in Appendix B of [114].

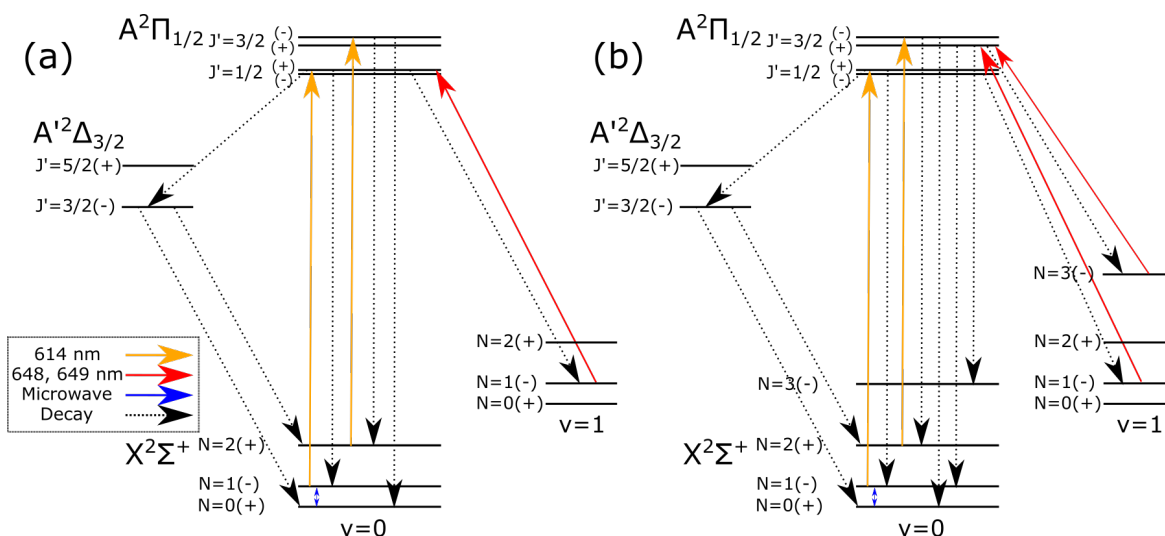


Figure 4.5: (a).  $\Gamma/8$  repumping scheme. The  $N=1 \leftrightarrow N=2$  microwave is removed, while the  $N=2$  is directly repumped to  $A^2\Pi_{1/2} J' = 3/2$  by a laser. The  $v=0$   $N=2$  state is therefore decoupled from the cooling ground state  $v=0$   $N=1$ , resulting in an effective scattering rate of  $\Gamma/8$ . (b).  $\Gamma/5$  repumping scheme. The  $v=1$  repumper is replaced by two lasers pumping into  $A^2\Pi_{1/2} J' = 3/2$  state.  $v=1$   $N=1$  state is therefore decoupled from the cooling excited state  $A^2\Pi_{1/2} J' = 1/2$  ( $+$ ), resulting in an effective scattering rate of  $\Gamma/5$ .

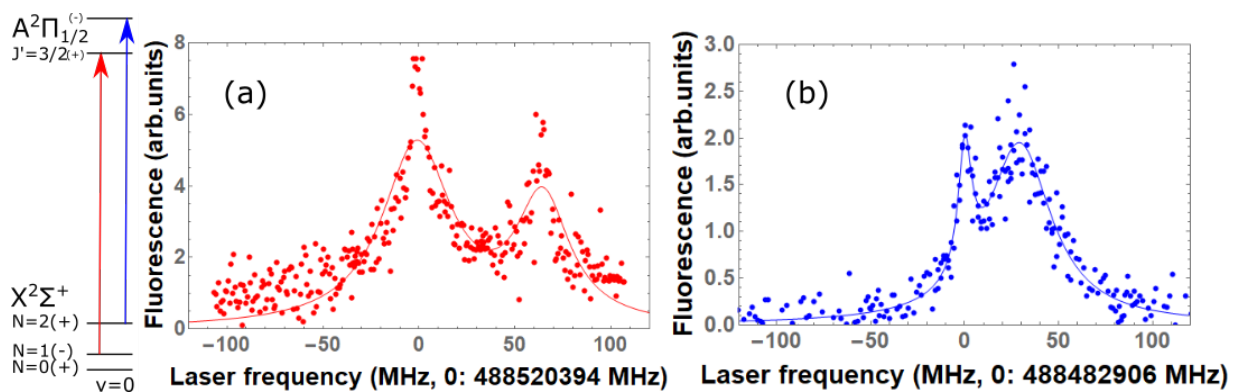


Figure 4.6: (a).  $X^2\Sigma^+ N = 1(-) \rightarrow A^2\Pi_{1/2} J' = 3/2(+)$  spectroscopy, peaks are  $F=1$  and  $F=2$ . (b).  $X^2\Sigma^+ N = 2(+) \rightarrow A^2\Pi_{1/2} J' = 3/2(-)$  spectroscopy, peaks are  $F=1$  and  $F=2$ .  $N=2$  repumper is parked at the right peak for the best slowing performance.

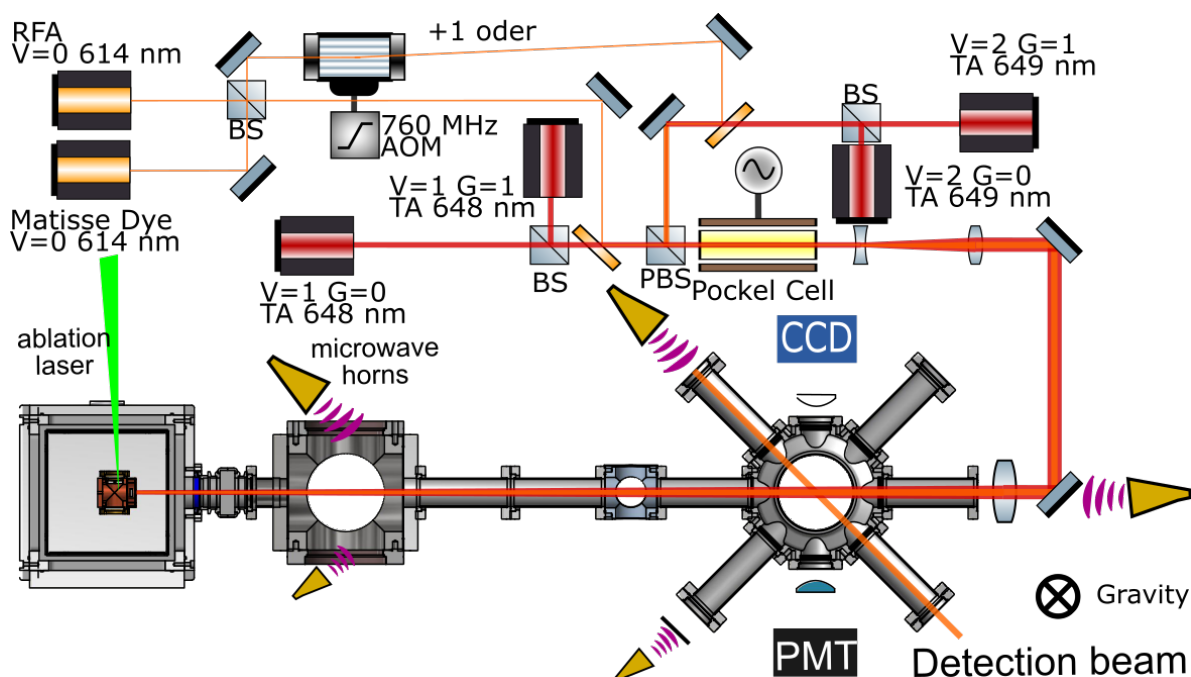


Figure 4.7: Slowing setup for chirped slowing. The vibrational repumpers  $v=1$  and  $v=2$  are injection locked and then amplified by the tapered amplifier. The main  $N=1$  transition and vibrational repumps are combined by dichroic mirrors and PBS.

A 1 W Raman fiber amplifier (MPB RFA) is used to address the main slowing transition. Since the  $N=2$  repumping is 9.617 GHz away from the main slowing transition, a commercial dye laser (Sirah Matisse DR) is used to repump the  $N=2$  dark state. RF sidebands produced by a series of AOMs address all hyperfine transitions. The beam combination is achieved by dichroic mirrors and polarizing beam splitter (PBS). In order to address more velocity groups, a 10 MHz EOM could be inserted to broaden the slowing spectrum. In addition, the combined beams go through a Pockels cell which switches the polarization between s and p to disrupt the optical pumping into the dark Zeeman states. The Pockels cell also introduces sidebands into the lasers, broadening the spectrum together with AOMs. The collimated slowing beams are slightly focused at the entrance of the science chamber to provide a transverse confinement and maintain a good mode match to the molecule beams. This technique doubles the number of slowed molecules. The solution for the cell heating by slowing beam is described in Section 3.2.1

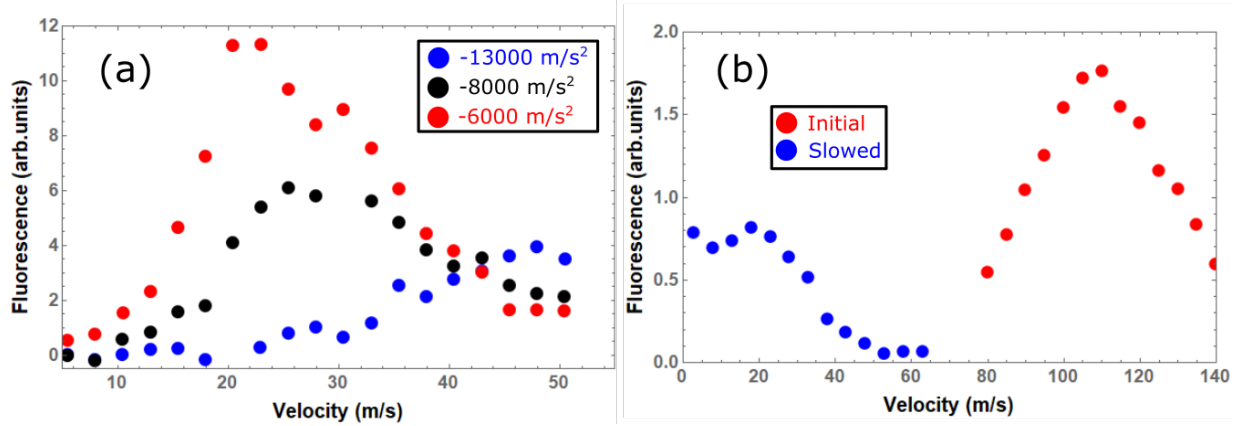


Figure 4.8:  $\Gamma/8$  slowing performance. (a). Slowing at different deceleration rate. (b). Slowing result at optimal slowing parameters

We first explored the chirped slowing by scanning the deceleration rate as shown in Figure 4.8 (a). In the experiment, we kept the initial ( $v_i=110 \text{ m/s}$ ) and final ( $v_f=20 \text{ m/s}$ ) velocities fixed while only varying the deceleration rate  $a$ . In this case, the deceleration distance  $s$  changes accordingly,  $v_f^2 - v_i^2 = 2a \times s$ . The optimal deceleration rate is  $\sim 6000 \text{ m/s}^2$ , indicating a scattering rate of 1 MHz. It is a factor of 3 smaller than the effective scattering rate  $\Gamma/8$  calculated based on the repumping scheme. We've checked that all transitions are well saturated and properly mixed, thus the discrepancy in decelerations remains unclear.

We also varied the Pockels cell frequency for slowing. Pockels cell chops the polarization of slowing beam to prevent the polarization dark state. Since the scattering rate is  $\sim 1 \text{ MHz}$ , there is no strong dependence from 1 MHz to 5 MHz.

For a 100-20 m/s slowing, slowing beams are typically switched on at  $\sim 2 \text{ ms}$  after the Yag ablation pulse. This is mostly due to the exit time of YO from the cell, which is  $\sim 1.5 \text{ ms}$ .

Combining all the upgrades, the  $\Gamma/8$  scheme delivered  $\sim 2 \times 10^5$  molecules within the trappable velocity. The slowing efficiency from 120 m/s to 5 m/s is  $\sim 4\%$ . This provides enough slow molecules for the trapping stages.

#### 4.4 Slowing Scheme with $A'^2\Delta_{3/2}$ Repumped

To prevent the leakage into  $N=0$  and  $N=2$  dark states, we can also directly repump the  $A'^2\Delta_{3/2}(J' = 3/2(-))$  state into  $B^2\Sigma^+(J = 1/2(+))$  state, as shown in Figure 4.9. The  $B^2\Sigma^+$  to  $X^2\Sigma^+$  transition is very diagonal with most of the decays into  $v=0, 1$  and  $2$  where the vibrational states are already repumped. The proposed scheme decouples  $N=0$  and  $N=2$  from the main ground state  $N=1$ , which increases the photon scattering rate by 15% but most importantly, reduce the loss during cooling. The coupling to the  $N=1$  state deteriorate the cooling, which will be detailed in section 6.1.2. In the current repumping scheme, to achieve a cold temperature, the  $N=0$  rotational repumper is switched off during the gray molasses cooling, resulting in a 50% of molecules loss. This loss will be prevented in the new scheme. In the new scheme, there are 4 manifolds coupled in the excited state( $n_e = 4$ ) and 24 manifolds involved in the ground state( $n_g = 24$ ). This results in an effective scattering rate [75, 76]  $\Gamma_{Scatter} = \frac{n_e}{n_g+n_e}\Gamma$  of  $\Gamma/7$ .

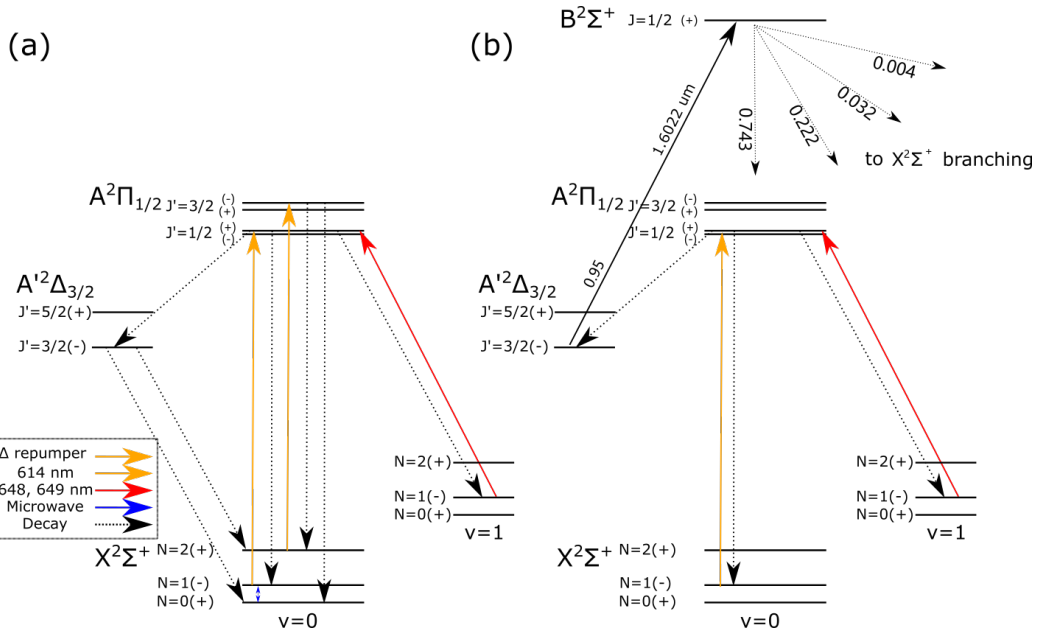


Figure 4.9: (a). Current repumping scheme. (b). New repumping scheme with  $A'^2\Delta_{3/2}(J' = 3/2(-))$  directly repumped to  $B^2\Sigma^+$ . This scheme doesn't significantly increase the scattering rate but prevent the loss during the gray molasses cooling.

## Chapter 5

### 3D Magneto-Optical Trap of Yttrium Monoxide

After slowing the molecules, it's important to trap them and keep them locally confined. Magneto-optical trap(MOT) is a widely used technology in atomic physics to produce samples of cold, trapped, neutral atoms. It combines laser cooling and a spatially-varying magnetic field to create the trapping forces. Since the first proposal on making a molecular MOT in 2008 [54], over the past 12 years, there are only a few molecules that have been trapped in MOT [91, 55, 56, 57, 58]. In this chapter, we discuss different MOT schemes on a type II cooling transition, present the implementation of the MOT in three-dimensions along with the comparison between RF and dc MOT performances.

#### 5.1 Magneto-optical Trapping Theory

Building on laser cooling, the first magneto-optical trap(MOT) was demonstrated in 1987 [115]. A typical MOT is formed from the intersection of a weak quadruple magnetic field and three pairs of circularly-polarized red-detuned beams. A simplified 1D MOT configuration is shown in Figure 5.1.

A magnetic field gradient is generated by a pair of anti-Helmholtz coils, creating a spatially varying energy level due to the Zeeman effects. We first focus on the traditional MOT setup(Type I MOT), as shown in Figure 5.1 (a). For a  $J=0$  to  $J=1$  transition, the magnetic field splits the three sublevels( $m_j = 0, \pm 1$ ) of the excited state, whereas the ground state remains unchanged. A pair of red detuned lasers with  $\sigma^+$  and  $\sigma^-$  polarizations are sent from opposite directions. Because



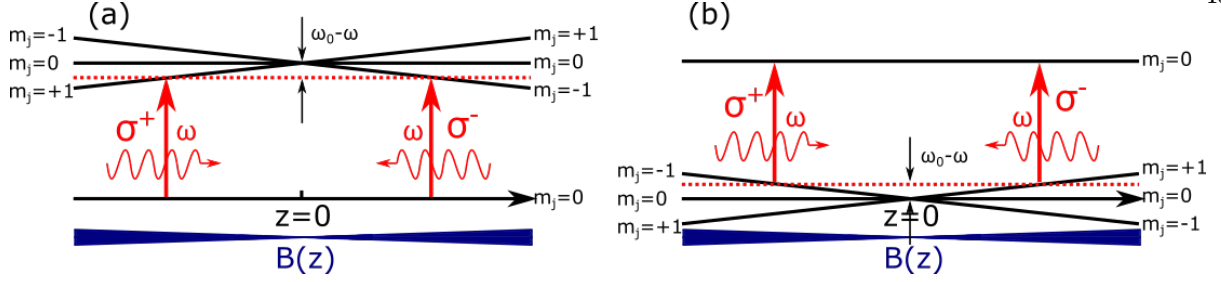


Figure 5.1: Arrangement for a MOT in 1D. (a). Type I MOT. In the magnetic field gradient, the Zeeman splitting of  $m_j = 0, \pm 1$  states depends on the position of the atom. The counter propagating beams with different polarization and the transition selection rules lead to an imbalance in the radiative force from the laser beams that pushes the atom back towards the centre of the trap. (b). Type II MOT. Trapping force doesn't exist due to the dark manifolds in the ground state.

of the transition selection rule, atoms are excited from ground state to  $m_j = -1$  state by absorbing a  $\sigma^-$  photon. Similarly, atoms are excited from ground state to  $m_j = +1$  state by absorbing a  $\sigma^+$  photon. If the atoms are displaced to the right of the origin, it preferentially absorbs the laser from the right which is closer to resonance, and thus receives a kick back towards the origin. Similarly, if the atoms are displaced to the left, it prefers the photon from the left, and thus receives a kick towards the origin as well. The excited state atoms would then decay back down to  $J=0$  state, resulting in a force averaged to zero and the whole process continues. The total force [102] on the atoms is given by the sum of  $\sigma^+$  and  $\sigma^-$  beams where

$$F_{\text{MOT}} = F_{\text{scatt}}^{\sigma^+} (\omega - kv - (\omega_0 + \beta z)) - F_{\text{scatt}}^{\sigma^-} (\omega + kv - (\omega_0 - \beta z)) \simeq -2 \frac{\partial F}{\partial \omega} kv + 2 \frac{\partial F}{\partial \omega_0} \beta z,$$

with  $F_{\text{scatt}}$  as the scattering force from a single beam

$$F_{\text{scatt}} = \hbar k \frac{\Gamma}{2} \frac{I/I_{\text{sat}}}{1 + I/I_{\text{sat}} + 4\delta^2/\Gamma^2}.$$

The term  $\omega_0 + \beta z$  is the resonant absorption frequency for the  $\Delta m_j = +1$  transition at position  $z$ . Similarly,  $\omega_0 - \beta z$  is that for the  $\Delta m_j = -1$ . The Zeeman shift at displacement  $z$  is

$$\beta z = \frac{g\mu_B}{\hbar} \frac{dB}{dz} z,$$

where  $g = g_j$ . Therefore, the force depends on the frequency detuning  $\delta = \omega - \omega_0$ , so

$$F_{\text{MOT}} = -\alpha v - \frac{\alpha\beta}{k}z, \quad \alpha = \frac{\partial F}{\partial \omega} = \frac{8\hbar k^2 \Delta I / I_{\text{sat}}}{\Gamma \left(1 + I / I_{\text{sat}} + \frac{4\Delta^2}{\Gamma^2}\right)^2}.$$

This is the expression describing a damped harmonic oscillator. Therefore, the atoms are confined inside the trap under the restoring and viscous force.

### 5.1.1 Type II MOT

Unlike atoms, a molecular MOT is more difficult due to its complex energy structure. For a typical type I MOT on a  $J \rightarrow J+1$  transition, as shown in Figure 5.1 (a), excited atoms always decay back to the same ground state. Therefore, a large number of photon scatterings becomes possible. However, in order to maintain the rotational closure for molecules [54],  $N=1$  is chosen as the ground state, resulting in a  $F \rightarrow F-1$  transition, a type II MOT. As a result, there are more ground states than the excited states where molecules can be pumped into dark states in the ground [116] under a fixed laser polarization and magnetic field gradient, as shown in Figure 5.1 (b). For example, molecules on  $m_j = +1$  can absorb a  $\sigma^-$  photon and get pumped to  $m_j = 0$  excited state. They become dark to the  $\sigma^-$  laser if they decay to  $m_j = 0, -1$  states. To avoid these dark states, there are two solutions: rf MOT [117] and dc dual frequency MOT [118, 119].

## 5.2 Experiment Setup for RF MOT

As first described in Ref. [91], in an rf MOT, we modulate both magnetic field direction and laser polarization at a rate faster than the optical pumping rate. Typically, the optical pumping rate into dark state is on the order of 1 MHz. The switching needs to be fast enough for the change to be non-adiabatic.

### 5.2.1 RF MOT Coils

The typical MOT coil is realized by two spools of magnet wires in an anti-Helmholtz configuration. However, a normal drive for the coils can not create B field gradient of  $\sim 10$  Gauss/cm

oscillating at MHz, which is limited by the required current and voltage at such high frequency. We use a resonant tank approach to drive the coils sinusoidally, as implemented in Ref. [91]. Several vacuum compatible coils are designed and constructed.

Switching current at high frequency gives rise to a large inductive spike, creating a huge voltage. The stray electric field then mixes the opposite parity states and causes extra loss into the wrong parity states, which will be detailed in Section 5.4. To reduce the inductance, coils are made small and placed inside the vacuum chamber. In this case, heating becomes an issue inside the vacuum. At RF frequencies, the current in the conductor is localized near the surface in a limited thickness called skin depth

$$\delta = \sqrt{\frac{2\rho}{\omega\mu}},$$

where  $\rho$ ,  $\omega$ ,  $\mu$  are resistivity of the conductor, angular frequency of the current and permeability of the conductor. The skin depth of copper at 5 MHz is  $\sim 35 \mu\text{m}$ . Therefore, the resistivity is large due to the small the cross section, which produces lots of heat.

### 5.2.2 First 3D RF MOT Coil Design

We use a coil directly bonded on an amorphous aluminum nitride (AlN) substrate that has a very high thermal conductivity ( $\sim 200 \text{ W/m}\cdot\text{K}$ ). Therefore, the heat generated by the copper coils is quickly conducted to the insulated AlN board. However, AlN is much harder than alumina, making the fabrication very difficult. All our coils are designed and drawn by ourselves and then fabricated by REMTEC.

The first coil design used in 3D rf MOT paper [58] was previously described in [114], so here we only emphasize the most salient details. As shown in Figure 5.2 (a), four boards with two slightly different designs are used to increase the magnetic field. There is one copper spiral on both sides of the board and a Kapton film is sandwiched between the boards to avoid direct contact and the possible arcing. There are 4 layers and total 28 turns on each half of the MOT coil. A copper C clamp is installed on the left side to conduct the heat to the water cooled copper finger. With this coil setup, we generated a magnetic field gradient of  $\sim 20 \text{ Gauss/cm}$  modulating at 5 MHz

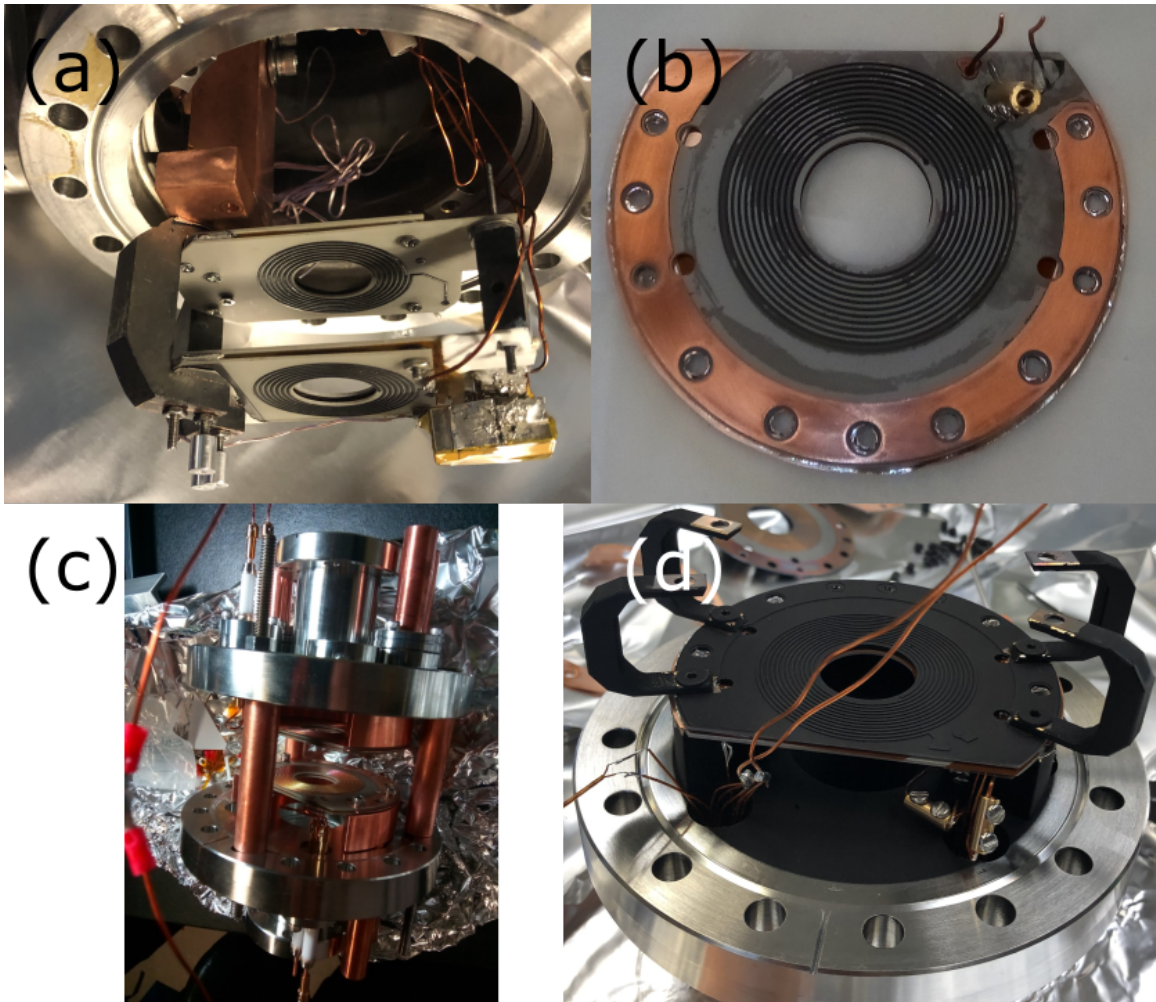


Figure 5.2: Different MOT coil designs. (a). First MOT coil design used in 3D rf MOT paper. There are 7 turns on each side of the board. 2 boards are used on each half of the coil. (b). Current MOT coil design used in 3D dc MOT. (c). Coil mount for good thermal conductivity. (d). Coil mount for better pumping conductance. The blackening is achieved by the black paint, MH2200.

with a working temperature of 50 °C. To reduce the unwanted light scatter, the coil is blackened by oxidizing [120] the copper traces while the AlN substrate remains reflective. This design has several drawbacks. The high voltage capacitors were installed inside the vacuum, therefore, the resonant frequency of the LC tank circuit can't be tuned without opening the vacuum. The coils weren't centered properly for years due to the limited accesses. In addition, the coils remained hot during normal operation due to the limited thermal contact.

### 5.2.3 New RF MOT Coil Design

To overcome these problems, a new pair of coils was designed. The pictures of a single board and the coil assembly are shown in Figure 5.2 (b) and (c). Compared with the previous design, we nearly doubled the number of traces on each surface for higher field gradient and introduced a copper layer on the edge for better heat conductance. The center hole is larger than that of the old coil, allowing a larger MOT beam to capture more molecules. The boards are cut for potential optics inside the vacuum, for example, an in-vacuum lens. The detailed drawing of the coils are displayed and discussed in Appendix C.

### 5.2.4 Driving RF Coil

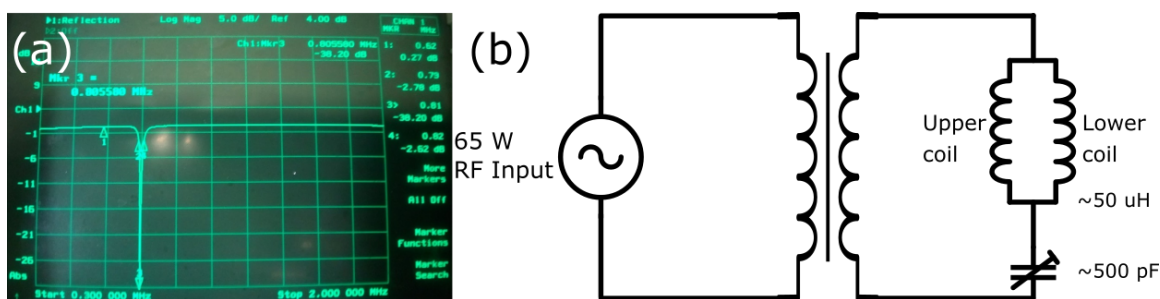


Figure 5.3: (a). Measure the reflection of new coils to determine the resonant frequency ( $f_0=0.8$  MHz) and the quality factor ( $Q\sim 40$ ). (b). Impedance matching circuit diagram for rf MOT coils.

The new boards, Figure 5.2 (b), consist of a 12 turns copper spiral bonded on both side of the AlN substrate. The spiral is 0.012" thick with a width of 0.025" and a gap of 0.025". Compared with the previous design, the new design increases the inductance(resistance) by a factor of 4.6(2.3). A high voltage variable capacitor is located outside the vacuum, giving a tunable frequency between 0.5 to 2 MHz. With a capacitance of  $\sim 500$  pF, the quality factor  $Q$  of the coil is  $\sim 40$  and the resonant frequency is 0.8 MHz, as shown in Figure 5.3 (a). For this configuration, we tested that the arcing didn't occur at 4 kV/cm where the magnetic field gradient is 40 Gauss/cm.

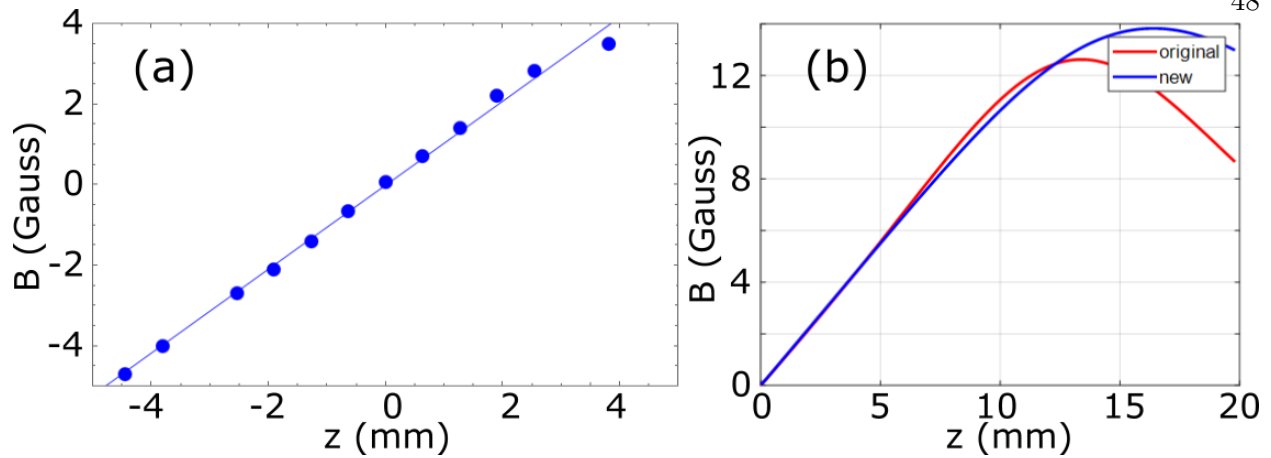


Figure 5.4: (a). Axial magnetic field measurement. The field is very linear in a 8 mm region. (b). Calculated axial magnetic field with different coil configuration. Both configurations provide a good linearity within 1 cm.

To drive the RF coil, we use a commercial RF amplifier (RM Italy HLA-305V) that produces  $\sim 65$  W, resulting in a field gradient of 20 Gauss/cm at 0.8 MHz. The impedance matching is achieved by a wrapped toroidal transformer. The magnetic field is quite linear in a 8 mm region, as measured in Figure 5.4 (a), matching the calculated result in Figure 5.4 (b). 11 Gauss/cm·A is measured along the axial direction, in agreement with the calculation. The new coils are directly mounted to the stainless steel vacuum flanges as shown in 5.2 (c). Therefore, the coil center is very well aligned to the geometric center of the chamber. At the beginning, the coil was connected in series to ensure that they are driven with the same current. Later, we switched to parallel configuration as shown in Figure 5.3 (b) to reduce the potential E field associated loss. We will discuss this in Section 5.4.

### 5.2.5 Cooling the Coil

When driving the coils with 20 Gauss/cm (RMS), 50 watts of heat are generated inside the vacuum. With limited thermal convection, the thermal conductance becomes critical to prevent outgassing and thermal gradients. In the new design, a copper layer was bonded on the edge of the board for better thermal contact. The copper "horse shoe" which mounts the coils were

attached onto four 0.5" copper feedthroughs. An indium foil was sandwiched between all joints to increase the thermal conduction. These copper feedthroughs were water cooled at the outside of the vacuum. Using a water-ethylene glycol(EG) mixture in the chiller, the cooling water were maintained at  $-20\text{ }^{\circ}\text{C}$ . This allows the coils to run at full duty cycle with a temperature of  $\sim 40\text{ }^{\circ}\text{C}$  in vacuum. The thermal performance was measured by two thermistors located at the highest and lowest temperature spots of the coil. The temperature difference on the board is less than  $10\text{ }^{\circ}\text{C}$ .

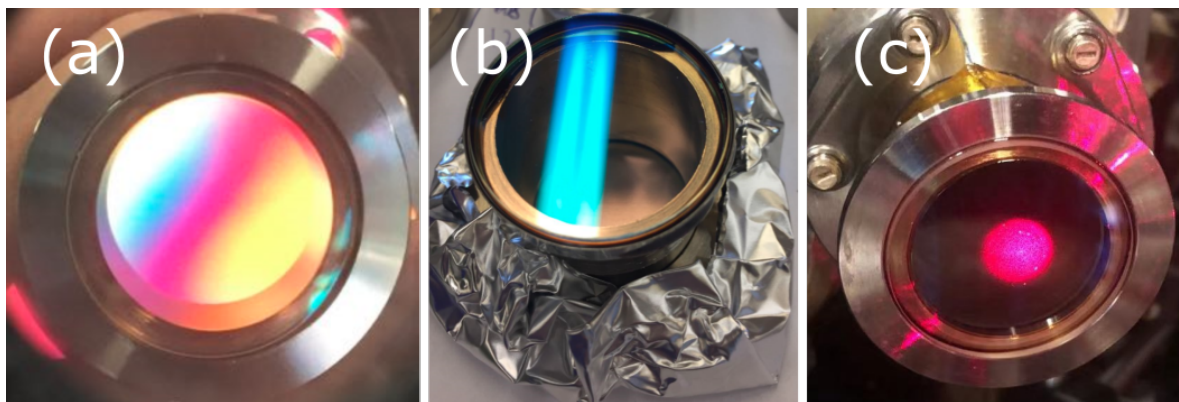


Figure 5.5: (a). Stress inside the window, checked via polarized stress tester. The color is due to the birefringence, indicating a strong stress in the window. (b). Window glued on thin wall vacuum flange. The stress is greatly reduced. (c). Scattered light from our custom viewport.

### 5.2.6 Reducing the Scattered Light

In our experiment, YO molecules are detected using light induced fluorescence(LIF). Therefore, it's necessary to reduce the light scattered by the stainless steel chamber and all coil accessories. There are many blackening methods including copper blackening [121] and various types of black paints. Previously, we oxidized a series of copper shields and put them inside vacuum to block all scattered light. The method involves bringing a sodium hydroxide(NaOH) and sodium chlorite( $\text{NaClO}_2$ ) solution to a boil and immersing the copper for several minutes. However, it only works for copper surfaces and it's prohibitively hard to machine this copper to fit all surface necessary to block scattered light. In addition, the copper oxide coating can be easily removed by rubbing the surfaces. For an improved solution, we spray a black paint(Alion MH2200) all

over our chamber due to the ease of application and great performance. This paint is silica-based, nonconductive, UHV compatible and scratch resistive [122, 123, 124]. It can be easily applied to all surfaces including aluminum, copper, stainless steel and aluminum nitride. We sprayed the paint over all surfaces using an air brush and baked them in air at 200 °C for 4 hours to eliminate possible outgassing. Figure 5.2 (b) and (d) shows the coil before and after the blackening. The only drawback is that the coating is hard to remove.

It is suggested [99] that a custom window should be used to further reduce the light scatter. During the brazing process, the commercial UHV windows are covered with a thin layer of grime which causes high scattering. We tried to epoxy a 40 mm N-BK7 window with NIR I coating(Edmund optics 83-476) onto a CF to KF adapter(Kurt J. Leskser F0275XQF40). The epoxy(Epotek 353 ND) [125] we used requires a minimum cure temperature of 80 °C and 150 °C for full bonding strength according to the specification sheet. The high cure temperature combined with the mismatch of thermal expansion coefficient between stainless steel and N-BK7 introduces a large stress in the window, as shown in Figure 5.5 (a). If fused silica is used for better surface quality, the window would even crack after the cure due to its small thermal expansion coefficient. To overcome these problems, we machined the vacuum flange to 0.01” thickness which reduces the stress, as shown in Figure 5.5 (b). This was originally developed by Housekeeper for direct metal to glass seal where the thickness is normally  $\sim 0.001$ ”. The epoxy is also applied on the side of the window for better performance. With this design, the stress in the window is greatly reduced. However, the viewports still scatter  $\sim 0.25$ -1% of laser light, as seen in Figure 5.5 (c). This can be attributed to the grime introduced during the curing at high temperature. In the future, a low temperature epoxy(Epotek 032-3M) should be used which is able to cure at room temperature.

### 5.2.7 Detection system for RF MOT

The detection system shown in Figure 5.6 was used for the 3D rf MOT [58]. We detected 614 nm fluorescence and filtered the 648, 649 nm vibrational repumpers with color filters(Edmund 84-118). Irises are placed in the image plane between lens sets to block the unwanted scattering. A



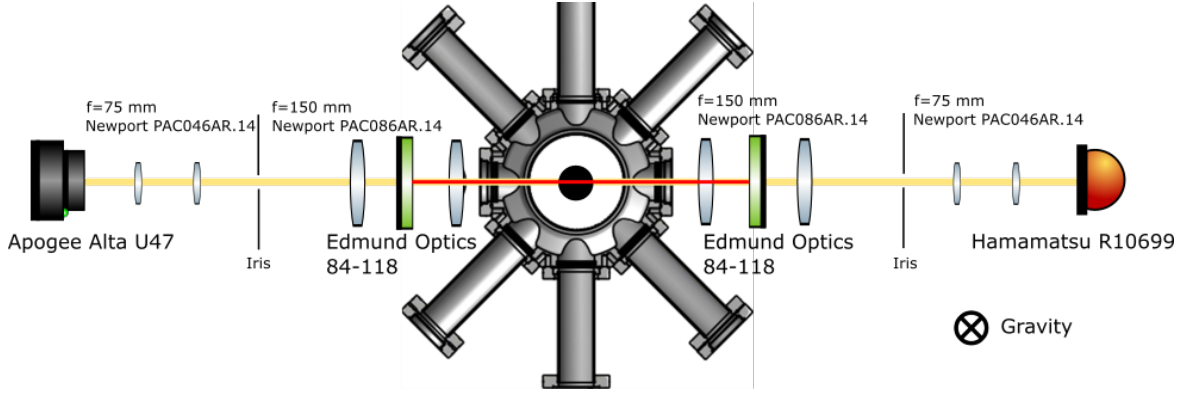


Figure 5.6: Detection system for the rf MOT. Two 2 inch, 150 mm focal length and two 1 inch, 75 mm focal length lenses are used on each side. An iris is placed at the focal plane to block the unwanted light scatter. There is a color filter blocking the vibrational repumpers.

PMT(Hamamatsu R10699) provided time resolved signals and a CCD(Apogee Alta U47) recorded spatial information. PMT receives the photons and generates the photon current. The current goes through a transimpedance amplifier and is then counted by a multichannel scaler(SRS 430). The amplifier was designed and built by the electronic shop in JILA. With a high photon flux, the photo current pulses have a high chance to overlap with each other. In this case, the multichannel scaler can not distinguished the pulses, resulting in a saturation. This can be improved by inserting a correction factor [126]. Both PMT and CCD systems are similarly designed and orthogonal to the molecule beam. The collection efficiency of the PMT(CCD) is  $3.3 \times 10^{-4}$  ( $1.4 \times 10^{-3}$ ). The CCD alignment is confirmed by imaging a notched threaded rod in the MOT center [114].

## 5.3 RF MOT Performance

### 5.3.1 1D RF MOT

To study the 3D RF MOT, we first explored the 1D rf MOT. The slowing was unnecessary since the transverse velocity of the beam is on the order of  $\sim 5$  m/s, comparable to the trapping velocity. 1D MOT allowed for optimization of the correct phase between the laser polarization and the magnetic field direction.

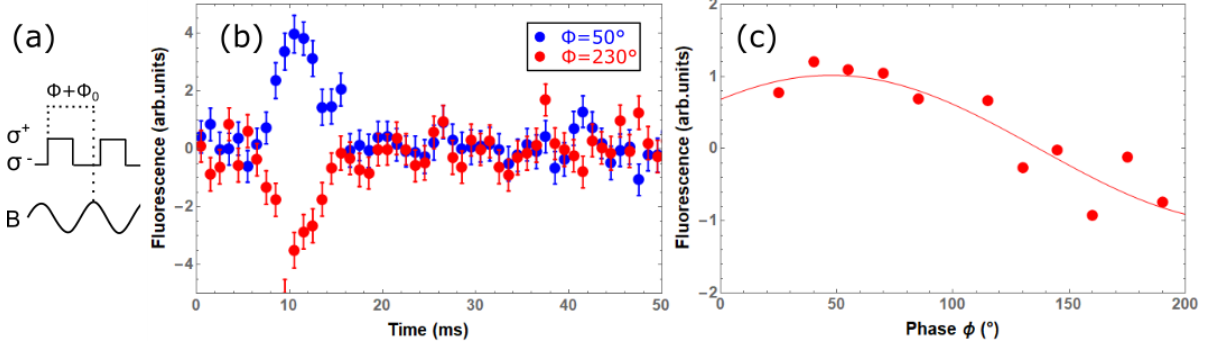


Figure 5.7: 1D RF MOT. (a). Phase between laser polarization and magnetic fields in rf MOT. (b). 1D rf MOT at opposite phase. The signal is phase subtracted ( $\phi - (\phi + 180^\circ)$ ). Molecules are generated at time zero. (c). Differential 1D MOT signal at different phase.  $50^\circ$  is the optimal MOT phase.

Three lasers are red detuned to address  $G=0 F=1$ ,  $G=1 F=0$  and  $G=1 F=1,2$  states. We sent 3 pairs of beam into the chamber and looked at the fluorescence detected by a beam with limited size. As discussed in the previous section, both magnetic field direction and laser polarization are modulated at a rate faster than the optical pumping rate to prevent molecules from going dark. When the correct phase is chosen, the molecule beam is compressed due to the trapping force. Similarly, if the phase is wrong, the trapping force becomes weak and even expand the beam. With a small detection beam, a compressed beam has more counts than an expanded beam, as shown in Figure 5.7 (b). The phase is scanned to reach the optimal trapping condition, as shown in Figure 5.7 (c). The data was measured at a detuning of 5 MHz and a magnetic field gradient of 10 Gauss/cm.

### 5.3.2 3D RF MOT

To capture molecules in a 3D rf MOT, it's necessary to slow molecules down to 5 m/s. As it has been discussed previously in Section 3.2 and 4.3.3, we removed the second stage of the buffer gas cell, coated the cell, installed an in-vacuum shutter and implemented the slowing scheme from  $\Gamma/14$  to  $\Gamma/8$ . We first checked that we can slow molecules down to  $\sim 5$  m/s. It takes  $\sim 16$  ms to slow molecules from 120 m/s to 5 m/s. Then we looked for a slow decay signal of trapped

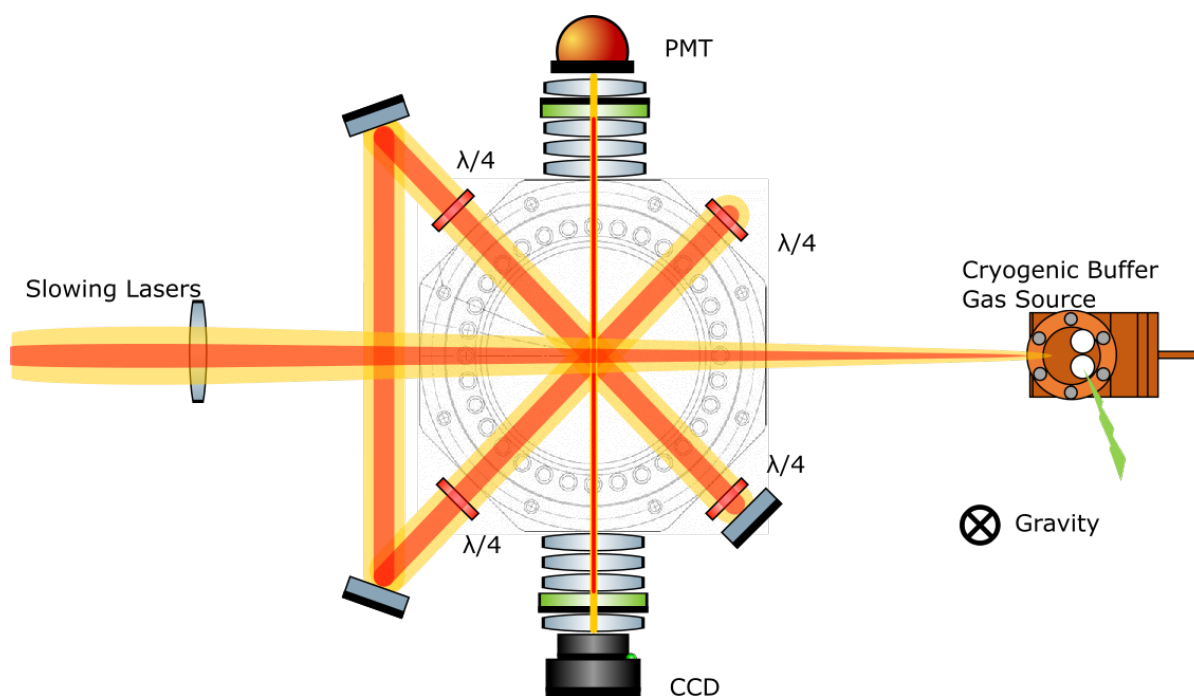


Figure 5.8: Experiment layout for 3D rf MOT Setup. MOT beams are circulated for a strong intensity.

molecules using a PMT. Limited by the laser intensity of  $v=0$  and  $v=1$ , we circulated the trapping and repumping beams instead of using three independent pairs. The beam first entered through the bottom port, then reflected down to the octagonal plane, as shown in Figure 5.8. After reflecting into the last port, the beam was retroreflected back.

We had been struggling with a weak MOT signal for a very long time until we extended the slowing sequence by an extra 12 ms, which was first discovered by the Harvard group. Apparently, they underestimated the molecular beam velocity and overestimated the trapping velocity of the MOT. In our case, the Doppler sensitive detection would only overestimate the velocities, as described in Section 4.2.2. Therefore, we believe it's the over slowing that helped load more molecules into the MOT. As we can see in Figure 5.9 (a), more molecules were loaded into the MOT with more slowing time and reached saturation at  $\sim 11$  ms. The optimal slowing time of 28 ms almost doubled the time we had seen as the arrival time of 10 m/s molecules, which was only  $\sim 16$  ms. Figure 5.9 (b) shows a Doppler detection at the end of the slowing, molecules are slowed

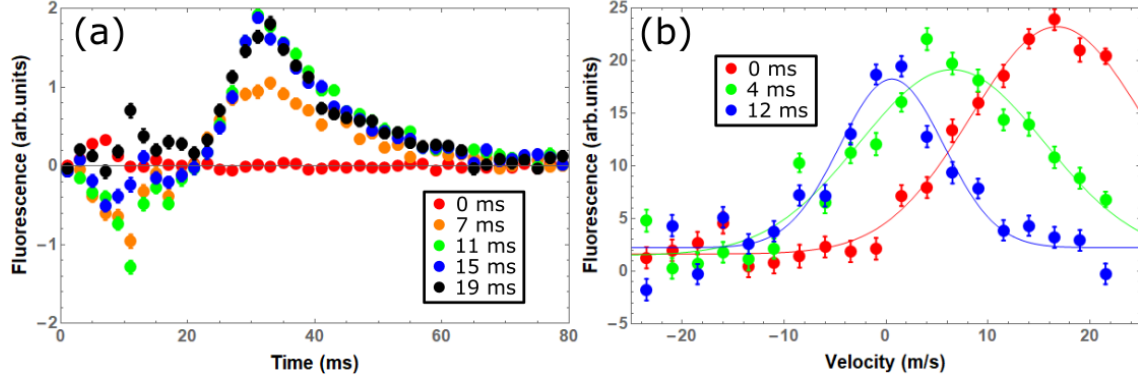


Figure 5.9: (a). 3D rf MOT loading with different extra slowing time,  $\Delta = 2\pi \times 5$  MHz. The original slowing time is 16 ms. The trace is phase subtracted ( $\phi - (\phi + 180^\circ)$ ). Extra slowing time after the original slowing sequence helps the MOT loading. (b). Doppler detection at the end of slowing with different extra slowing time. The center velocity is shifted from  $\sim 18$  m/s to 0 m/s with extra 12 ms at the end of the original slowing sequence. This "over slowing" apparently helps the MOT loading.

further to about 0 m/s and they're even "over slowed" with the extra slowing time. Apparently, the trapping velocity of the rf MOT is really lower than expected.

The MOT beams have a  $1/e^2$  beam waist of 10 mm and can have a maximum of 25 mW  $v=0$  of light per beam. The power on each hyperfine states were set to be equal.  $v=1$  and  $v=2$  repumpers are typically 25 and 8 mW per MOT beam. The light induced fluorescence detected by PMT with various parameters is shown in Figure 5.10. MOT loading is optimal with a 12.5 mW trapping laser of 5 MHz red detuning. Initially, the MOT loading is limited by the magnetic field gradient which only reaches 13 Gauss/cm. With some technical upgrades, we achieved a rms field gradient of 20 Gauss/cm with 60 W input. The phase dependence was not very strong as well.

The temperature of the MOT was determined by time-of-flight(TOF) expansion. A thermal cloud would expand in free space where the expansion rate depends on the temperature. In our experiment, we turn off MOT beams and magnetic field simultaneously for various amount of time  $t$ , followed by a 2 ms resonant beam for detection. A short detection time(2 ms) and typical intensity( $1.3 \text{ mW/cm}^2$ ) are used to reduce any heating effects during imaging. The images of the released molecular cloud are shown in Figure 5.11 (a), with the cloud becoming larger at longer

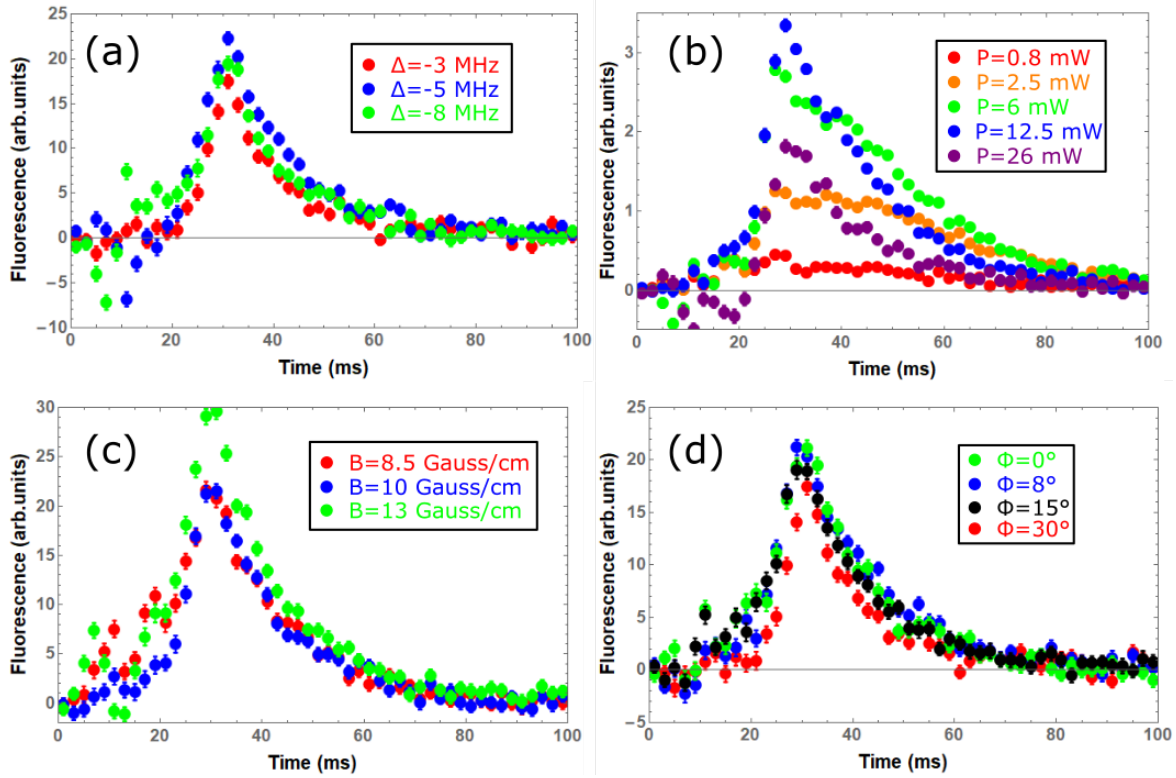


Figure 5.10: Characterisation of 3D rf MOT. (a). Different  $v=0$  detunings. (b). Different  $v=0$  powers. (c). Different magnetic field gradients. (d). Different phases  $\phi$  between magnetic field direction and laser polarization.

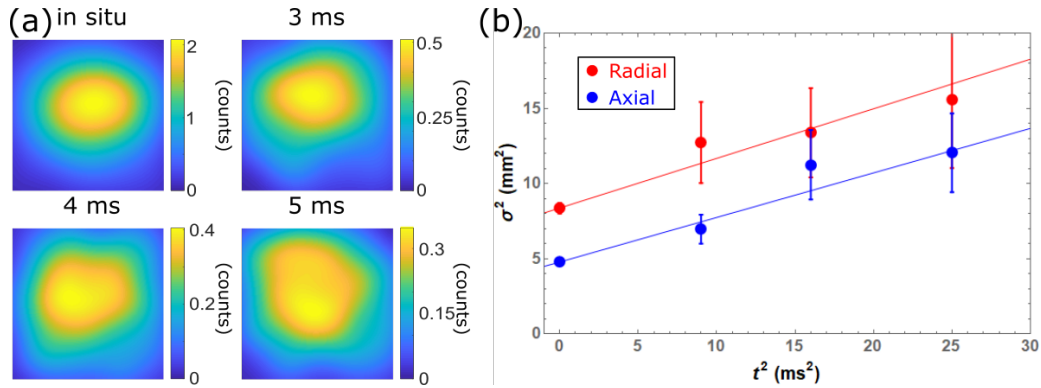


Figure 5.11: Time-of-flight expansion for temperature measurement. (a). Image of released molecule cloud, the size of each image is  $1 \text{ cm} \times 1 \text{ cm}$ . We can see the cloud expands with time. (b). The measurement of the Gaussian width  $\sigma$  of the cloud as a function of free flight time  $t$ . The slope is proportional to the temperature. We extract the radial and axial temperature of the MOT to be  $4.1(5)$  and  $3.8(5)$  mK.

release time. We extracted the radial and axial temperature by fitting the Gaussian width  $\sigma$  with the release time  $t$

$$\sigma_t^2 - \sigma_0^2 = \frac{k_B T}{m_{YO}} t^2$$

and the temperature of the cloud is  $T = T_{axial}^{1/3} T_{radial}^{2/3}$ .

Unlike typical type I MOT, the temperature is much hotter than the Doppler temperature,  $T_D = 116 \mu\text{K}$ . This has been observed in all molecular MOT [57, 127, 56] using type II transitions. It's theorized that the hot temperature is resulted from the Sisyphus heating mechanism [128]. The heating might also come from the unwanted sidebands on the MOT beams, which are introduced by the Pockel cell for polarization chopping. Since the hyperfine splittings are  $\sim$ tens of MHz, we reduced the Pockel cell chopping rate from 5 MHz to 1 MHz after coil modification, but it didn't make a difference. To further cool the molecules, intensity can be ramped after trapping. However, the molecular cloud's size would increase rapidly due to the limited restoring forces. Instead, we apply gray molasses cooling which is detailed in the following Chapter 6.

## 5.4 Molecule Loss by Parity Mixing

The MOT lifetime was determined by measuring the decay of the MOT fluorescence. As we can see in Figure 5.10 (b), MOT loading was enhanced with more trapping power while the lifetime become shorter at higher scattering rates. The MOT decay time versus power curve is plotted in Figure 5.12. The fitting is inversely proportional to power, indicating the molecules are pumped into dark states. This limits the number of trapped molecules and our MOT lifetime.

As we mentioned earlier in Section 4.1, YO possesses an intermediate state  $A'^2\Delta_{3/2}J' = 3/2(-)$  which introduces extra loss into opposite parity states due to the two photon process. The  $\Lambda$  splitting between  $A'^2\Delta_{3/2}J' = 3/2(-)$  and  $J' = 3/2(+)$  is only  $\sim 0.2$  MHz. These states can be mixed by an external electric field, for example, our rf MOT coil. Therefore, molecules on  $J' = 3/2(+)$  state would decay into  $N=1$  and  $N=3$  state where  $N=3$  is not repumped, as shown in

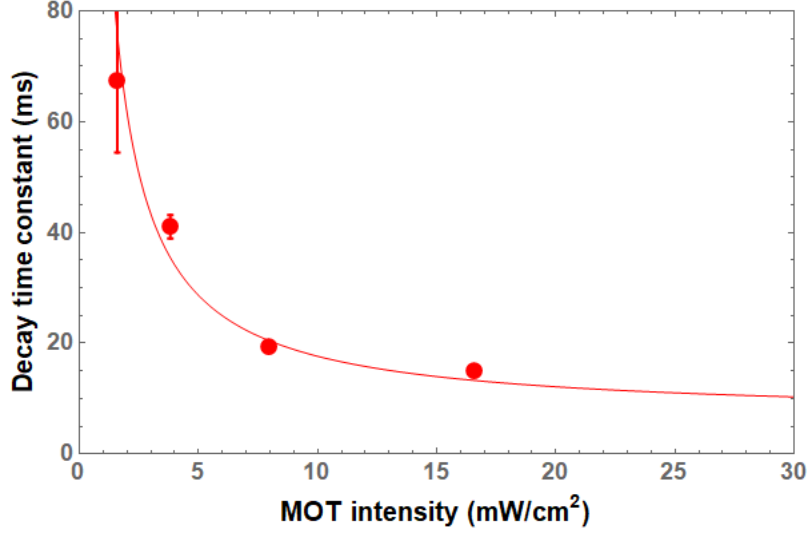


Figure 5.12: MOT lifetime at different intensities of the trapping beam. The solid line is a fit to the function  $t = a/P + b$ , where  $a$  and  $b$  are fitting parameters. This indicates the molecules are pumped into dark state, limiting our MOT lifetime

Figure 5.13 (a). The remixing rate into  $N=3$  dark state is:

$$\frac{1}{\tau} = \frac{(d_{A'}E/3)^2}{4\omega_{\Lambda}^2 + \Gamma^2/4} R_{sc} q_{AA'}, \quad d_{A'} = 7.5D [77], \quad \omega_{\Lambda} \approx 0.1MHz$$

where  $d_{A'}$ ,  $\omega_{\Lambda}$ ,  $R_{sc}$ ,  $q_{AA'}$  are half of  $\Lambda$  doubling splitting,  $A'^2\Delta$  state electric dipole moment, scattering rate and branching ratio from  $A^2\Pi_{1/2}$  to  $A'^2\Delta_{3/2}$ .

The top and bottom coils are connected in a parallel configuration to reduce the stray electric field. For coils run at 1 MHz with 10 Gauss/cm and the electric field of  $\sim 1$  V/m leads to a lifetime of  $\sim 20$  ms at the scattering rate of 1 MHz. As a result, the leaking into  $N=3$  is limiting our rf MOT lifetime.

### 5.4.1 N=3 Spectroscopy

The  $N=3 \rightarrow J' = 5/2$  spectroscopy is taken to repump the  $v=0$   $N=3$  state. We excited the molecules on  $N=3$  state to  $A^2\Pi_{1/2} J' = 5/2(+)$  with a low intensity laser beam perpendicular to the motion of molecules and then collected the fluorescence. The laser frequency is modulated as described in Section 4.2.2, thus the entire spectrum is obtained in a single experiment.

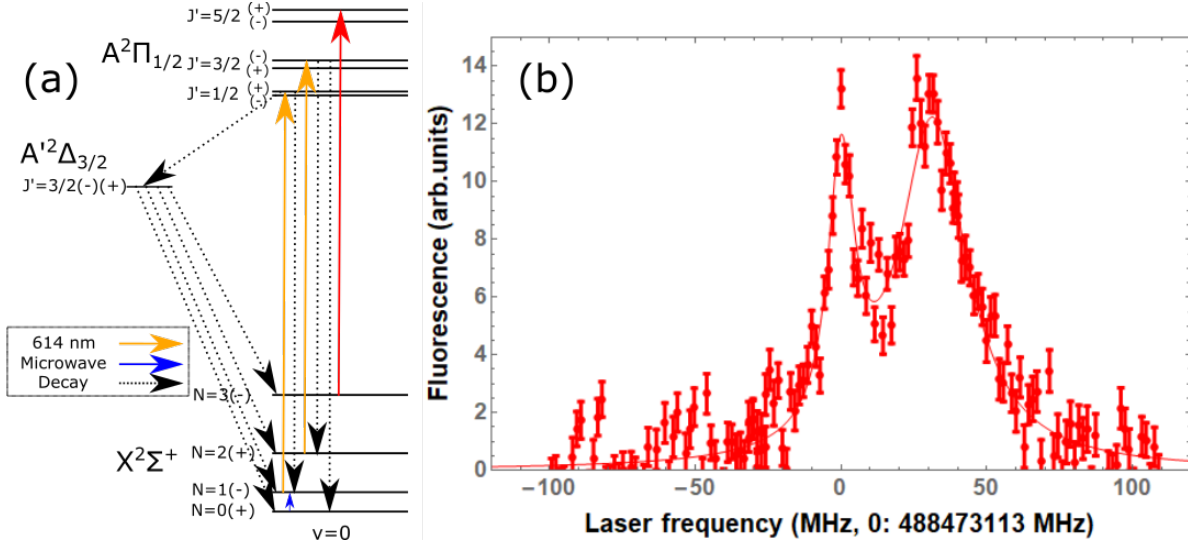


Figure 5.13: (a). Loss into  $v=0$   $N=3(-)$  due to the parity mixing on  $A'^2\Delta_{3/2}(J' = 3/2)$  state. The red arrow is the  $N=3$  repumper. (b).  $X^2\Sigma^+ N = 3(-) \rightarrow A^2\Pi_{1/2} J' = 5/2(+)$  spectroscopy, peaks are  $F=2$  and  $F=3$ .  $N=3$  repumper is parked at the right peak(488.473144 THz) for the best MOT performance.

### 5.4.2 N=3 Performance

As mentioned previously in Section 4.3.3, a dye laser was used to repump the  $X^2\Sigma^+ N = 2(+)$  state. The  $N=3$  repumper is set on the right peak in Figure 5.13 (b), which is  $\sim 9.8$  GHz lower than the  $N=2$  repumper. We generate sidebands on the dye laser by an EOM(Qubig EO09775M2) to address the  $N=3$  state. It is worth mentioning that the cooling transition on  $N=1$  is  $\sim 9.6$  GHz higher than the  $N=2$  repumper. Therefore, one of the EOM sidebands is only  $\sim 200$  MHz from the main cooling transition, which can potentially interact with molecules.



We studied the  $N=3$  performance in the dc MOT, which is different from rf MOT and will be discussed in the follow section. By inserting a resistor between the top and bottom coils, we can increase the electric field from 0.3 V/cm to 37 V/cm. The MOT traces without  $N=3$  repumper are shown in Figure 5.14 (a). In both cases, the number of trapped molecules and the MOT lifetimes are equal, indicating the  $A'^2\Delta_{3/2} J' = 3/2(\pm)$  parity has been fully mixed, even at 0.3 V/cm. With the  $N=3$  repumper, as shown in Figure 5.14 (b), the MOT lifetime increases from 34(1) to 57(1) ms and the molecule number increases by a factor of 2.

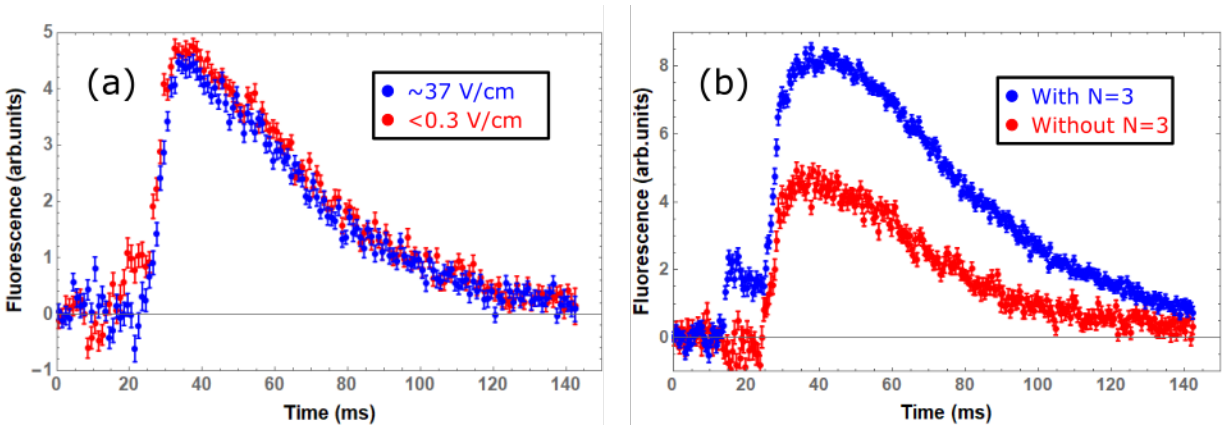


Figure 5.14: Repumping  $N=3$  state in dc MOT. The trace is subtracted (molecule on-molecule off) to take away the back ground scattering. (a). MOT without  $N=3$  repumper at different electric field. (b). DC MOT with/without  $N=3$  repumper. The electric field is 0.3 V/cm.

## 5.5 DC MOT

Instead of an rf MOT, A dc MOT [128, 119] can be exploited to remix the dark states as well. In the rf MOT, the remixing relies on diabatically switching the magnetic field. In the dc MOT, besides the red detuned laser, a blue detuned laser with opposite polarization is added to address the dark magnetic sublevels, as shown in Figure 5.15 (a). The laser setups of RF and dc MOT are shown in Figure 5.15 (b). We add another laser  $L_4$  with opposite detuning and polarization to address the dark magnetic manifolds.

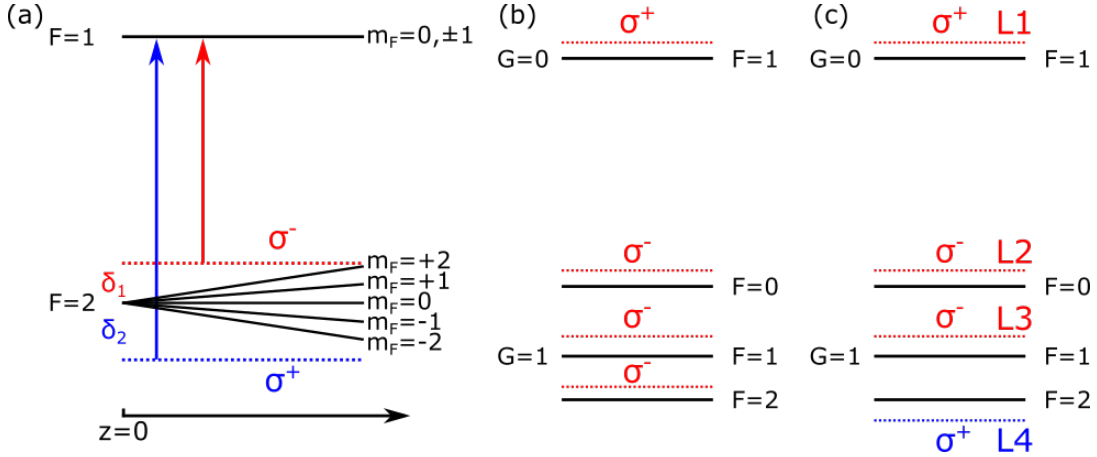


Figure 5.15: The optimal polarization scheme for a YO MOT. (a) Simplified dual frequency MOT setup.  $F=2$  is the ground state and  $F=1$  is the excited state. Compared to rf MOT with a single red detuned  $\sigma^-$  laser, a blue detuned  $\sigma^+$  beam is added to address the dark manifolds such as  $m_F = -1, -2$ . (b). rf MOT setup of YO. Only ground states are shown for simplicity. All beams are red detuned and polarizations are set based on the g factor. (c). DC MOT setup of YO. Only ground states are shown for simplicity. L3 and L4 with opposite polarizations around  $G=1$   $F=2$  provide trapping, while the L1 and L2 mainly repump the states.

### 5.5.1 DC MOT Performance

To generate the dc MOT beams, we equally split the main cooling laser into four beams L1, L2, L3, L4 with a diameter of 8.2 mm. We set a nominal intensity  $I = 1.4I_0$ , where  $I_0 = 2.7$  mW/cm<sup>2</sup> is the estimated saturation intensity. At this intensity, the optimal detunings for the hyperfine components, from top to bottom in Figure 5.15 (c), are tuned to be -5.8, -9, -5.8 and +2.6 MHz, resulting in a MOT lifetime of 90 ms. The magnetic field gradient is 12 Gauss/cm. Under these conditions, the molecular sample has a  $2\sigma$  diameter of 2.8 mm (3.9 mm) along the axial (radial) direction and a temperature of 2 mK, 2 times colder than the rf MOT (4 mK). The number of trapped molecules is  $1.1 \times 10^5$ , 7 times that reported in the work of rf MOT [58] and the peak spatial density is  $\sim 1 \times 10^7$  cm<sup>-3</sup>. I should mention that we increased the cell yield by  $\sim 5$  times after the rf MOT paper [58] was published.

The dual-frequency MOT results from the trapping on  $G=1$   $F=1,2$  states and also has contributions from the other two trapping mechanisms, red-detuned Type-I and red-detuned Type-II

MOT [118, 129]. To determine their relative contributions, we disable the blue-detuned component L4 in Figure 5.15 (c) and compare the MOT performance at different polarization settings of L1, L2 and L3. As we can see in Figure 5.16 (a), all states including  $G=0 F=1$  and  $G=1 F=0,1$  contribute to trapping under the correct polarization. When L4 is unblocked, the MOT produces 5 times more molecules and twice the lifetime as compared to the MOT with L4 blocked, as shown in Figure 5.16 (b). This feature clearly demonstrates that the dual-frequency trapping mechanism dominates the trapping force for the MOT [118].

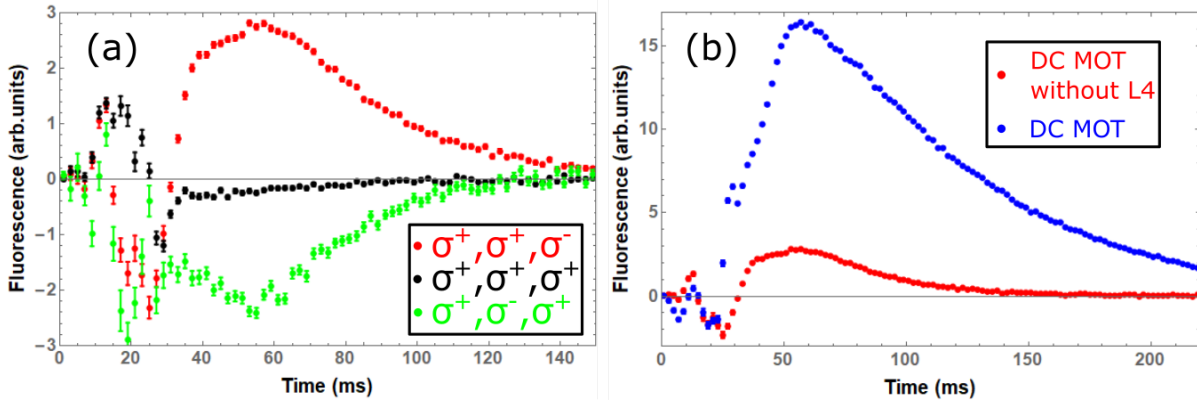


Figure 5.16: Test the dc MOT contribution. We plot differential MOT fluorescence between two opposite quadruple field directions. (a). Red detuned dc MOT with different polarizations. Polarizations of  $G=0 F=1$  and  $G=1 F=0,1$  beam are labeled in the legend. All beams contribute to trapping if the polarization is correct. (b). DC MOT with and without the blue detuned component. Apparently, the dual-frequency trapping mechanism dominates the trapping force for the MOT.

The YO dual-frequency MOT further benefits from the close spacing (3.5 MHz) of  $G=1 F=1$  and  $G=1 F=2$ , in comparison to the cooling transition linewidth of  $\Gamma=2\pi\times 4.8\text{MHz}$  [130]. Therefore,  $G=1 F=1$  and  $G=1 F=2$  both contribute to the dual-frequency trapping mechanism, increasing the overall trapping frequency. This feature may be responsible for our observation that the dc MOT traps approximately 20% more molecules than the rf MOT given that the other conditions remain the same, contrary to the results reported for CaF [57] and SrF [76].

We experimentally determine that the red detuned MOT shown in Figure 5.15 (b) already employs the correct polarization for both laser components addressing the  $G=1$  manifold. For

the two closely spaced states of  $G=1$   $F=1$  and 2, the corresponding laser polarization produces trapping for  $G=1$   $F=2$  and antitrapping for  $G=1$   $F=1$  [129], which shows that the force from  $G=1$   $F=2$  overwhelms that from  $G=1$   $F=1$ , consistent with the observation in [131] for SrF molecules.

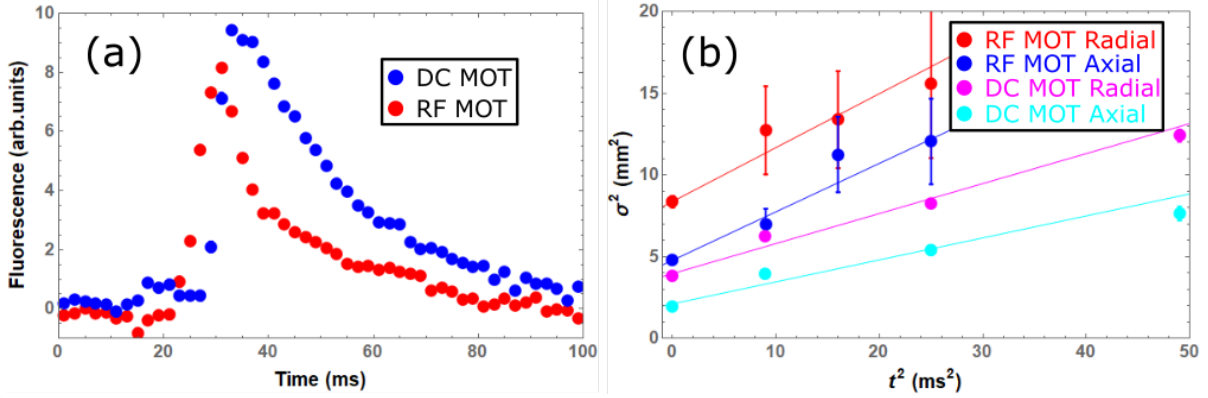


Figure 5.17: DC rf MOT comparison. We plot differential MOT fluorescence between two opposite quadruple field directions. (a). DC and rf MOT under same intensity ( $12 \text{ mW/cm}^2$ ,  $4.4 I_0$ ) and magnetic field gradient ( $12 \text{ Gauss/cm}$ ). (b). Time of flight expansion of dc and rf MOT for temperature measurement. The temperature of dc MOT is 2 mK, colder than rf MOT (4 mK).

In general, we trap  $\sim 7$  times more molecules in dc MOT ( $1.1 \times 10^5$  molecules [59]) compared to the rf MOT ( $1.5 \times 10^4$  molecules [58]). I should mention that a factor of  $\sim 5$  increase is attributed to the cell modification. As a result, dc MOT traps 20% more molecules than rf MOT shown in Figure 5.17 (a). The cloud volume of dc MOT is a factor of 3.4 smaller than the rf MOT. The temperature of dc MOT is 2 mK, colder than the rf MOT which is 4 mK, as shown in Figure 5.17 (b). Therefore, dc MOT is about 4 times denser and 50 % colder than the rf MOT. Under the same intensity, dc MOT lifetime is  $\sim 50\%$  longer than the rf MOT. DC MOT is also technically simple to realize since it doesn't require magnetic field and polarization modulation. Therefore, we proceed with the dc MOT to trap YO molecules.

### 5.5.2 Detailed DC MOT Characterization

The optimal dc MOT parameters are described in the previous section. Here we show all the optimization we did for the dc dual frequency MOT to maximize the loading and MOT lifetime.

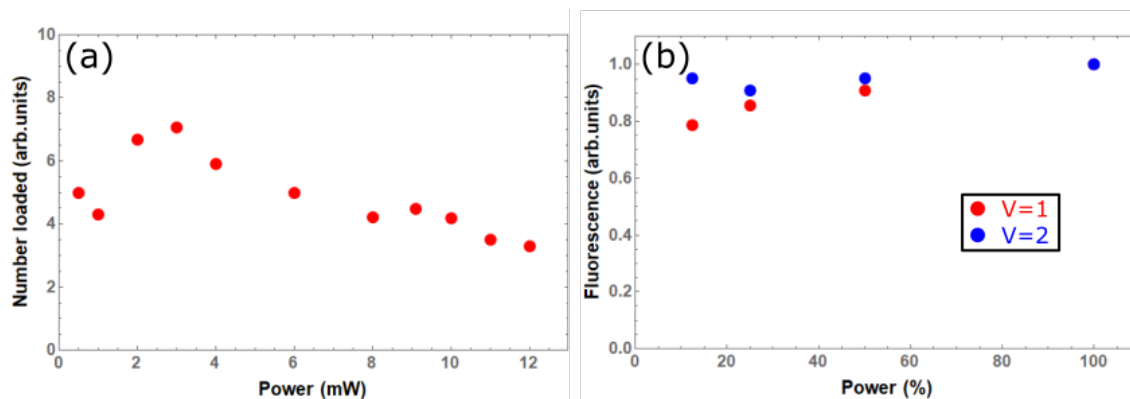


Figure 5.18: (a). MOT loading at different  $v=0$  trapping power. We choose 2 mW for optimal loading. (b). MOT fluorescence at different  $v=1$  and  $v=2$  power. The 100% repumper power of  $v=1$  and  $v=2$  on each hyperfine component is 20 mW. Both  $v=1$  and  $v=2$  repumpers fully saturate the transition.

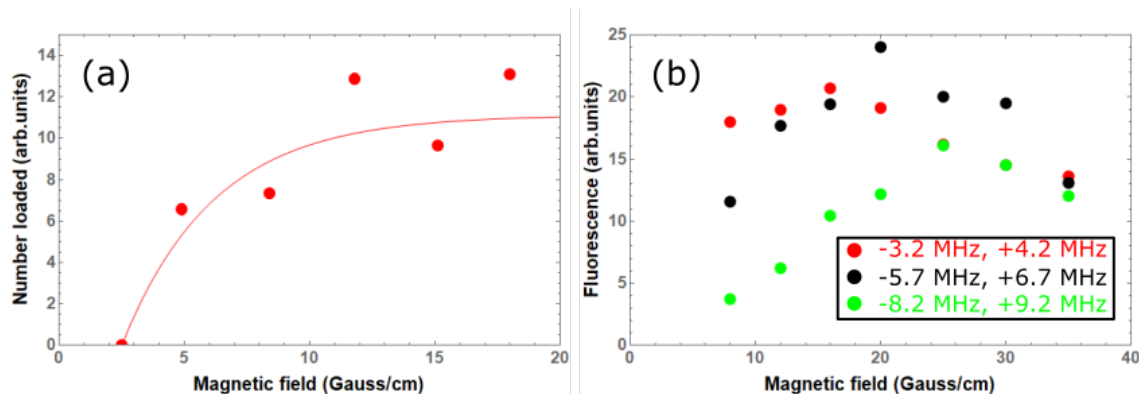


Figure 5.19: (a). MOT loading at different magnetic field gradient. The solid line is a guide for the eye. (b). MOT loading versus various detunings of L3 and L4.

The dc MOT saturates at  $\sim 2$  mW for a beam of diameter of 8.2 mm, as shown in Figure 5.18 (a). The loading becomes worse at high trapping power, potentially resulting from the scattering loss. We can see in Figure 5.18 (b) that both  $v=1$  and  $v=2$  beam fully saturate the transition. We also applied the  $v=3$  repumper but it didn't make any difference, as expected since it takes more than  $10^5$  photon scatterings [88] into  $v=3$  state. We did more lifetime study in the next section.

The MOT loading at various magnetic field gradients and detunings are shown in Figure 5.19. The optimal loading is  $\sim 12$  Gauss/cm while a higher gradient doesn't increase the loading

efficiency any more. Scanning the frequency of the L3 and L4 showed a optimal detuning at  $\sim -3.2$  MHz and  $\sim +4.2$  MHz for 10-40 Gauss/cm. Eventually we chose -5.8 MHz and +2.6 MHz for MOT loading.

### 5.5.3 Collision with Background Gas in DC MOT

In order to figure out what's limiting our MOT lifetime, we first scanned the lifetime at different helium flow rates. The lifetime decreases to 35 ms when the helium flow becomes  $2 \times 10^{-8}$  Torr at 2 sccm, as shown in Figure 5.20 (a). If we measured the MOT lifetime at different scattering rates and then fit the lifetime against scattering rate, as shown in Figure 5.20 (b), we can see there is a constant loss that is limiting the lifetime. This indicates that the MOT lifetime is limited by the collision with background gas. To prevent the helium from reaching the MOT region, a second shutter was installed inside the molecular beam box. This in-vacuum shutter also helps reduce the cell heating effect, which is mentioned in Section 3.2.1. The pressure is reduced to  $3 \times 10^{-9}$  Torr with both shutters open for about 8 ms during the whole experiment and the vacuum lifetime should increase to  $\sim 1$  second. The shutter motor is in direct contact with a large piece of aluminum to dissipate the heat. This is critical to reduce the outgassing and lengthen the shutter lifespan.

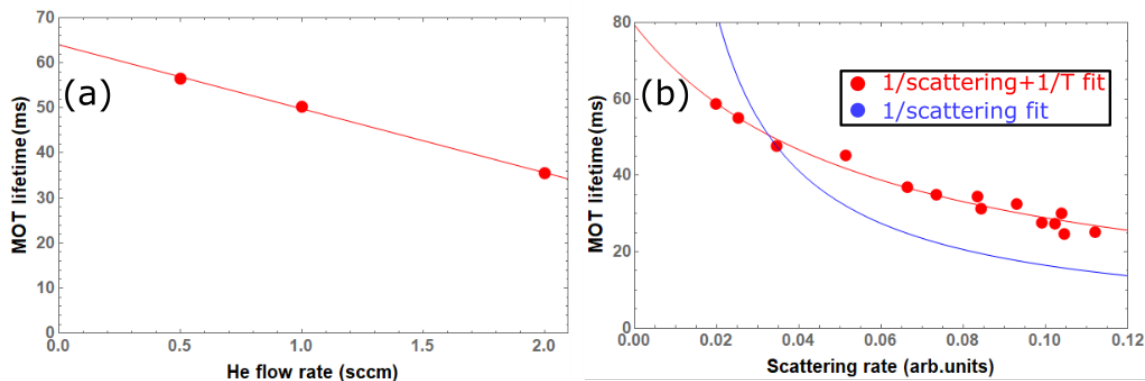


Figure 5.20: MOT lifetime limited by helium. (a). MOT lifetime at different helium flow rate. It's clear that the helium limits the MOT lifetime at high flow rates. (b). MOT lifetime  $t$  versus scattering rate  $R_{sc}$ . The blue line is a fit to the function  $t=a/R_{sc}$  where  $a$  is the fitting parameter. The red line is a fit to the function  $t=a/R_{sc}+1/T$ , where  $T$  represents the lifetime limited by the background gas.

### 5.5.4 Remaining Issues in MOT Beams

When we first made the MOT work, the MOT shape was changing every day. There are several reasons for this instability. First, the MOT beams propagate about three meters before they see the molecules. This long beam path amplifies any pointing fluctuation introduced by the optics. Secondly, the shape of the beams are terrible due to the acousto optical modulator(AOM), tapered amplifier(TA) and Pockel cell. A non TEM00 mode introduces a spatially dependent trapping force which degrades the MOT performance. Thirdly, all components of the MOT beam ( $v=0,1,2$  and hyperfine components) need to match the mode to each other. These problems are solved by coupling the beams into a PM fiber before the beams are directed to the molecules. With a fiber, the length of the beam path is reduced to less than one meter. As a spatial filter, the fiber cleans up the mode and ensures the mode matching of all MOT beams.

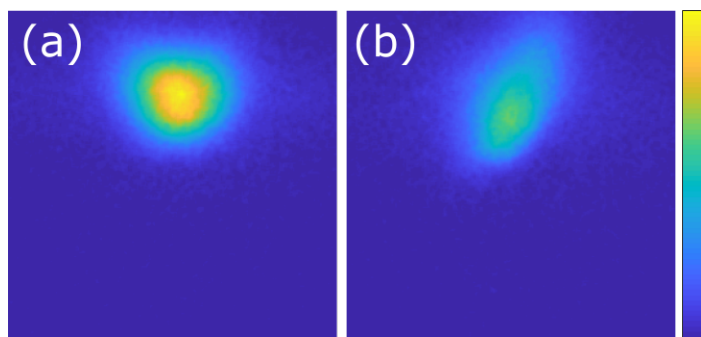


Figure 5.21: (a). MOT with good alignment. (b). MOT with mis-aligned retroreflection( $\sim 0.5^\circ$  off).

In a regular atomic MOT, beam alignment is not very critical. However, our dc MOT relies on a perfect alignment of the counter-propagating beams. Since the MOT beams are circulated through three orthogonal directions, the counter-propagating alignment is optimized by coupling the beam back into the fiber using the retro-reflected mirror. A well optimized and a mis-aligned MOT image is shown in Figure 5.21. The mis-alignment affects both the MOT shape and the number of trapped molecules. One possible reason is the power imbalance in the MOT beams due to the circulation of beams. As previously mentioned in Section 5.2.6, the MOT windows have

considerable loss in transmission. Therefore, the beams are attenuated by  $\sim 12\%$  before retro-reflection. To compensate this power loss, the MOT beams are slightly focused to compensate this attenuation, but it can not balance each MOT direction nicely. A proper way is to decouple these three directions if we have extra laser power and replace all MOT windows with lower loss.

### 5.5.5 Limited MOT Lifetime at High Magnetic Field Gradient

To further compress the molecule cloud, one would reduce the MOT temperature or increase the trapping frequency, as  $T \propto k\sigma^2$  where  $T$ ,  $k$   $\sigma$  are cloud temperature, spring constant and cloud radius. One route is to ramp up the magnetic field after loading to increase the trapping frequency. This is known as compressed MOT (cMOT) [132]. In our experiment, we first load MOT at 12 Gauss/cm for 32 ms, then ramp to a higher magnetic field gradient in 32 ms and eventually measure the cloud size and lifetime.

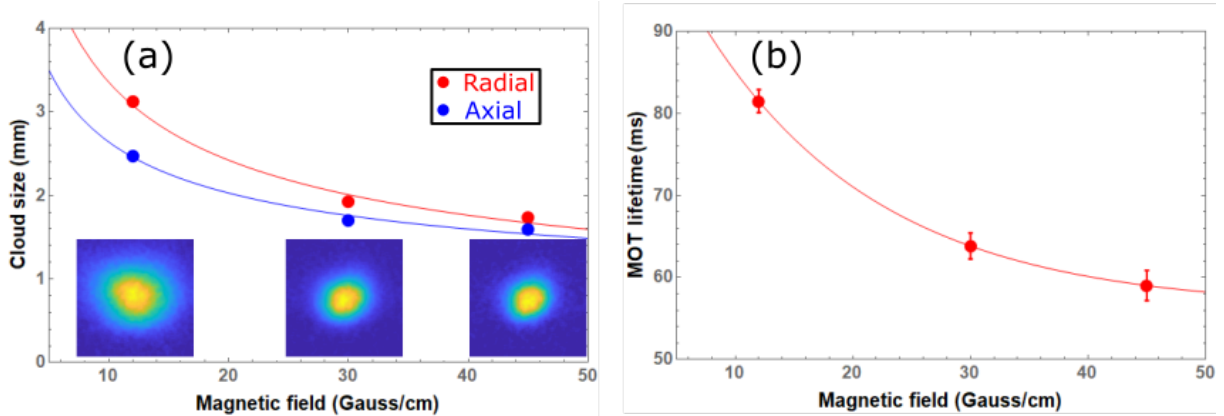


Figure 5.22: Compressed MOT. (a). MOT size  $2\sigma$  at different magnetic field gradient. The solid lines are fits to the function  $\sigma = \frac{1}{\sqrt{dB/dl}}$  where  $dB/dl$  represents the magnetic field gradient. The cloud size shrinks accordingly at large magnetic field gradient. (b). MOT lifetime at different magnetic field gradient. The solid line is a guide for the eye.

We can see from Figure 5.22 (a), the cloud shrinks at higher magnetic field, following  $\sigma \propto (dB/dl)^{-0.5}$  where  $dB/dl$  represents the magnetic field gradient. In addition, we find that the loss gets enhanced at higher field gradient, as shown in Figure 5.22 (b). This loss mechanism is unclear and yet to be discovered. The  $X^2\Sigma^+N = 3(-)$  leaking from  $A'^2\Delta_{3/2}(J' = 3/2(+))$  state has been



repumped by the N=3 repumper. Based on the Frank-Condon factors [88], it takes  $\sim 3000$  photons to pump molecules into  $A'^2\Delta_{3/2}$  state and it has  $\sim 10\%$  chance leaking into  $v=1$  state. With the scattering rate of 0.5 MHz, the calculated lifetime is  $\sim 60$  ms if  $v=1$  N=0,2,3 are not repumped. Therefore, it's very likely that the leakage comes from  $A'^2\Delta_{3/2}(J' = 3/2)$ . Currently, the lifetime of the MOT is long enough for the transfer of the compressed cloud to a conservative trap, in which there would be no resonant light-assisted collisions and the further cooling is feasible.

### 5.5.6 New Trapping Scheme

We propose a new trapping scheme employing  $A^2\Pi_{3/2}$  as the main excited state. The  $A^2\Pi_{3/2}$  state has similar magnetic moment as that used in atomic cooling experiments, as shown in Figure 5.23(b), which will largely improve the capture velocity and trapping force of the MOT [129]. In addition, as recently demonstrated for rubidium atoms [116], applying the blue-detuned MOT, shown in Figure 5.23 (b), to the trapped YO molecules using the excited state with a large Landé g-factor will compress the molecular cloud and increase the spatial density by a few orders of magnitude.

The proposed scheme involves more excited states, which increases the photon scattering rate by more than a factor of two compared with the current one we're using ( $\Gamma/8$ ). In the new scheme, there are 8 manifolds coupled in the excited state ( $n_e = 8$ ) and 20 manifolds involved in the ground state ( $n_g = 20$ ). This results in an effective scattering rate [75, 76]  $\Gamma_{Scatter} = \frac{n_e}{n_g+n_e}\Gamma$  of  $2\Gamma/7$ . According to section 4.3, we expect it to increase the number of slowed molecules by at least an order of magnitude [58] as a result of the higher deceleration rate. Combined with the potential enhancement from the compression, we expect to increase the phase space density by several orders of magnitude.

An extra 597 nm laser is required to implement this scheme. The dye laser can be use if the new fiber laser(Precilaser) generates the N=2 repumper.

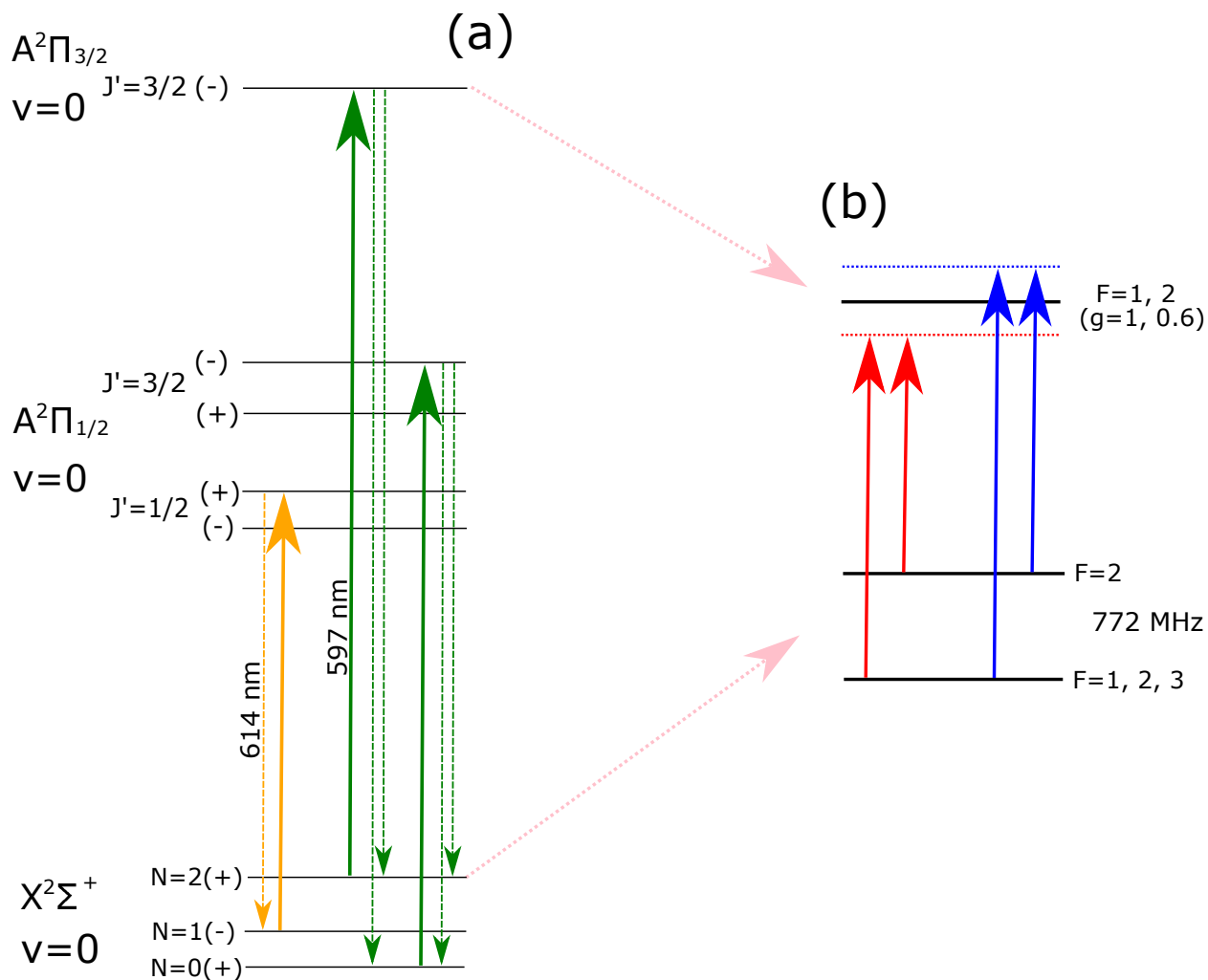


Figure 5.23: (a). Lasers for creating cycling transitions in YO molecules. Orange arrows: the current scheme that optimizes angular momentum closure [54], which only requires a single laser. Green arrows: the proposed scheme that involves the excited  $A^2\Pi_{3/2}$  state. This state has a considerable magnetic dipole moment, which is crucial for improving the MOT trapping force. The solid (dashed) arrows represent the laser-driven transitions (spontaneous emissions). (b). Scheme for capture and compression of molecular cloud. Red: red-detuned MOT [129] for capturing the molecules. Blue: blue-detuned type-II MOT [116] for compression.

## Chapter 6

### Sub-Doppler Cooling and Compressed Trapping of Molecules

Once the molecules are trapped in the MOT, the goal is to further cool and compress the molecular cloud and eventually load them into a conservative trap. In this chapter, we first introduce the theory of sub-Doppler cooling, including gray molasses cooling(GMC) and  $\Lambda$ -enhanced gray molasses cooling. Next, we discuss the performance of YO with these cooling methods. Then, we show a novel compressed trapping scheme tailored for the unique structure of  $^{89}\text{Y}^{16}\text{O}$ . With the combination of these techniques, we produced a laser-cooled molecular sample with the highest phase space density in free space [59].

In this chapter, I reproduce the work published in [59] with modifications.

#### 6.1 Gray Molasses Cooling

Gray molasses is a method of sub-Doppler cooling and is widely used in atomic species with poorly-resolved hyperfine structure. Typically, atoms trapped in MOT can be cooled below the Doppler limit with the quadrupole magnetic field removed. This cooling method is called optical molasses as the trapping force disappears. Then, atoms can be cooled even further by the gray molasses employing the Sisyphus cooling together with a "dark" state, which is not coupled to the light. Compared to traditional optical molasses, gray molasses cooling can achieve a colder temperature, with cold atoms/molecules shielded from interacting with the light.

### 6.1.1 Gray Molasses Cooling Theory

Before the invention of gray molasses cooling, atoms were first cooled with optical molasses after the MOT. By removing the quadruple magnetic field, atoms can be cooled well below the Doppler limit [133], which is an order of magnitude colder compared to the MOT. Typically, there are two configurations for the optical molasses:  $\text{lin}\perp\text{lin}$  and  $\sigma^+\sigma^-$ . In the first case,  $\text{lin}\perp\text{lin}$ , shown in Figure 6.1 (a), there is a spatially varying light shift of the ground-state sublevels ( $M=\pm 1/2$ ), where the polarization cycles from linear to circular to orthogonal linear to opposite circular in the space of half a wavelength.  $M=1/2$  atoms starting at  $z=0$  climb up the potential hill as they approach  $\lambda/4$  point, where the polarization becomes  $\sigma^-$ . At this point, they're very likely to be excited due to the transition selection rule and eventually decay to  $M=-1/2$  state. The same process continues for  $M=-1/2$  until it climbs up to  $\lambda/2$  and get excited by  $\sigma^+$  beam. The energy gets dissipated during each scattering since the atom absorbs less energy compared to the emission, resulting in a low temperature. As for  $\sigma^+\sigma^-$  configuration, there is no spatially varying light shift thus the cooling doesn't rely on the Sisyphus effect. It has been shown that the damping force is introduced by the differential scatterings caused by the imbalance in the population, which results from the time lag between the atomic orientation and the local field [134]. In addition to these configurations, a light field of constant polarization combined with a magnetic field could also produce sub-Doppler cooling [135]. In this case, the polarization is fixed ( $\sigma^+$ ) but the light intensity is oscillating in space because of the interference, as shown in Figure 6.1 (b). For  $J_g=1/2$  to  $J_e=3/2$  transition, ground state  $M=1/2$  is more strongly coupled than  $M=-1/2$ , resulting in a larger light shift. Starting at  $z=0$ , atoms must climb a potential hill as they approach the nodes at  $\lambda/4$ . Under a small transverse magnetic field, atoms may merge into the  $M=-1/2$  state through Larmor precession. As the  $M=-1/2$  state is weakly coupled, atoms gain less energy as they move towards the antinode at  $\lambda/2$ . At this point, where the laser intensity is the strongest, atom can absorb a photon and possibly decay back to  $M=1/2$  state. Each optical pumping results in the absorption of a photon at lower frequency than the emission, taking away the energy.

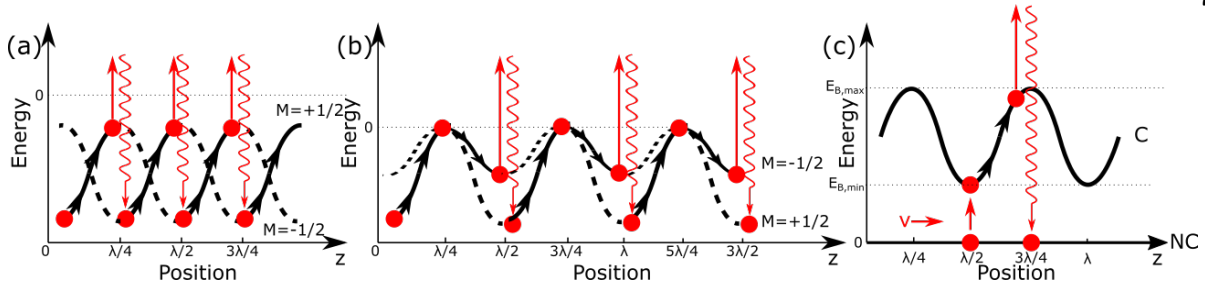


Figure 6.1: Simplified diagram for different sub-Doppler cooling configurations. Excited states are not shown for simplicity. (a). Optical molasses,  $\text{lin}\perp\text{lin}$ . (b). Magnetically induced cooling. (c). Gray molasses,  $\text{lin}\perp\text{lin}$ . C represents coupling state("bright"), NC represents non-coupling state("dark").

Gray molasses cooling(GMC) works on type-II transitions and relies on position-dependent dark states that are formed from the spatial variation of the laser polarization and intensity, as shown in Figure 6.1 (c). Unlike most Doppler cooling techniques, light in the gray molasses must be blue-detuned from its resonant transition. As a result, all "bright" coupling states are always Stark shifted upwards above the "dark" non-coupling state. The "bright" state has a spatially varying light shift due to the polarization gradients while the "dark" state remains unchanged. A molecule in the "dark" state can evolve into the "bright" state through non-adiabatic process at the node where the minimal energy gap is located. Then, the molecule rides up the hill, get excited by the laser and eventually decay back to the "dark" state. Molecules get cooled as they absorb a photon at a lower frequency than the emission. It is worth mentioning that the blue-detuned laser causes Doppler heating, but it is offset by this polarization-gradient cooling. This provides cooling in  $\text{lin}\perp\text{lin}$  case. It has been calculated [128] that for  $F\leftrightarrow F$  and  $F\leftrightarrow F-1$  transition, both  $\text{lin}\perp\text{lin}$  and  $\sigma^+\sigma^-$  configuration of GMC provide cooling in 3-D.

### 6.1.2 Gray Molasses Cooling of YO

In Figure 6.2 (a)-(b), we show the simplified molecular structure and laser configuration relevant to dc MOT and GMC. Once the dc MOT is loaded, we blue detune  $L_1$ , remove the red-detuned component of  $L_2$ , switch off  $L_3$  and the quadrupole magnetic field for gray molasses

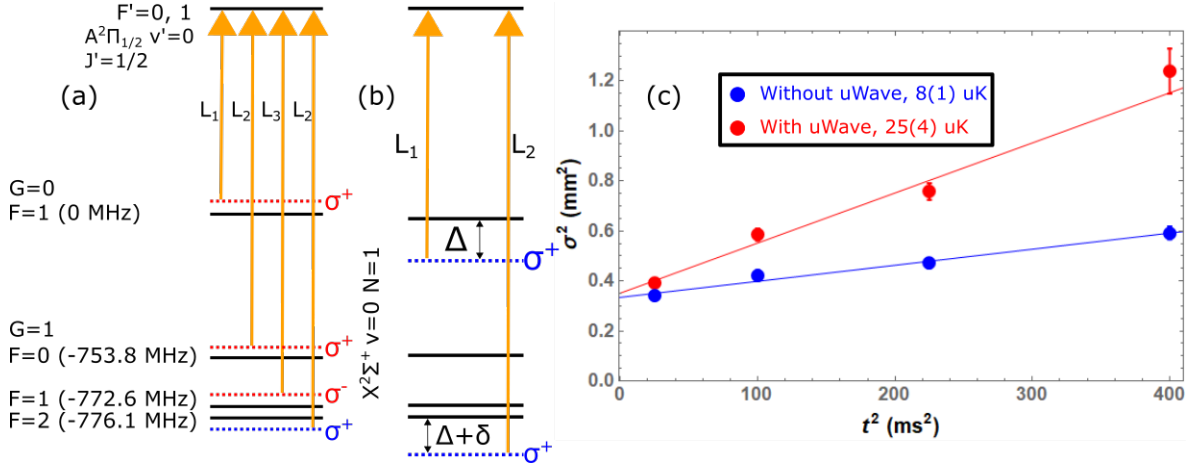


Figure 6.2: (a). Laser setup for DC MOT. (b). Laser setup for GMC. (c). GMC temperature without/out  $N=0 \leftrightarrow N=1$  microwave.

cooling. Unlike other molecules, YO has a large frequency gap (753.8 MHz) between  $G=0$  and  $G=1$ , as shown in Figure 6.2 (a). Therefore,  $L_1(L_2)$  covers  $G=0(G=1)$  individually. The magnetic gradient is switched off in less than 100  $\mu$ s, during which time the laser beams are switched off by AOMs and detuned accordingly by relocking the main laser. All the vibrational and rotational repumpers are left untouched at the initial stage of cooling.

We first tried the GMC cooling with laser intensity  $I=3.1 I_0(I_0=2.7 \text{ mW/cm}^2)$ , single photon detuning  $\Delta/2\pi=10 \text{ MHz}$  and Raman detuning  $\delta/2\pi=-3.5 \text{ MHz}$ . As we can see in Figure 6.2 (c), we achieved a temperature of  $25(4) \mu\text{K}$ , which is two orders of magnitude lower than the temperature inside the MOT (2 mK). During this cooling, microwave remixing between  $N=0 \leftrightarrow N=1$  was kept on to repump the leakage from  $A'^2\Delta_{3/2}(J' = 3/2(-))$  state. However, any field addressing the ground state, such as magnetic or electric field, is detrimental since the cooling relies on the light shift of the ground state. Therefore, with microwave switched off, the temperature was significantly reduced to  $8(1) \mu\text{K}$ . By doing so, we lost 15% of molecules as  $N=0$  and  $N=2$  states are not repumped back to the main cycling transition. This loss is not significant since it requires  $\sim 3000$  photon scatterings to  $A'^2\Delta_{3/2}(J' = 3/2(-))$  state and GMC doesn't scatter many photons as long as the molecules are cold. The GMC temperature reduces with single photon detuning  $\Delta$  and intensity  $I$  as the

momentum diffusion is reduced [134].

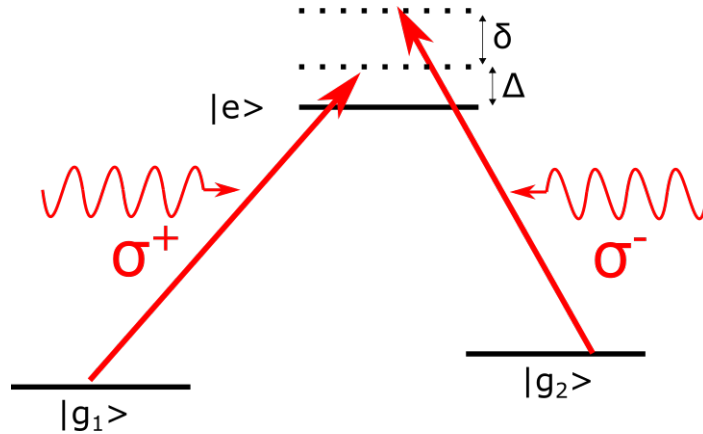


Figure 6.3: Three level system showing velocity selective coherent population trapping(VSCPT).

## 6.2 $\Lambda$ -Enhanced Gray Molasses Cooling

$\Lambda$ -Enhanced gray molasses combines the gray molasses with velocity selective coherent population trapping(VSCPT) [136]. It introduces a dark state which is more stable compared to the "dark" state in gray molasses cooling. Therefore, the cold molecules can not scatter photons and eventually a colder temperature can be achieved.

### 6.2.1 $\Lambda$ -Enhanced Gray Molasses Cooling Theory

The theory can be explained using a three level system, as shown in Figure 6.3 (a). With two circularly polarized, counter propagating beams of specific frequencies, a coherent dark state is formed for molecules with specific velocity( $v \propto \delta/M$ ), therefore, the molecules at velocity  $v$  can not scatter any photons. This is because, in the molecular frame, the two counter propagating beams form a Raman resonance, creating a superposition of ground state  $g_1$  and  $g_2$  with transition amplitudes destructively interfere. Therefore, the cooling "center" is determined by the Raman detuning  $\delta$ . If  $\delta$  is zero, then the molecules with zero velocities will be trapped by the VSCPT effect. However, VSCPT is not very efficient by itself due to its stochastic nature. Combined with

the GMC where the energy is effectively dissipated,  $\Lambda$ -enhanced GMC can reach extremely low temperature with very limited photon scatterings. This technique was first demonstrated in alkali atoms [137], creating a dense lithium atom sample at  $\sim 60\mu\text{K}$ .

### 6.2.2 $\Lambda$ -Enhanced Gray Molasses Cooling of YO

In our YO setup, two lasers are applied to address  $G=0$  and  $G=1$  states separately, due to their large frequency gap. This significantly reduces the parameter space. To explore the  $\Lambda$ -enhanced feature, we set  $I=3.2I_0$ , leave  $L_1$  fixed at  $\Delta/2\pi=40$  MHz and vary the frequency of  $L_2$ . As we can see in Figure 6.4 (a), a low temperature is achieved if the Raman detuning  $\delta=0$ , where a coherent dark state is formed between  $G=0$   $F=1$  and  $G=1$   $F=2$ . A similar feature is also observed at  $\delta/2\pi=-3.5$  MHz where a coherent dark state is formed between  $G=0$   $F=1$  and  $G=1$   $F=1$ . Unlike typical  $\Lambda$ -enhanced feature, we do not see a lower temperature at resonance, but instead, there are extensive heating peaks around the Raman resonance.

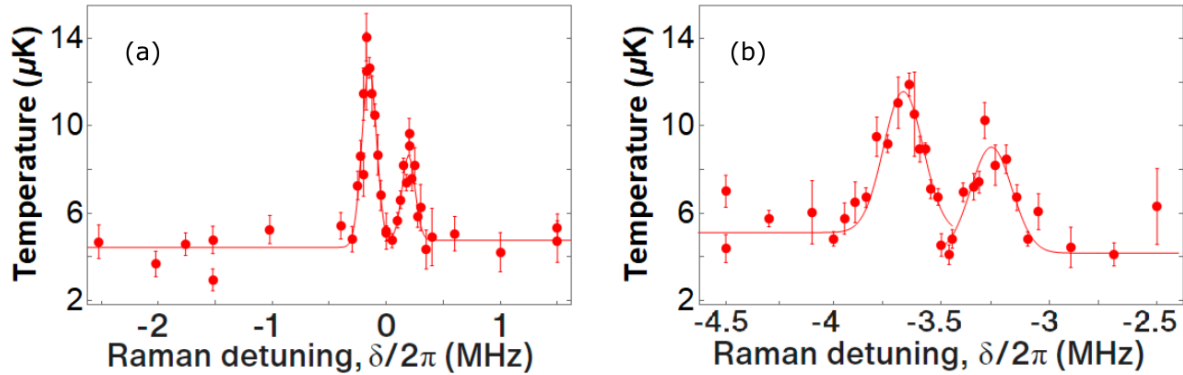


Figure 6.4: Temperature vs Raman detuning around different Raman resonance, with  $I=3.2I_0$  and single-photon detuning  $\Delta/2\pi=40$  MHz. (a). Temperature vs Raman detuning around  $G=0$   $F=1$  and  $G=1$   $F=1$  Raman resonance. (b). Temperature vs Raman detuning around  $G=0$   $F=1$  and  $G=1$   $F=2$  Raman resonance. We do not see a lower temperature at resonance, but there are extensive heating peaks around the Raman resonance.

To understand the performance of GMC around a Raman resonance, we next investigate the cooling on each hyperfine state by putting  $L_1$  or  $L_2$  on resonance. We keep  $I=3.2I_0$ , leave  $L_1$  fixed



at  $\Delta/2\pi=40$  MHz and vary the frequency of  $L_2$  in a much larger range, as shown in Figure 6.5. For  $\delta/2\pi=-43.5$  MHz, the remaining component of  $L_2$  is on resonance with  $G=1, F=1$ . Thus, cooling (to  $9 \mu\text{K}$ ) arises purely from the  $G=0, F=1$  manifold. Similarly, if we set  $L_1$  on resonance with  $G=0$  while having  $L_2$  blue detuned from  $G=1$ , the cooling temperature reaches as low as  $15 \mu\text{K}$ . We thus conclude that both  $G=0$  and  $G=1$  states are responsible for cooling, and their combination leads to an efficient sub-Doppler cooling of YO to the lowest temperature while being robust against the Raman detuning  $\delta$  in a wide range. This is very different compared to an atomic system, where one laser provides cooling while the other is mostly responsible for repumping. Therefore, in YO setup,  $L_1$  and  $L_2$  beams share the same intensity in our setup.

As we can see in Figure 6.4, when  $\delta$  is tuned slightly away from zero, we observe striking rises of temperature, followed with quick decreases back down to  $4 \mu\text{K}$  when  $|\delta|$  becomes sufficiently

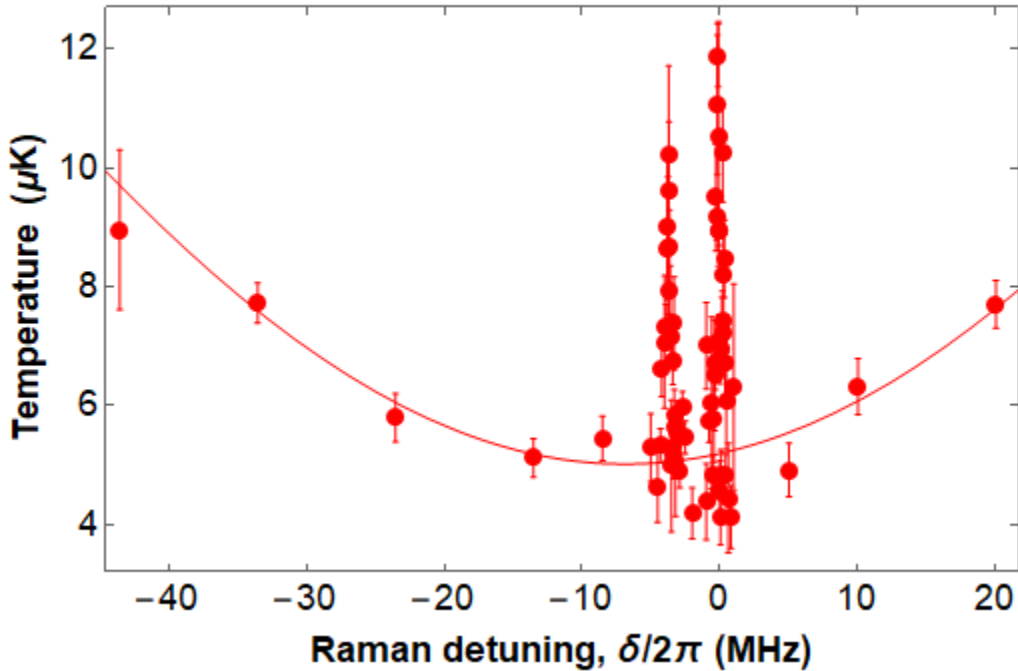


Figure 6.5: Temperature vs Raman detuning  $\delta$ , with  $I=3.2I_0$  and single-photon detuning  $\Delta=8.3\Gamma(2\pi\times 40$  MHz). The solid line is a guide for the eye.

large of a few hundred kHz. The two resonancelike features are symmetrically located around  $\delta=0$ . This feature has been observed previously in other molecules [61] without explanations.

To understand the heating peaks around the Raman resonance, we explore the cooling performance with various parameters, as shown in Figure 6.6. As we can see in Figure 6.6 (a), the observed peak width and splitting between the two temperature peaks increase with the laser intensity. As for the single-photon detuning  $\Delta$ , shown in Figure 6.6 (b), the peak width and splitting decreases with  $\Delta$ . Our understanding for this effect is the following. Gray molasses cooling depends on transient dark states [128, 138] and generally, a less stable dark state causes more momentum diffusion and leads to a higher temperature. Near the Raman resonance condition ( $\delta = 0, -3.5$  MHz), dark states formed in both  $G=0 F=1$  and  $G=1 F=1(2)$  can be destabilized by their cross-coupling. It leads to enhanced photon scattering and deteriorated cooling over a range on the order of the two-photon Rabi frequency,  $\Omega_R \propto \Omega_1\Omega_2/\Delta$ , consistent with our observation. This result is different from the  $\delta=0$  situation, where a new stable dark state is formed with the superposition of Zeeman sublevels from different hyperfine states [61, 62], resulting in a  $\Lambda$ -type GMC.

In addition to the peak width and separation, we can see the lowest temperature changes with the laser intensity and single-photon frequency  $\Delta$ . The temperature depends on the molasses beam intensity and single-photon detuning  $\Delta$  in a way consistent with theory [128]. As shown in Figure 6.7 (b) and (c) for  $\delta=0$ , the temperature increases linearly with the intensity and decreases with the detuning before settling down to a constant. The momentum diffusion coefficient  $D_p$  increases(decreases) with intensity(detuning), while the damping coefficient  $\alpha$  is both intensity and detuning insensitive [128]. The temperature is determined by  $k_B T = D_p / \alpha$ , where  $k_B$  is the Boltzmann constant. The fittings in Figure 6.7 (b) and (c) are consistent with this model. This behaviour is similar to the sub-Doppler cooling with type-I transitions [134], where  $T \propto |\Omega|^2 / \Delta$ .  $\Omega$  is the Rabi frequency, which is proportional to  $\sqrt{I}$ .

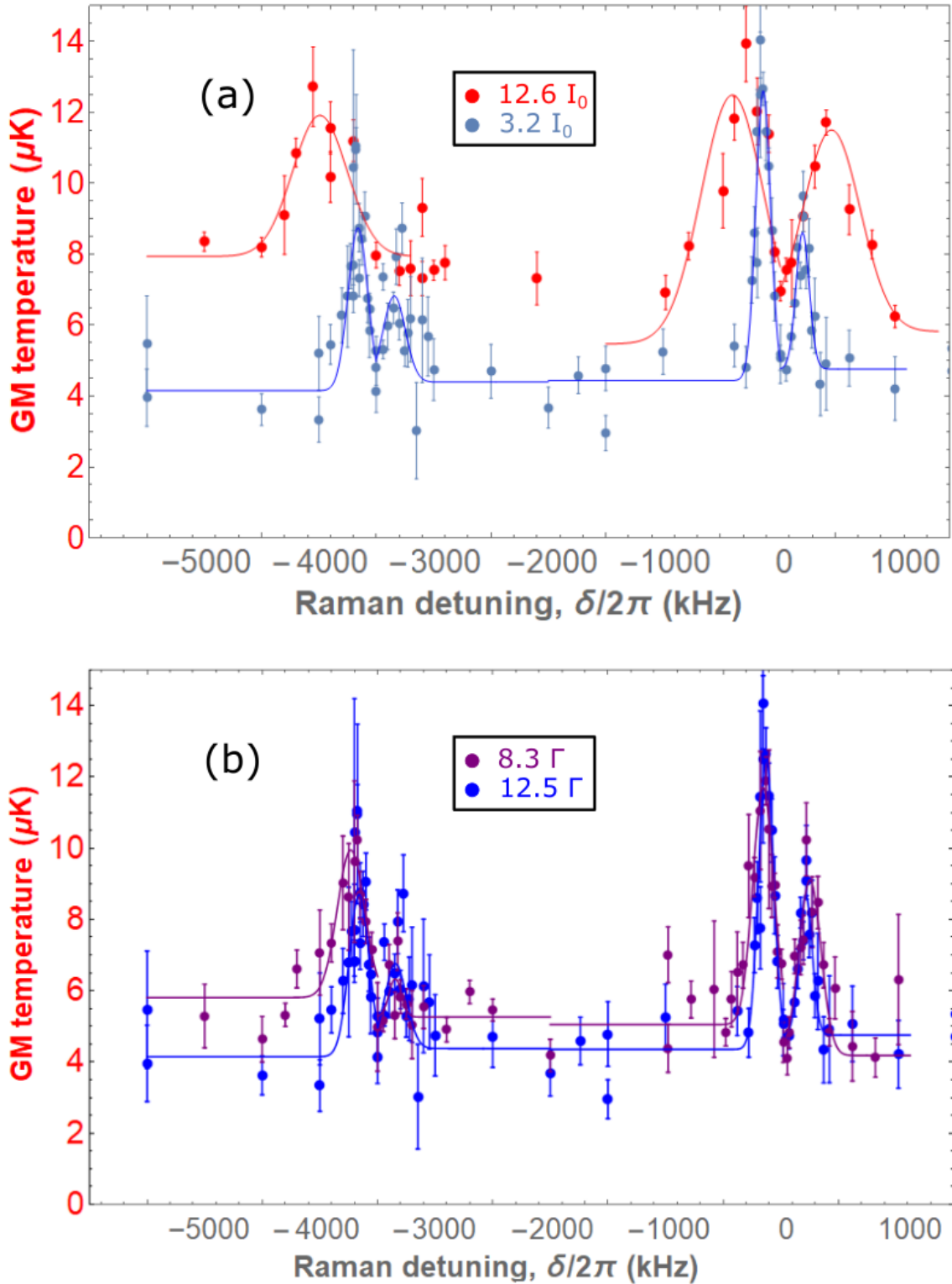


Figure 6.6: Temperature vs Raman detuning  $\delta$ . (a).  $\Delta=12.5\Gamma$  with different intensity  $I$ . (b).  $I=3.2I_0$  with different single-photon detuning  $\Delta$ . The peak width and separation increases(decreases) with  $I(\Delta)$ . The lowest temperature also depends on the intensity and single-photon detuning  $\Delta$ , consistent with theory [128].

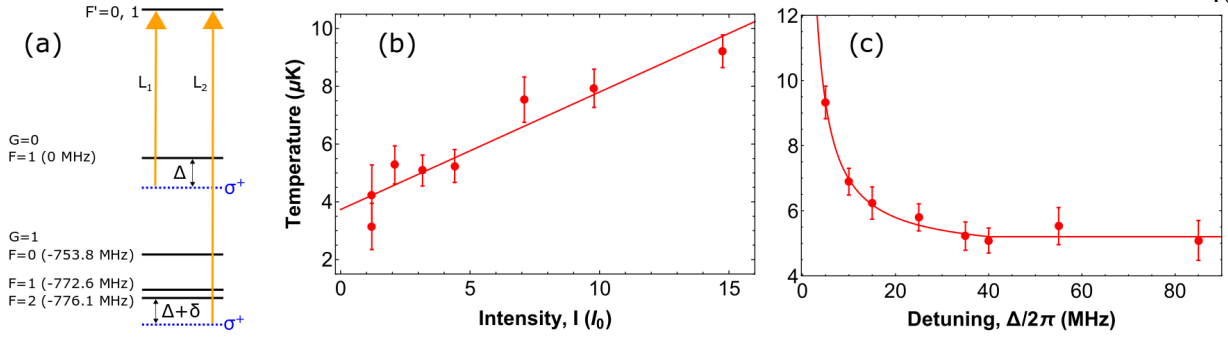


Figure 6.7: Characterization of GMC. (a). Configuration of laser detunings. (b). Temperature versus intensity  $I$  with single-photon detuning  $\Delta=8.3\Gamma$  and Raman detuning  $\delta=0$  between the  $G=0$   $F=1$  and the  $G=1$   $F=2$  manifolds. The solid line is a linear fit. (c). Temperature versus  $\Delta$  with  $I=3.2I_0$  and  $\delta=0$ . The solid line is a fit to the function  $T_{avr}=1/\Delta+T_0$ , where  $T_0$  represents a background temperature. The error bars in the plots correspond to  $1\sigma$  statistical uncertainty, and the fittings are consistent with the theoretical predictions in [128].

With  $\delta=0$ ,  $\Delta/2\pi=40$  MHz and  $I=1.2I_0$ , we achieve a YO sample at  $4 \mu\text{K}$ , which represents the coldest laser cooled molecules in free space. It is worth mentioning that, for an intensity smaller than the minimum value ( $I=1.2I_0$ ) shown in Figure 6.7 (b), the molasses becomes too weak to hold molecules against gravity, leaving an unexplored territory.

## 6.3 Compressed Trapping of YO

### 6.3.1 Gray Molasses Cooling with Magnetic Field

It has been shown previously in Figure 6.2 (c) that microwave coupling between the  $N=0$  and the  $N=1$  state increases the lowest temperature of GMC. The temperature increases as long as the ground state is perturbed by an external field. The ground state can be shifted by Zeeman effect as well. Bias magnetic field also remixes the bright and dark state, reducing the cooling efficiency. Therefore, Earth's field was roughly cancelled when the chamber was open by the cancellation coils shown in Figure 6.8. These Helmholtz coils provide a small region of homogeneous field along NS(1.16 gauss/A), EW(-1.14 gauss/A) and Z direction(-14.2 gauss/A). Figure 6.9 shows the cloud temperature versus different bias magnetic field. These scans are repeated several times until the lowest temperature is achieved.

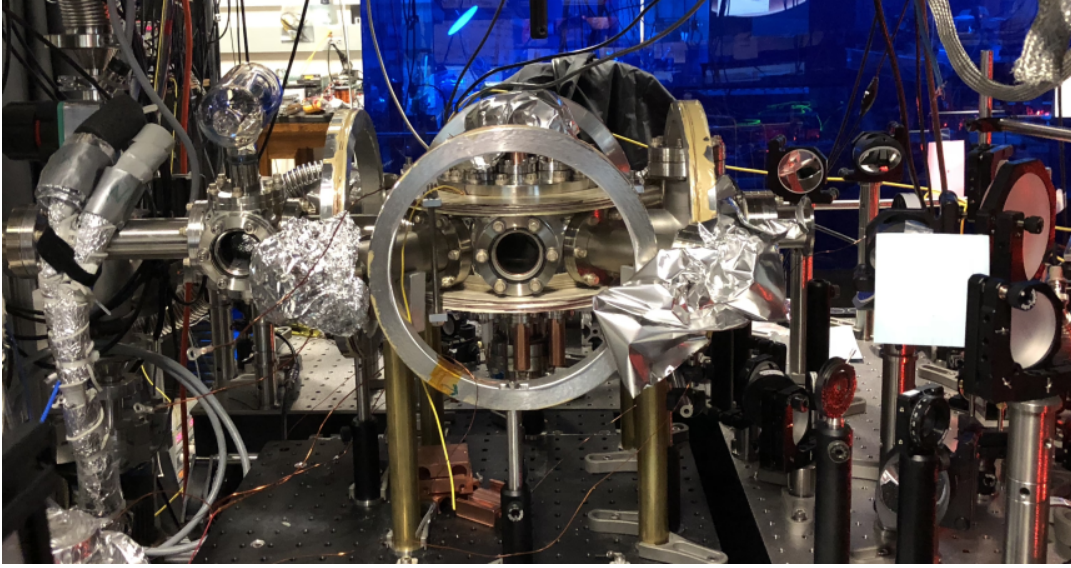


Figure 6.8: Cancellation coil pairs. They are made with magnetic wire using the winding tools designed by the machine shop. Aluminum rings are machined by the shop to hold coils in place. Three pairs of coils cancel three directions independently.

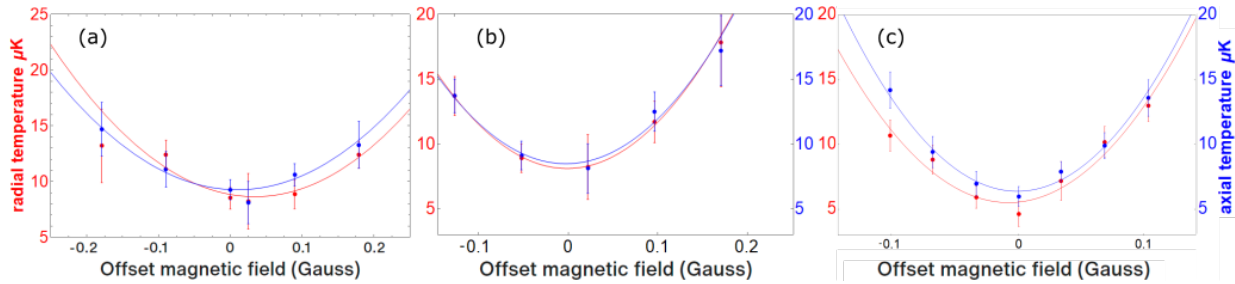


Figure 6.9: Cancellation coil scans. (a). Z coil. (b). North/South coil. (c). East/West Coil.

### 6.3.2 Robust Cooling with Magnetic Field

Considering the negligibly small Lande  $g$  factor for  $G=0$ , it's interesting to explore how well gray molasses performs in the presence of  $B$ . We apply a magnetic field along the axial direction with a pair of cancellation coils and measure the temperatures both along and perpendicular to  $B$  with  $\delta=0$ . Typically, the temperature would continue to rise with a stray magnetic field. This turns out not to be the case for YO. As we scan over a large range of bias field, we see the GMC is surprisingly robust over a large range of magnetic field strength, along with a few remarkable

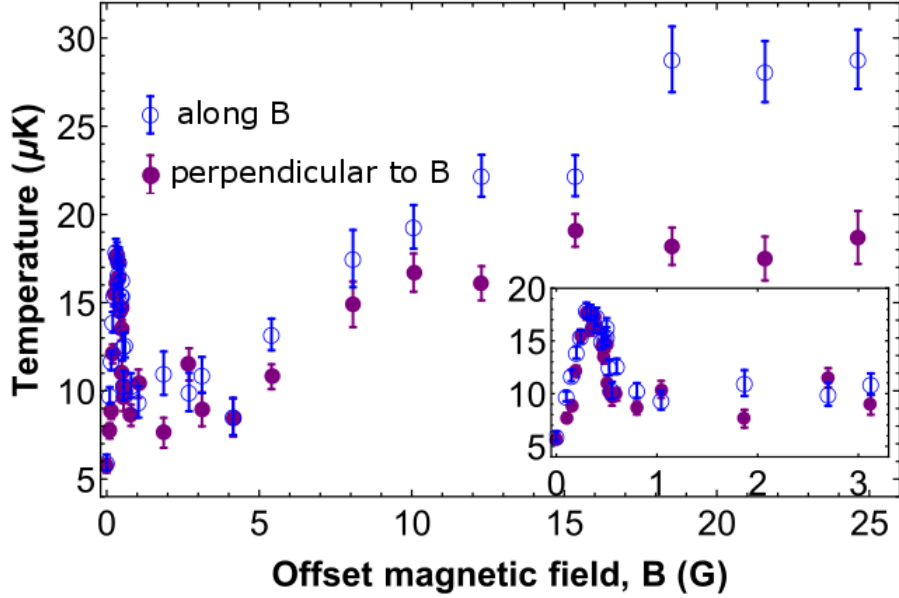


Figure 6.10: Temperature under a uniform B applied along  $z$ , with  $I=3.2 I_0$ ,  $\Delta=8.3\Gamma$  and  $\delta=0$ . The blue open circles (purple filled points) represent the temperature measured along (transverse to) B. The inset shows the temperature from 0 to 3 gauss.

features.

First, the temperature appears to have a pronounced peak near 0.3 gauss. This resonancelike feature is attributed to the Zeeman shifts of the  $G=1$   $F=2$  sublevels destabilizing the dark state formed both in its own manifold through Larmor precession and in the  $G=0$   $F=1$  manifold through Raman coupling. The temperature dependence on magnetic field then becomes flat between 0.6 and 4 gauss, regardless of whether  $L_2$  is tuned on resonance with  $G=1$   $F=2$  ( $\delta/2\pi=-43.5$  MHz) or remains on Raman resonance with  $L_1$  ( $\delta=0$ ). This observation reveals that, within this range, GMC arises mostly from  $G=0$   $F=1$ , where relatively a stable dark state is formed due to its small Lande  $g$  factor.

At approximately 4 gauss, the temperature starts to rise with B, indicating the dark state in  $G=0$   $F=1$  becomes unstable. The temperature measured in the direction perpendicular to B rises slower than that along B and reaches a plateau after approximately 10 gauss. This effect is attributed to the magnetically induced Sisyphus cooling [139, 140, 141, 142, 143], introduced in

Section **6.1.1**, after the original GMC becomes less effective. The laser field pumps YO into a dark state, which is remixed with a bright state via Larmor precession. This process damps the molecular motion in a Sisyphus fashion [142]. In the direction transverse to B, the spatially varying dark and bright state mixing is much stronger than that along B. Therefore the temperature is lower in the transverse direction. The magnetically induced Sisyphus cooling works at approximately 25 gauss for YO, which is substantially larger than the field ( $\sim 1$  gauss) applied to any other atoms or molecules [139, 140, 141, 142, 143]. Such an exceptional magnetic insensitivity must be attributed to the small Lande  $g$  factor of  $G=0$   $F=1$  state.

### 6.3.3 A Novel Compression Method

Such exceptionally robust GMC against the magnetic field brings an intriguing capability. In the presence of the quadrupole magnetic field applied for the MOT, molecules can still be cooled via GMC to a temperature much lower than that for the MOT. Thus, with the quadrupole field turned on continuously, we can alternate the laser beams between MOT and GMC parameters so as to apply the strong trapping force of the MOT to the ultralow-temperature molecular sample prepared by GMC. This scheme works effectively, as the GMC process is fast relative to MOT heating, such that the compression from the MOT dominates over the expansion during the GMC.

We first measure the cooling (heating) rate of GMC (MOT) by recording the temperature for different GMC (MOT) pulse durations. The GMC cooling rate increases with the laser intensity and is not sensitive to the single-photon detuning  $\Delta$  between  $1\Gamma$  and  $6.2\Gamma$ . As shown in Figure 6.11 (a), with full laser power  $30I_0$  and detuning  $3.1\Gamma$ , molecules are cooled from 2 mK to 100  $\mu$ K with a  $1/e$  time constant  $\tau \sim 94 \mu$ s. As for the MOT heating process, shown in Figure 6.11 (b), takes approximately 1 ms to 1 mK.

To explore the MOT compression, we first ramp the magnetic field gradient of the dc MOT from 12 to 47 G/cm in 5 ms and hold at this value for another 5 ms for initial compression [132, 144]. This is known as compressed MOT (cMOT) and its performance has been described previously in Section **5.5.5**. The MOT stabilizes with a diameter of 1.4 mm (2.4 mm) along the axial (radial)

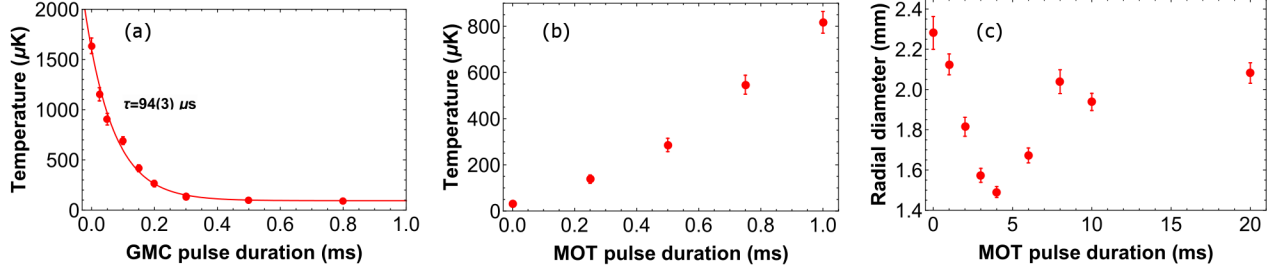


Figure 6.11: Compression of the molecular cloud by combining the GMC with the dual-frequency dc MOT at a B gradient of 47 G/cm. (a) Temperature versus the duration of the GMC pulse, with  $I=30I_0$ ,  $\Delta=3.1\Gamma$ , and  $\delta=0$ . The solid line is an exponential fit with  $1/e$  time constant as  $94(3)\mu\text{s}$ . (b),(c) Temperature and *in situ* diameter of the molecular cloud versus the duration of a single MOT pulse, which is applied after the 2 ms GMC pulse.

direction. We then apply a 2 ms GMC pulse to cool the molecules followed by another MOT pulse with a varying duration for compression. The cloud size is measured right after the MOT pulse, as shown in Figure 6.11 (c). The cloud size shrinks until approximately 4 ms and is significantly smaller than the equilibrium MOT size. This compression process is dynamical, and the cloud expands to eventually reach the original MOT size.

For our optimized compression sequence, we repeat the GMC-MOT cycle 3 times in 10 ms after the initial 5 ms MOT hold pulse, as shown in Appendix D. We do not observe considerable molecule loss during the compression except those optically pumped into the unaddressed dark states(50%). After the compression, the cloud has a diameter of 0.69 mm (0.93 mm) along the axial (radial) direction. The corresponding volume is approximately 10 times smaller than that before the compression, with approximately  $5 \times 10^4$  molecules remaining and a peak spatial density of  $5.4 \times 10^7 \text{ cm}^{-3}$ . The molecules are then cooled to 4  $\mu\text{K}$  with a final 8 ms GMC pulse, creating a molecular sample with a peak phase space density of  $3.3 \times 10^{-8}$ . The 4  $\mu\text{K}$  temperature is about 8 times the recoil limit.

Even though  $G=0$  and  $G=1$  both contribute to cooling, we should still explore the hyperfine ratio since the  $G=0$  state is more robust against the variations of experiment conditions.



## Chapter 7

### Optical Trapping of Molecules

After the realization of the ultracold molecule sample in freespace, it is important to transfer molecules into a conservative trap for interesting applications, ranging from ultracold chemistry to quantum simulation. Typically, a cold and dense sample in the conservative trap is desired. In recent years, many indirectly cooled molecules have been loaded in optical traps [23, 24, 25, 26, 40, 41, 42, 145]. For directly cooled molecules, we have both Stark-decelerated molecules and laser cooled molecules loaded in various conservative traps [63, 64, 65, 61, 66, 67, 68, 146].

Conservative traps for neutral atoms have been studied extensively over the past few decades. Magnetic and optical traps are the two main setups used in the cold atom community. Magnetic traps have high trap depths on the order of 100 mK, while it could only trap molecules on low field seeking state. This is not ideal for molecules with a complex structure. However, optical trapping could be independent of internal states if the trapping laser is far detuned. This is critical for cooling inside the trap since the cooling strongly depends on the coherent dark states that could be destroyed by the differential ac Stark shifts, as described in Chapter 6. In this chapter, we discuss how the YO molecules are cooled and loaded into optical dipole trap(ODT) and optical lattice.

#### 7.1 Optical Dipole Trap(ODT) Theory

Optical dipole traps are formed when an atom or molecule interacts with a strong, far detuned, and focused laser beam. Here we follow the derivation of [147] to calculate the basic equations by considering the atom as a simple oscillator to the classical radiation field.

### 7.1.1 Molecule Interacts with Laser

When an atom/molecule is interacting with a laser beam, the electric field  $\mathbf{E}$  induces an atomic dipole moment  $\mathbf{p}$  oscillating at the driving frequency  $\omega$ . The complex polarizability  $\alpha$  is defined as  $\tilde{p} = \alpha(\omega)\tilde{E}$ . The interaction potential  $U_{dip}$  is [147]

$$U_{dip} = -\frac{1}{2}\langle pE \rangle = -\frac{1}{2\varepsilon_0 c} Re(\alpha)I$$

where  $I = 2\varepsilon_0 c |\tilde{E}|^2$  and a  $\frac{1}{2}$  factor is introduced as the dipole moment is induced. Thus, the dipole force results from the gradient of the interaction potential  $F_{dip}(r) = -\nabla U_{dip}(\mathbf{r}) = \frac{1}{2\varepsilon_0 c} Re(\alpha)\nabla I(r)$ . We can see that there is a net force pointing towards the intensity maxima if  $Re(\alpha)$  is positive. In order to calculate the polarizability  $\alpha(\omega)$ , we first consider the Lorentz's oscillator model. In this picture, an electron is considered to be bound elastically to the core where the oscillation eigenfrequency  $\omega_0$  corresponds to the optical transition frequency. The radiative energy loss introduces damping to the system. We can write down the equation of motion  $\ddot{x} + \Gamma_\omega \dot{x} + \omega_0^2 x = -\frac{eE(t)}{m_e}$  for the electron, where  $\Gamma_\omega = \frac{e^2 \omega^2}{6\pi\varepsilon_0 m_e c^3}$  is the classical damping rate. Integrate the equation, we could get

$$\alpha = \frac{e^2}{m_e} \frac{1}{\omega_0^2 - \omega^2 - i\omega\Gamma_\omega} = 6\pi\varepsilon_0 c^3 \frac{\Gamma/\omega_0^2}{\omega_0^2 - \omega^2 - i(\omega^3/\omega_0^2)\Gamma}$$

where we introduce the on-resonance damping rate  $\Gamma = \Gamma_{\omega_0} = (\omega_0/\omega)^2 \Gamma_\omega$ . This gives a dipole potential in the case of large detunings and negligible saturation situation:

$$U_{dip}(\mathbf{r}) = -\frac{3\pi c^2}{2\omega_0^3} \left( \frac{\Gamma}{\omega_0 - \omega} + \frac{\Gamma}{\omega_0 + \omega} \right) I(\mathbf{r})$$

Thus for red(blue) detuning,  $\omega - \omega_0 < (>)0$ , dipole force points toward highest(lowest) intensity. In the case of dipole trapping, the saturation effects can be neglected. The damping rate  $\Gamma$  can be determined by the dipole matrix element between ground and excited state,

$$\Gamma = \frac{\omega_0^3}{3\pi\varepsilon_0 \hbar c^3} |\langle e|\mu|g \rangle|^2$$

For a multilevel system, the damping rate becomes a sum over all relevant states:

$$\Gamma = \frac{\omega_0^3}{3\pi\varepsilon_0 \hbar c^3} \sum_i \sum_j |\langle e_i|\mu_{ij}|g_j \rangle|^2$$

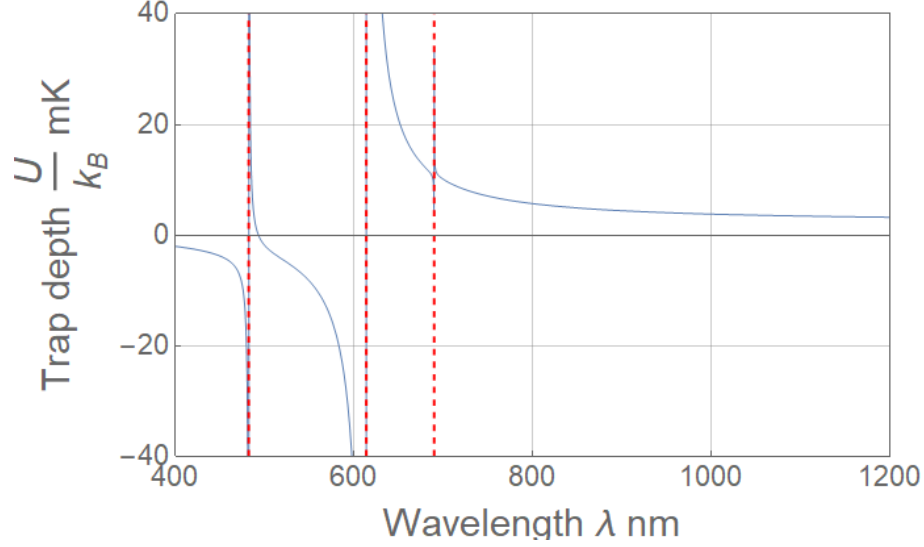


Figure 7.1: YO trap depth as a function of wavelength. Here I assume a 100 watt trapping beam with a beam waist of 20 micron.

Considering all nearby electronic states  $A^2\Pi$ ,  $B^2\Sigma^+$ ,  $A'^2\Delta$ , we can calculate the trap depth of YO at different trapping wavelength, as shown in Figure 7.1. The dashed lines represent the resonant transition wavelength. We tried a near resonant optical trap(NROT) at 689 nm and a far-off-resonance optical dipole trap (FORT) at 1064 nm, which will be detailed in the following sections.

### 7.1.2 Gaussian Beam Profile

Single beam ODT is a focused-beam trap as shown in Figure 7.2 (a). The intensity distribution follows:

$$I(r, z) = I_o \left( \frac{w_o}{w(z)} \right)^2 \exp \left( \frac{-2r^2}{w^2(z)} \right)$$

In the case of low saturation, atoms/molecules spend most of the time in the ground state and we can calculate the light-shifted ground state as the trapping potential of atoms, illustrated in Figure 7.2 (b)(c). When atoms/molecules are cold enough compared to the trap depth, they occupy the bottom of the trap. Therefore, the trap properties can be calculated under harmonic approximation:

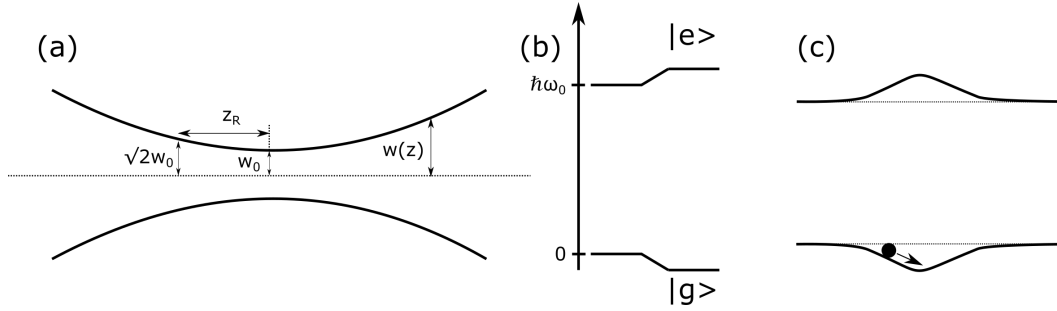


Figure 7.2: (a). Gaussian beam profile. A focused gaussian beam is used to provide both radial and axial trapping. (b). Energy shifts from the trapping laser. A red-detuned trapping beam shifts the ground state energy lower. (c). Spatially varying potential due to Gaussian beam profile. Atoms/molecules are trapped at the intensity maximum where the trap is the deepest. (b) and (c) are reproduced from Ref. [147].

$$\omega_r = \sqrt{\frac{4U_{dip}}{mw_0^2}} \quad \text{Radial Frequency}$$

$$\omega_z = \sqrt{\frac{2U_{dip}}{mz_r^2}} \quad \text{Axial Frequency}$$

$$n_0 = N \left( \frac{m}{2\pi k_B T} \right)^{3/2} \omega_r^2 \omega_z \quad \text{Peak Density}$$

If the atoms/molecules are hot or trap is shallow, the harmonic approximation breaks down. Typically, a focused-beam ODT is aligned perpendicular to the direction of gravity. In this case, the strong radial force  $\sim U_{dip}/w_0$  prevent the molecule from falling under gravity. Normally, the radial trapping frequency is about a hundred times larger than the axial trapping frequency due to the focused beam geometry. If a shallow trap is tilted, atoms/molecules can leave the trap by falling along the axial direction, as shown in Figure 7.3. The linearly polarized light is usually the right choice for a dipole trap, as the magnetic sub-levels of certain hyperfine manifold are shifted by the same amount.

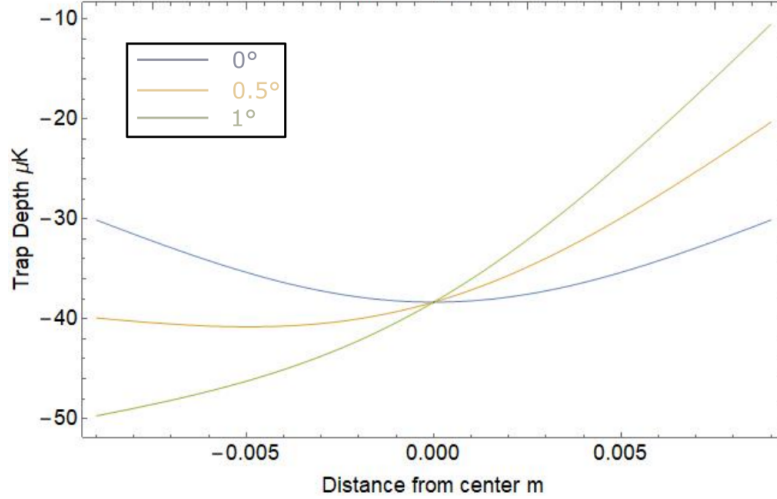


Figure 7.3: Here I plot the trap depth along the axial direction. Atoms/molecules can leave the shallow trap if there is a tilt. For a shallow trap, a trap alignment becomes critical.

## 7.2 689 nm ODT

Based on the polarizability derived in the last section, we found that the trap depth  $U_{dip} = \frac{3\pi c^2}{2\omega_0^3} \frac{\Gamma}{\Delta} I(\mathbf{r})$  scales as  $\frac{1}{\Delta}$  while the scattering rate  $\Gamma_{sc} = \frac{3\pi c^2}{2\hbar\omega_0^3} \left(\frac{\Gamma}{\Delta}\right)^2 I(\mathbf{r})$  scales as  $\frac{1}{\Delta^2}$ . A simple relation exists between the trap depth and scattering rate  $\Gamma_{sc} = \frac{\Gamma}{\hbar\Delta} U_{dip}$ . With a narrow  $A'^2\Delta$  state, we could create a near-resonant optical trap(NROT) with low power.

### 7.2.1 Experiment Setup

We obtain a 100 mW of 689 nm beam from a tapered amplifier(EYP-TPA-0690-00250-2003-CMT02-0000) and then focus to a beam waist of 50  $\mu\text{m}$ . According to the calculation, this produces a trap depth of 15  $\mu\text{K}$ , with scattering rate of 1 Hz. The ODT beam is aligned to the molecular cloud by depleting molecules into  $N=0/2$  dark states, creating a hole at the center of the molecule cloud. We lock the 689 nm beam on  $A^2\Pi_{1/2}(N=1, G=0, F=1) \iff A'^2\Delta_{3/2}(J'=3/2, F=2)$  transition. The beam is aligned perpendicular to gravity to prevent molecules from falling.

### 7.2.2 Discussion

We briefly tried this 689 nm ODT for 2 months, but didn't trap any molecules. The possible reasons are:

- (1) Low trap depth: Our trap depth is limited by the 689 nm TA power, which is only 250 mW. A 15  $\mu\text{K}$  is hard to trap molecules with the temperature of 10  $\mu\text{K}$  if cooling is not working in the lattice. A deeper trap can be achieved with a lower detuning, but the scattering loss will be enhanced, following  $\Gamma_{sc} = \frac{\Gamma}{\hbar\Delta}U_{dip}$ . This can be improved with a SFG laser from Precilasers which generates watts of power at 689 nm.
- (2) Amplified spontaneous emission(ASE): Our trapping beam is amplified by a TA, which contains a broadband ASE. The close-resonance ASE would scatter molecules quickly which limits the trap lifetime. ASE filters with GHz bandwidth can be used to block the unwanted light. A SFG laser can also solve this problem.
- (3) Gravity: For a weak trap, a small( $0.5^\circ$ ) angle would be enough for molecules to fall under gravity, as described previously in Figure 7.3.

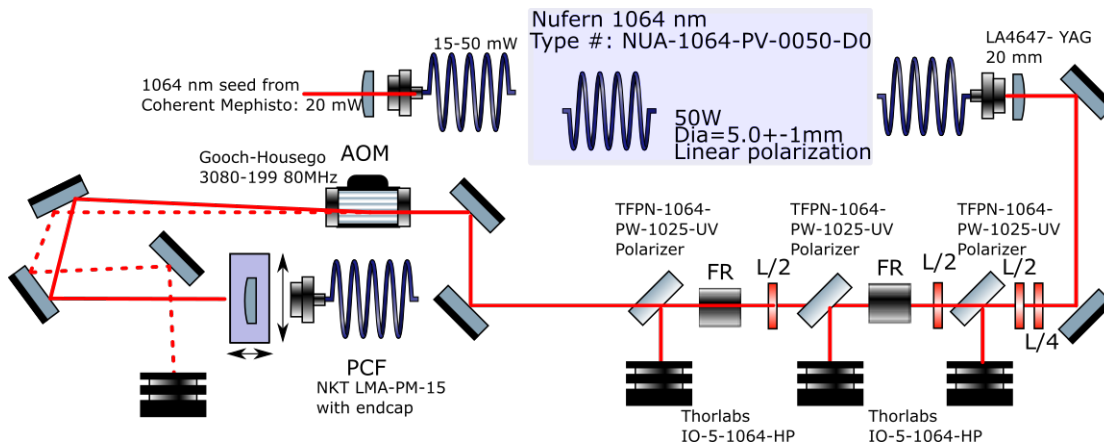


Figure 7.4: 1064 nm beam preparation and optical setup. The high power AOM is used to turn 1064 nm beam on and off. The whole setup is surrounded by aluminum enclosure to prevent dust and possible scattering. The entire system takes 1.5 hours to warm up.

### 7.3 1064 nm ODT

According to Figure 7.1, we decided to create a deeper optical trap of YO at 1064 nm where single frequency, high power, low noise amplifier is available. Compared with 689 nm ODT, 1064 nm ODT has deeper trap depth, lower scattering rate and smaller differential AC stark shift between hyperfine manifolds. We focused 11 W of light to a beam waist of  $50 \mu\text{m}$ , creating a trap depth of  $20 \mu\text{K}$  with radial(axial) trapping frequencies  $\omega_r(\omega_z) = 2\pi \times 220(0.96)$  Hz. In this case, the scattering rate is about 0.3 Hz, which is long enough for us at the moment. The full beam preparation and optical setup for 1064 nm ODT are shown in figure 7.4.

#### 7.3.1 Experiment Setup

A low noise, narrow bandwidth 1064 nm seed from Coherent Mephisto laser is amplified by a thousand times( $15\text{mW} \rightarrow 50\text{W}$ ) using a fiber amplifier(Nufern NUA-1064-PV-0050-D0), as shown in Figure 7.4. A high power AOM is used to switch and stabilize the trapping beam intensity. This high power beam was delivered to the vacuum chamber via a fiber. A normal step-index fiber can not handle power higher than 2 W, mostly due to stimulated Brillouin scattering(SBS). SBS arises from the light coupling with the phonon modes where the forward-traveling photons scatter into a phonon and a backwards-traveling photon. In this case, an interference pattern is formed,

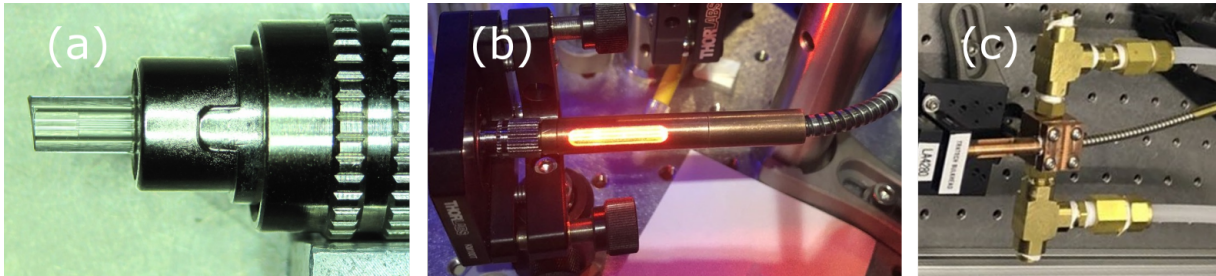


Figure 7.5: (a) Fiber end cap. A 1 mm long fused silica end cap is bonded at the fiber tip to increase the beam size at the air-to-gap interface that protects the tip from burning. (b) Copper ferrule. The shining orange light is the miscoupled beam. The hollow structure allows this light to escape without causing extra heat. In this picture, we couple 614 nm laser just for demonstration. (c) Custom-made water cooling block.

which modulates the local density of the fiber. This is a stimulated, non-linear process since this interference pattern enhances the back scattering of the photon. A power threshold exists when the back-scattered power is comparable to the input power[148]. The threshold is determined by the fiber length, core diameter, dielectric material, and the wavelength of the light. For example, the threshold is only  $\sim 3$  watt for coupling 1064 nm laser if a 5 meter long, step-index, fused silica fiber with  $5 \mu\text{m}$  core is used [149, 150]. To overcome this problem, we use a photonic crystal fiber(NKT LMA-PM-15) where a large mode area( $12.6 \mu\text{m}$ ) is achieved by guiding light through its photonic structure. Besides, a fused silica end cap(Tratech Fiberoptics HP 2.5), shown in Figure 7.5 (a), covers the input and the output of the fiber to prevent the possible burning at the fiber tip. This reduces the intensity at the air-to-end cap interface by increasing the beam diameter. A custom-made copper block is used to holds the copper ferrule for water-cooling, as shown in Figure 7.5 (c). We attach a thermocouple to the copper ferrule(close to the fiber tip) and program a temperature interlock system to protect the fiber from overheating. If the temperature exceeds  $40^\circ\text{C}$ , the interlock will disabled the AOM, leaving all laser power on the beam dump, as shown in Figure 7.4. When operating the fiber constantly at high power ( $>10 \text{ W}$ ), the temperature stays at around  $40^\circ\text{C}$ . This can be improved with better cooling power.

Care must be taken when working with high power lasers. Under high intensity, thermal lensing and unexpected reflection are problematic for stability and safety. Special optics are used to minimize these effects[151]:

- All reflective/transmissive optics are HR/AR V-coated at 1064 nm to minimize the transmission/reflection.
- All transmissive optics are fused silica to reduce the thermal expansion and absorption. Compared to N-BK7,  $\text{CaF}_2$  and  $\text{MgF}_2$ , fused silica has comparable transmittance but much lower coefficient of thermal expansion( $5.5 \times 10^{-7}/^\circ\text{C}$ ) which reduces thermal lensing effect.
- Low power polarizing beamsplitter cubes are epoxied together, which can be easily damaged



by high power laser beams. This can be prevented by using optical bonding or thin-film polarizer. In our experiment, we use thin-film plate polarizers(CVI TFPN-1064-PW-1025-UV) to further reduce the back-reflection.

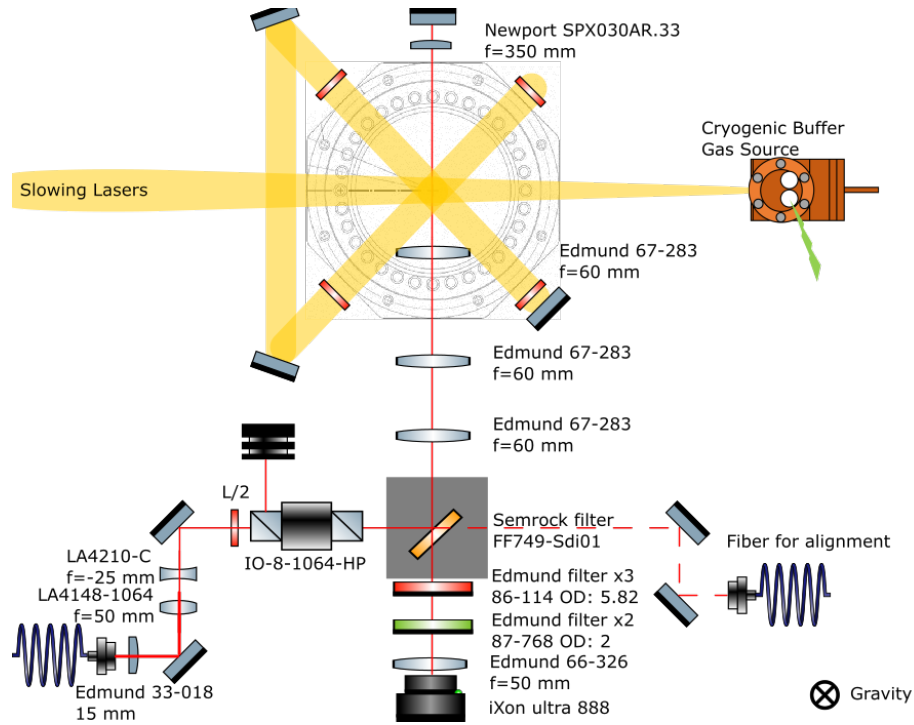


Figure 7.6: ODT and lattice optics beam paths and imaging optics. In ODT, the trapping beam is dumped at the top of the figure while the beam is retroreflected in 1D optical lattice.

An overview of the optical layout is shown in Figure 7.6. Limited by the optical access, 1064 nm beam shares the same path with the imaging system. The 1064 nm beam first go through a telescope for a smaller beam waist. Then, an isolator is used, specifically for optical lattice, to block the retro-reflected beam. The trapping beam is coupled into the chamber by a dichroic mirror(Semrock: FF749-Sdi01) and then collimated, dumped(retro-reflected) on the other side of the chamber for ODT(lattice) setup. S polarization is chosen to minimize the transmission through the dichroic mirror, which reduces the amount of retro-reflected light leaking into the camera. The transmitted light from the dichroic mirror is coupled into a single mode fiber for alignment and power stabilization. It is worth mentioning the isolator should be placed far away from the

molecular cloud since the laser cooling is sensitive to the magnetic field.

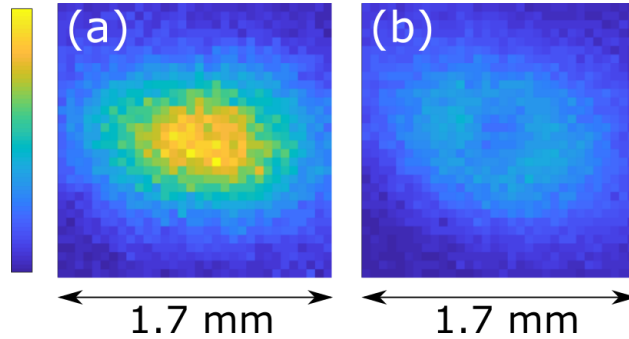


Figure 7.7: We use 689 nm depletion to align the 1064 nm beam. We first deplete the molecules with a weak 689 nm beam and then overlap 1064 nm trapping laser to the 689 nm beam. (a) Molecule cloud after GMC, without depletion. (b) With weak 689 nm depletion. A well aligned 689 nm beam depletes a hole at the center of the cloud.

In order to align ODT beam on the molecular cloud, we first depleted molecules with 689 nm light, as shown in Figure 7.7 and then overlapped 1064 nm beam to the 689 nm beam. After this initial alignment, the fine tuning was done by examining the position of trapped molecules. The ODT beam should be perpendicular to the direction of gravity to prevent leaking. This will be detailed in Section 7.3.3. Once the beam was aligned, the focus was adjusted to maximize the number of trapped molecules, as shown in Figure 7.8 (a).

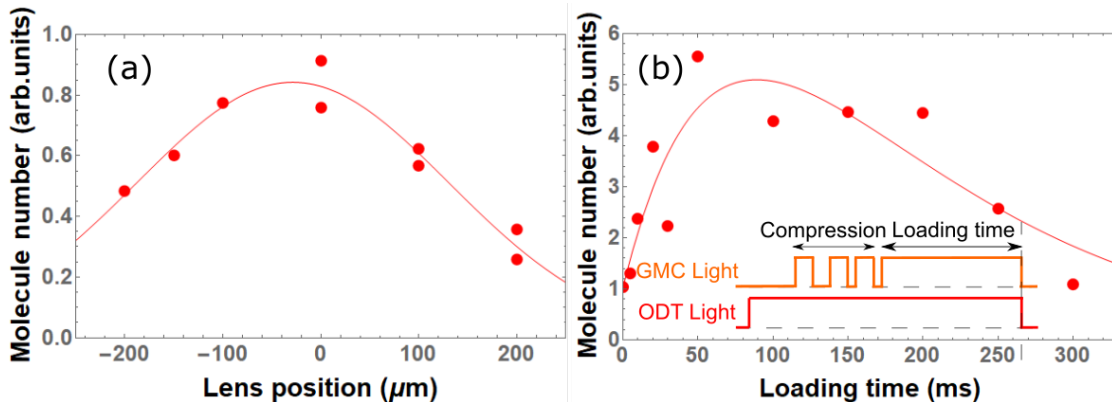


Figure 7.8: (a). Number of loaded molecules vs lens position. (b). Number of loaded molecules into the ODT as a function of loading time with GMC cooling. The timing diagram is shown in the inset.

### 7.3.2 Loading and Cooling inside ODT

In order to capture more molecules in the optical trap, the ODT light was switched on at the beginning of the GMC compression sequence, as shown in the inset of Figure 7.8 (b). Since the loading efficiency depends on the ability to cool molecules in the trap, we explore the dependence of trapped molecule number on various cooling parameters. We first scanned the loading curve by varying the overlap duration between GMC and ODT. As shown in Figure 7.8 (b), we found that the number of trapped molecules increased by a factor of 5 and reached the peak at 70 ms. We didn't perform a direct loading measurement to prove the cooling enhances the loading. But the peak loading efficiency ( $\sim 4\%$ ) is much higher than simply trapping the molecules within the beam waist ( $< 1\%$ ). This implies that GMC cools the nearby molecules and helps them fall into the trap.

In an optical trap, the trapping potential relies on the spatially varying Stark shift where differential Stark shifts are also created between hyperfine manifolds. These differential Stark shifts impede efficient cooling inside the trap by breaking the coherence needed for GMC. Therefore, we first varied the Raman detuning  $\delta$ . As shown in Figure 7.9 (b)(c), we observe the loading peaks are slightly offset from the Raman resonance condition in freespace by  $\sim$  tens of kHz. This on the same order of the estimated differential ac Stark shift arising from the ODT.

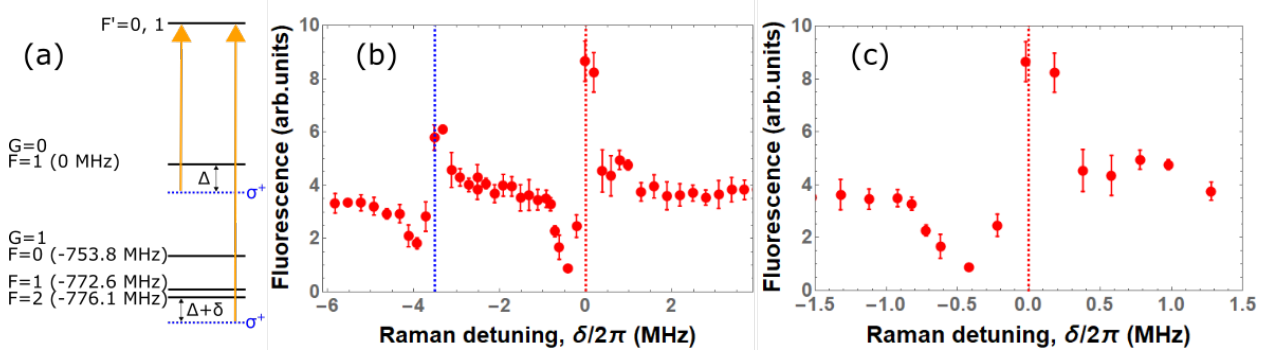


Figure 7.9: Dependence of ODT loading on Raman detuning  $\delta$ . (a). GMC configuration. (b). Fluorescence of trapped molecules vs Raman detuning  $\delta$ . Blue and red dashed lines represent  $G=0, F=1$ ,  $G=1, F=1$  Raman resonance and  $G=0, F=1$ ,  $G=1, F=2$  Raman resonance. (c). Zoom in of (b) around  $\delta = 0$ . The data points are not enough to determine the exact optimal  $\delta$  but the optimal loading detuning is  $\sim$  tens of kHz compared to the Raman resonance condition in free space.

Unfortunately, Raman resonance condition can not be fulfilled at each location of the trap due to the spatially varying Stark shift. In order to load more molecules, a high intensity GMC beam can be applied to broaden the  $\Lambda$ -enhanced cooling feature. We investigate the loaded number dependence on the intensity  $I$  while keeping Raman detuning  $\delta/2\pi=20$  kHz and the single-photon detuning  $\Delta/2\pi=+40$  MHz ( $8.3\Gamma/2\pi$ ). We find that the loaded number increases with GMC intensity, shown in Figure 7.10, consistent with the idea that increased intensity reduces the sensitivity to  $\delta$ . We confirmed this statement by scanning the loading dependence on  $\delta$  in lattice with different cooling intensities. The results are detailed in Section 7.4.1.

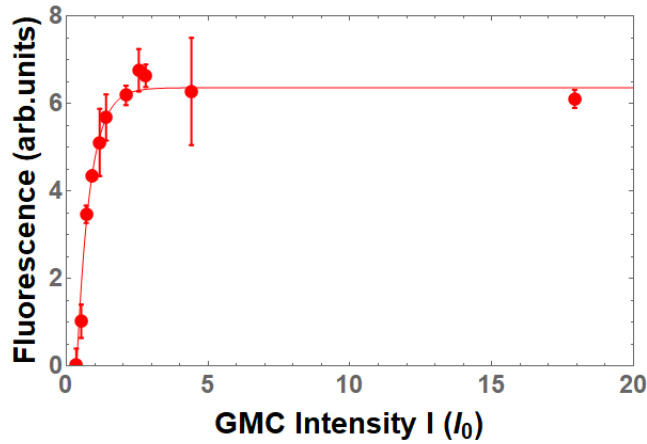


Figure 7.10: Number of loaded molecule versus GMC intensity at a trap depth of  $20 \mu\text{K}$ . We keep the Raman detuning  $\delta/2\pi=20$  kHz and the single-photon detuning  $\Delta/2\pi=+40$  MHz.

### 7.3.3 ODT Lifetime

Our first ODT was very short-lived( $31(4)$  ms), as shown in Figure 7.11 (a) in blue. This short lifetime also limits the loading process described in the previous chapter. This leakage results from the molecule falling under gravity and it is limited by the longitudinal trapping frequency, as described previously in Figure 7.3 . After a better alignment, the lifetime increased significantly to  $83(8)$  ms, as shown in Figure 7.11 (a) in red. This is still too short compared to the estimated lifetime from ODT scattering( $> 3\text{s}$ ) and background collision( $\sim\text{s}$ ). In order to exclude the background

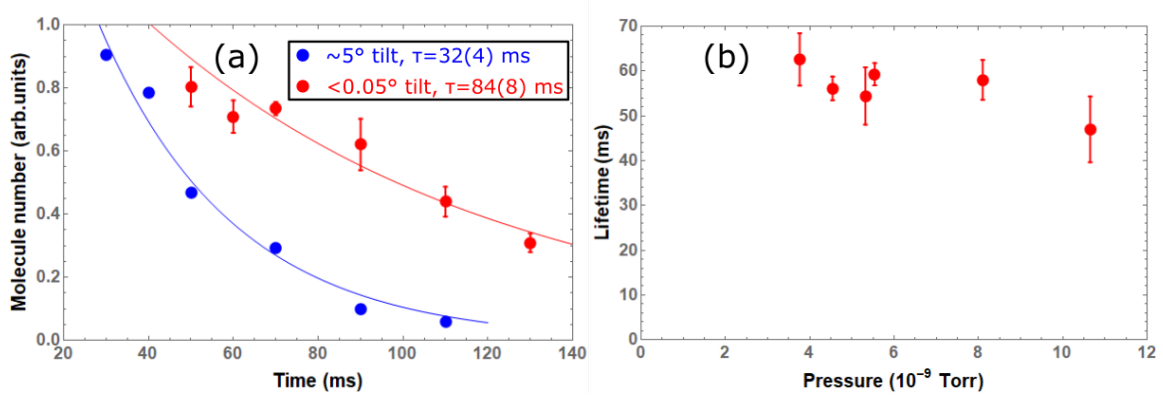


Figure 7.11: (a). Loss of trapped molecules in a trap. Molecules leave the trap at a faster rate if the trap is tilted. (b). ODT lifetime at different pressures. The pressure is adjusted by changing the helium flow and the opening time of the in-vacuum shutters. Collision with background gas is not limiting the current ODT lifetime. The typical operating pressure is  $\sim 3 \times 10^{-9}$  Torr.

collision, we performed the lifetime measurement at different pressures by varying the helium flow rate and the opening time of the in-vacuum shutters, as shown in Figure 7.11 (b). Apparently, the background collision is not limiting the ODT lifetime at the moment. We suspect that molecules are still leaving from the axial direction as the axial trapping frequency is only  $\sim 1$  Hz. There are two ways to enhance the trapping along axial direction: shrinking the focused beam waist, which reduces the loading efficiency, or adding another trapping laser to form a crossed ODT/optical lattice. We chose the 1D lattice for efficient trapping.

#### 7.4 1064 nm Optical Lattice

If the ODT beam is directly retro-reflected by a mirror shown in Figure 7.6, it forms an interference pattern with the incoming beam, creating a 1D lattice structure. Thanks to the lattice structure, the longitudinal trapping frequency is greatly enhanced. A deeper trap is created with the same trapping intensity. A 11 W 1064 nm light creates a trap depth of  $60 \mu\text{K}$  with radial(longitudinal) trapping frequencies  $\omega_r(\omega_z) = 2\pi \times 0.44(93)$  kHz and a scattering rate of 1.2 Hz. The full beam preparation and optical setup for 1D optical lattice are shown in Figure 7.4 and 7.6.

### 7.4.1 Loading and Cooling inside Lattice

The loading and cooling is very similar to the ODT setup. After 50 ms cooling inside the lattice, the cooling light was switched off for 40 ms to allow the untrapped molecules to escape from the detection region. Figure 7.12 shows the loading and cooling of molecules into the optical lattice. Since a deeper trap is formed in the lattice, we first varied the Raman detuning  $\delta$  with single-photon detuning  $\Delta/2\pi$  for  $G=0$   $F=1$  fixed at +40 MHz ( $8.3\Gamma/2\pi$ ) and  $I = 3I_0$ , where  $I_0=2.7$  mW/cm<sup>2</sup> is the estimated saturation intensity. As shown in Figure 7.12(b), the optimal two-photon detuning  $\delta_{trap}$  in the trap is shifted by  $\sim 2\pi \times 70$  kHz compared to the Raman resonance  $\delta_{free}=0$  in free-space, on the same order as the calculated differential Stark shifts between  $G=0, F=1$  and  $G=1, F=2$ . It is about 4 times larger than the optimal Raman detuning in ODT, as expected. Since the spatial varying Stark shift is inevitable, one way to reduce the sensitivity on Raman detuning  $\delta$  and achieve a lower temperature is to increase the single-photon detuning  $\Delta$ . With  $I=5.5I_0$  and  $\delta_{trap} = 2\pi \times 70$  kHz, the loading increases with single-photon detuning  $\Delta$  and saturates at  $\sim 2\pi \times 20$  MHz, shown in Figure 7.12(c). Another way to load more molecules is to increase the cooling intensity. With a high GMC intensity, the  $\Lambda$  cooling feature is broadened at the cost of raising the lowest attainable temperature. We investigated the loaded number dependence on the intensity  $I$  while keeping Raman detuning  $\delta_{trap} = 2\pi \times 70$  kHz and the single-photon detuning  $\Delta/2\pi=+40$  MHz ( $8.3\Gamma/2\pi$ ). As shown in Figure 7.12(d), the loaded number increases with intensity and eventually saturated at  $\sim 2I_0$ . To prove it is the case, we scanned the Raman detunings  $\delta$  at different intensities and observed a broader Raman feature at higher GMC intensity, shown in the inset of Figure 7.12 (d). The lowest temperature also increases with high intensity, consistent with the theory [134]. These confirm our previous hypothesis that the loading dependence on Raman detuning  $\delta$  decreases with intensity  $I$  or single-photon detuning  $\Delta$ .

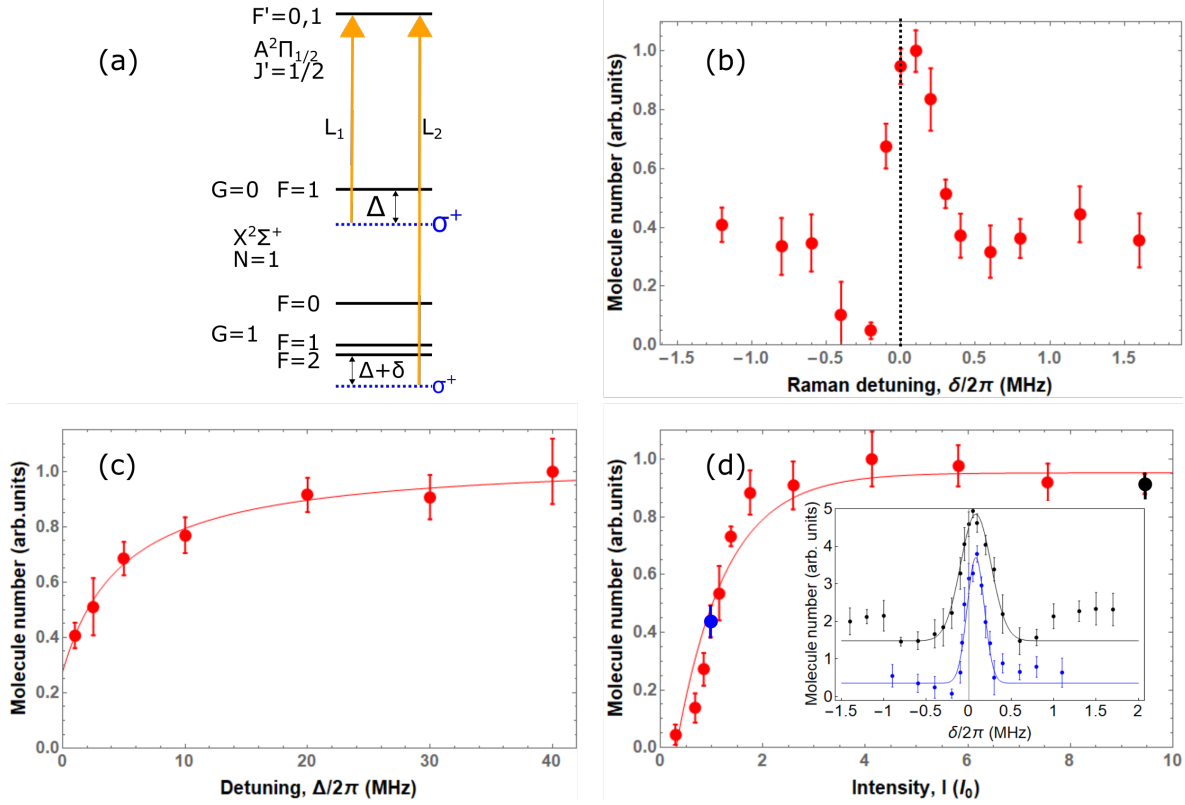


Figure 7.12: Dependence of lattice loading on GMC parameters. (a). GMC configuration. (b). Lattice LIF vs Raman detuning  $\delta$ . (c). Lattice LIF vs One photon detuning  $\Delta$ . (d). Lattice LIF vs GMC intensity. The inset shows the  $\Lambda$ -enhanced feature at different intensities. The  $\delta$  dependence decreases with intensity  $I$ .

#### 7.4.2 Lattice Characterization

The important lattice parameters are lattice trapping frequency, lifetime and heating rate. As for the trapping frequency, we haven't performed a direct measurement yet. Instead, the trapping frequency is currently inferred from the ODT transverse trapping frequency and the lattice geometry. I should be clear that the correct way is to directly measure the trapping frequencies by introducing intensity(pointing) noise into the trapping beam. But let me briefly explain what we've performed.

We measured the transverse trapping frequency of ODT by oscillating the center of the trap. This is achieved by modulating the beam pointing using a piezo actuated mirror. If the

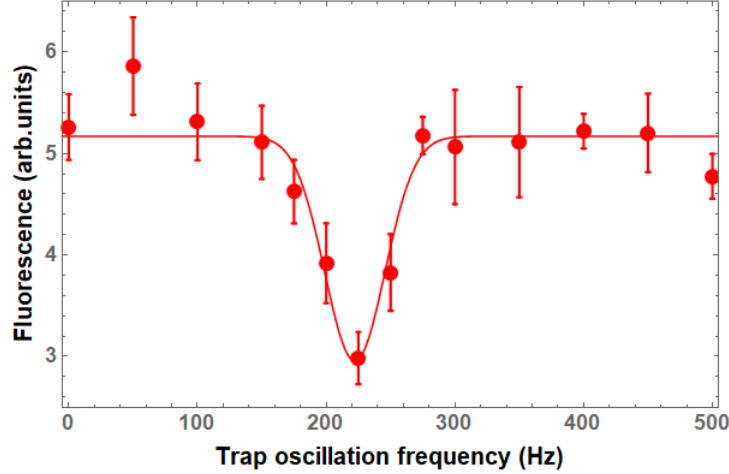


Figure 7.13: Measure the trapping frequency of the lattice by oscillating the center of the trap. If the center of the trap oscillates at the trapping frequency, molecules are heated and therefore escape from the trap.

trap is oscillating at the trapping frequency, molecules would be heated and then escape from the trap [152]. We loaded molecules into the trap, oscillated the trap center at various frequencies and observed the number of remaining molecules after oscillation. As shown in Figure 7.13, the transverse trapping frequency of the ODT is  $2\pi \times 222$  Hz. Assuming the perfect retro-reflection, the transverse trapping frequency of the lattice is  $2\pi \times 0.44$  kHz. With a  $50 \mu\text{m}$  beam waist at the focus, the longitudinal trapping frequency of the lattice is  $2\pi \times 93$  kHz.

The other properties of an optical lattice are the lifetime of trapped molecules and the heating rate induced by the lattice beams. After loading molecules into the lattice, we switched off all the other beams except the lattice light, and measured the number of remaining molecules after various amount of time. The results are shown in Figure 7.14 (a), from which we extract the lifetime to be  $850(70)$  ms. Our vacuum pressure is  $\sim 3 \times 10^{-9}$  Torr, and we attribute the limitation of lifetime to collisions with background gas. To determine the heating rate, we switched off the GMC beams after cooling molecules to  $7 \mu\text{K}$ , and measured how their temperatures evolve over time using the standard ballistic expansion method. As shown in Fig. 7.14 (b), no noticeable heating is observed within 500 ms.



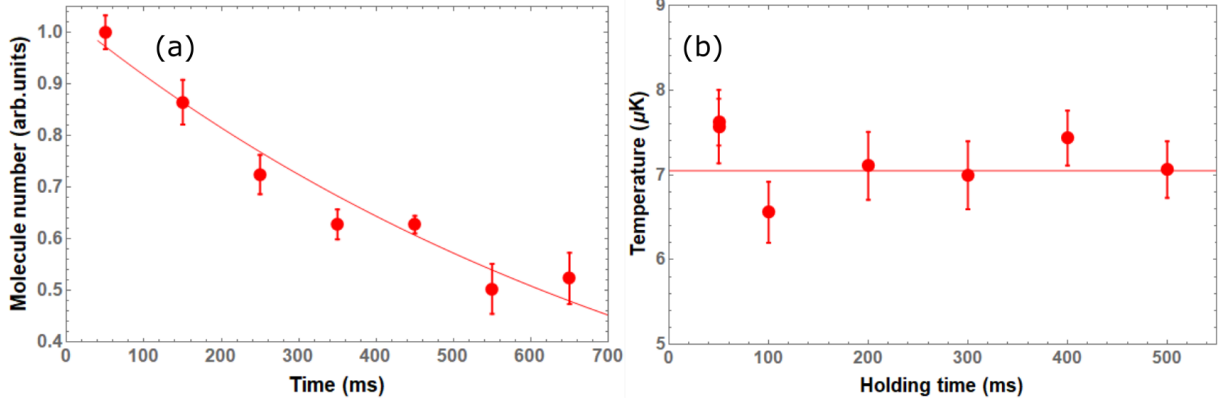


Figure 7.14: Characterization of 1D optical lattice. (a) Measurement of lattice lifetime. The solid line is an exponential fit with a  $1/e$  constant of 850(70) ms. (b) Measurement of molecules heating rate inside the lattice. The error bars in the plots correspond to  $1\sigma$  statistical uncertainty. The extracted heating rate is  $-0.4(0.7)\mu K$ .

With optimized parameters ( $\Delta = 8.3\Gamma$ ,  $\delta = 2\pi \times 70$  kHz,  $I_{loading} = 5.5I_0$ ,  $I_{cooling} = 3.0I_0$ , trap depth  $60 \mu K$ ,  $\omega_t = 2\pi \times 440$  Hz,  $\omega_l = 2\pi \times 93$  kHz, scattering rate 1.2 Hz), 1200 molecules are transferred into the 1D lattice with a temperature of  $7.0(6) \mu K$ . The peak density is  $1.2 \times 10^{10} \text{ cm}^{-3}$  and the phase space density is  $3.1 \times 10^{-6}$ . This is the highest phase space density of molecules achieved by direct laser cooling.

### 7.4.3 Molecule Loss with Low Intensity GMC Beams

Once the lattice is loaded, we apply an extra GMC pulse with different parameters compared to the loading. In this final stage, the cooling powers are still equally distributed between two components, but the intensity  $I$  is lowered to achieve a low temperature. We keep Raman detuning  $\delta = 2\pi \times 70$  kHz where the loading is the most efficient. After 8 ms of GMC, we measure the temperature using the standard ballistic expansion method. As shown in Figure 7.15 (b), the temperature decreases linearly with the intensity which we attribute to the reduced momentum diffusion, consistent with theoretical prediction [128].

In our previous work [59], we also observed that the temperature of YO gray molasses in free space decreases with light intensity. The trend stops when the intensity is too low to hold the

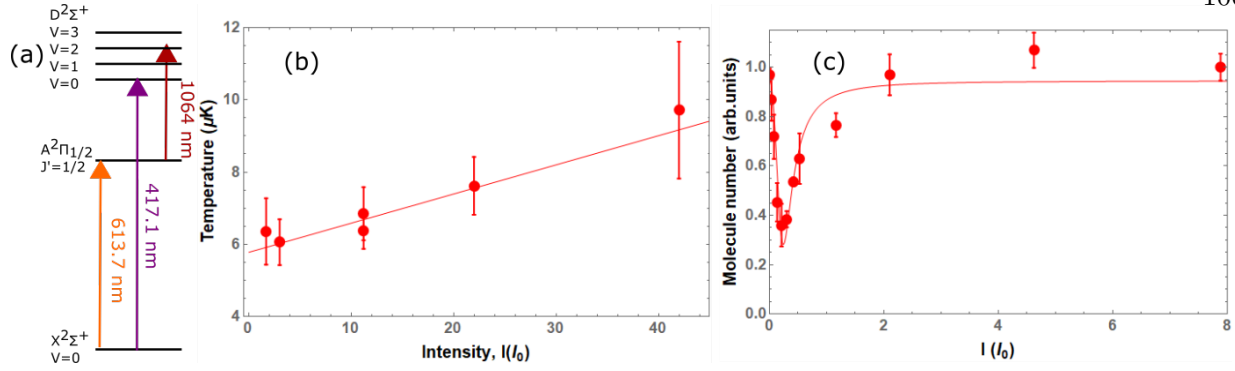


Figure 7.15: Molecule loss in lattice enhanced by low intensity GMC beams. (a). YO level structure with possible loss mechanism. (b). Temperature versus GMC intensity  $I$  with  $\Delta=8.3\Gamma$  and  $\delta=2\pi\times 70$  kHz. The solid line is a linear fit. (c). Number of remaining molecules versus GMC intensity  $I$  with  $\Delta=8.3\Gamma$  and  $\delta=2\pi\times 70$  kHz.. The solid line is a fit to the function  $N=N_0-k\times\rho_{ee}(I)$  where  $\rho_{ee}$  represents the excited state  $A^2\Pi_{1/2}$  population calculated in the theoretical predictions in Ref. [153]. Molecules in  $A^2\Pi_{1/2}$  state could be lost after scattering 1064 nm photons.

molecules against gravity. With molecules trapped inside the lattice, we ramped down the GMC intensity in order to obtain an even lower temperature. However, we observed a striking molecular loss near GMC intensity of  $I=0.21 I_0$ , shown in Figure 7.15 (c).

With a non-zero Raman detuning  $\delta$ , molecules can be populated up to  $A^2\Pi_{1/2}$  state at low GMC intensity [153] and then become lost through  $A'^2\Delta_{3/2}$  decay channels. In the  $X^2\Sigma^+$  state of YO, there is a close splitting between  $G=1 F=1$  and  $G=1 F=2$  manifolds (3.5 MHz). In this case, even a Raman resonance condition is fulfilled between  $G=0 F=1$  and  $G=1 F=2$ , there is still a non-zero Raman detuning  $\delta$  between  $G=0 F=1$  and  $G=1 F=1$  states, populating molecules to  $A^2\Pi_{1/2}$  state. Even if the Raman resonance condition is fulfilled at the trap center, the spatially inhomogeneity breaks the resonance at the edge of the trap. To verify that the molecules excited to  $A^2\Pi_{1/2}$  state are not leaking into  $A'^2\Delta_{3/2}$  state, we measured the decay curve at intensity  $I = 0.21I_0$ , as shown in Figure 7.16. Based on the branching ratio  $3 \times 10^{-4}$  and the fitted decay time constant 41(2) ms, the calculated scattering rate is  $8 \times 10^4 \text{ s}^{-1}$ , which is more than two orders of magnitude larger than the GMC scattering rate. Therefore, the loss is not due to the  $A'^2\Delta_{3/2}$  state leakage.

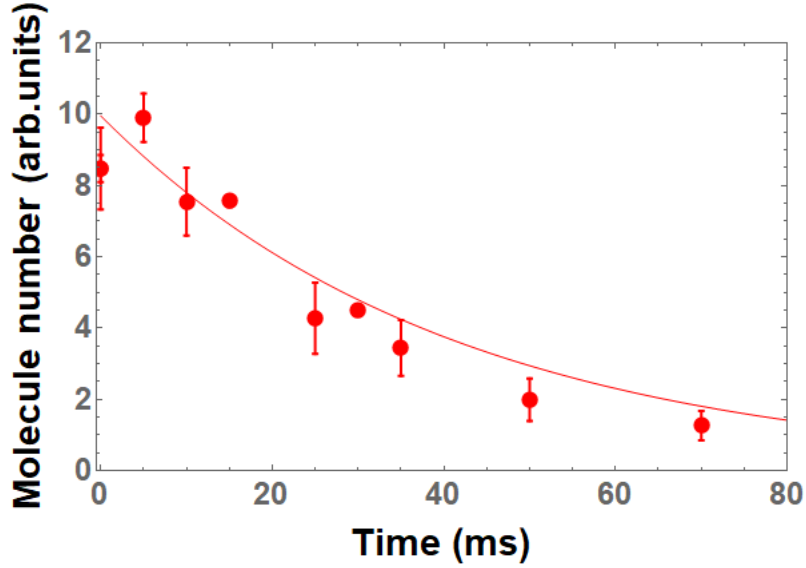


Figure 7.16: Molecule loss in the lattice with low power GMC beam( $I=0.21I_0$ ). The solid line is an exponential fit. The  $1/e$  time constant is 41(2) ms.

We attribute this loss to excitation to  $D^2\Sigma^+$  through  $A^2\Pi_{1/2}$  with a 1064 nm photon [87]. Among all electronic states,  $D^2\Sigma^+$  is  $\sim 230$  THz higher than our excited state  $A^2\Pi_{1/2}$  [87]. Therefore, a 1064 nm photon(280 THz) is reasonably close to the  $A^2\Pi_{1/2} \rightarrow D^2\Sigma^+$  transition. Molecules first get excited to  $A^2\Pi_{1/2}$  state by low intensity GMC beam, then get pumped up to  $D^2\Sigma^+$  by the 1064 nm photon and eventually decay back. This is a three-photon process, as a result, molecules decay to rotational states with opposite parity compared with the initial  $X^2\Sigma^+$  states in the  $X^2\Sigma^+ \rightarrow A^2\Pi_{1/2}$  cycle. Currently, we're taking more data to explore the remaining molecule number dependence on intensity  $I$ , single-photon detuning  $\Delta$  and Raman detuning  $\delta$ . These data can help us gain a better understanding of the loss mechanism.

#### 7.4.4 Heating at Low Intensity

In addition to the molecule loss, the excitation into  $A^2\Pi_{1/2}$  is undesirable for reaching a low temperature due to the momentum diffusion. In Figure 7.17, we observe a heating rate of  $84(18)$   $\mu\text{K}/\text{s}$  with  $\Delta/2\pi = 40$  MHz,  $\delta_{\text{trap}}/2\pi = 70$  kHz and  $I=0.06 I_0$ . As has been observed [61, 62, 154, 155] and discussed [134] previously, the temperature  $T = D_p/(\alpha \times k_B)$  would decrease with single-photon detuning  $\Delta$  as the momentum diffusion coefficient  $D_p$  is reduced, while the friction coefficient  $\alpha$  is independent of  $\Delta$ . To suppress the one photon scattering, we increase the single-photon detuning  $\Delta/2\pi$  from +40 MHz to +120 MHz. At +120 MHz, the heating rate becomes unnoticeable but the lowest temperature remains at  $\sim 7$   $\mu\text{K}$ . The current low temperature limit in the lattice might be caused by another mechanism such as the interference/dephasing between the lattice and GMC beams.

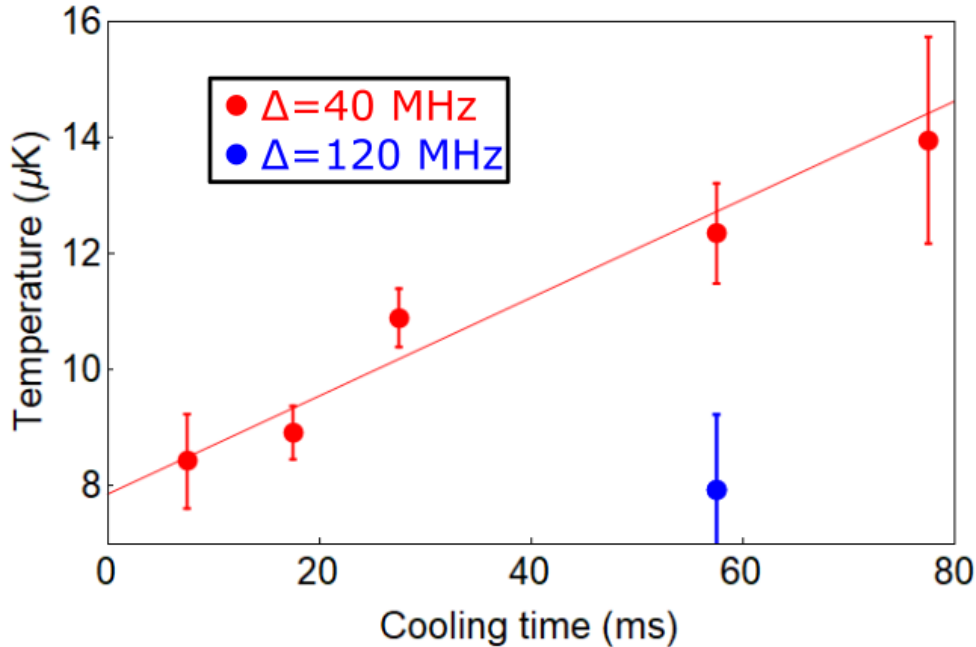


Figure 7.17: GMC heating inside the lattice with  $\delta_{\text{trap}}/2\pi = 70$  kHz and  $I=0.06 I_0$ . The heating is suppressed with a large single-photon detuning  $\Delta$ .

#### 7.4.5 Ramping Down the Lattice

Once the molecules are cooled inside the lattice, all the lasers are removed except the 1064 nm trapping beams. We next linearly ramped down the trap depth in 50 ms and holded at the final depth for another 6 ms. Since the CCD is aligned along the lattice axis, the ballistic expansion measurements determine the temperature in the transverse direction. As shown in Figure 7.18, the temperature decreases as the trap depth gets shallower. This is expected as density decreases during the expansion, temperature should be reduced if the phase space density is conserved. Similar observation has been reported in other systems [156, 157], but our transverse temperatures seem to decrease a little faster than expected. Assuming the molecules are fully thermalized that longitudinal temperature is the same as the transverse one, we plotted the calculated temperature (solid) and its 95% confidence interval (dashed) from fitting the molecule number associated with the molecular loss and a constant phase space density. Clearly, the transverse temperature decreases faster than what is assumed under a conserved phase space density. A sharp molecule loss at low trap depth is also observed. A systematic longitudinal temperature measurement and thermalization study is required to understand the physics.

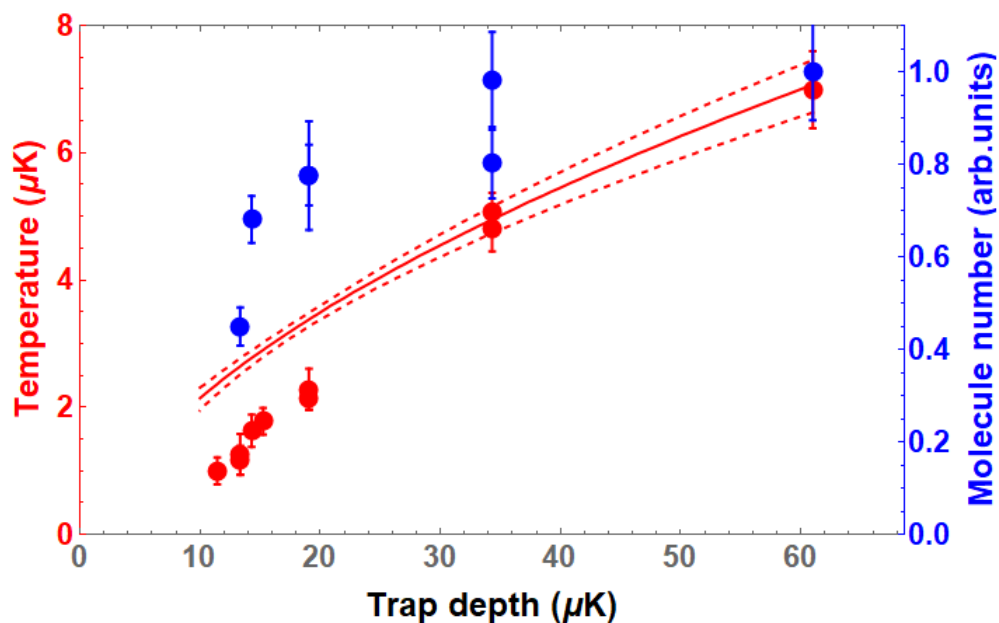


Figure 7.18: Achieving the coldest temperature by ramping down the trap depth. We load the molecules at the trap depth of 60  $\mu\text{K}$ , ramp down to different final trap depth in 50 ms and hold for 6 ms. The red dots represent the temperature measured along the transverse direction. The red solid line shows the calculated temperature under conserved phase space density, with 95% confidential interval showing in dashed. The blue dots represent the remaining number of molecules after the ramp.

### 7.4.6 Noise-induced Heating

There are two main sources of heating in far-off-resonance optical traps. Heating rates are estimated in terms of the intensity and position noise power spectrum measured for fiber amplifier. Intensity noise causes fluctuations in the trapping frequency resulting in exponential heating, while beam-pointing noise introduces fluctuations of the trap center and leads to heating at a constant rate. In this section, we consider a molecule in a one-dimensional harmonic-oscillator potential with a fluctuating spring constant and a fluctuating equilibrium position.

The heating rate by intensity noise can be calculated as follows [152]. For a focused Gaussian laser beam with field amplitude  $\tilde{E}$  and beam waist  $\mathbf{a}$ , the potential can be approximated as  $-V_0 + \frac{1}{2}kx^2$ , where  $\alpha$  is the polarizability,  $V_0 = \alpha \frac{|\tilde{E}|^2}{4}$  is the maximum light shift and  $k = 2\frac{V_0}{a^2}$  is the spring constant. Since both  $V_0$  and  $k$  are proportional to the laser intensity  $I(t)$ , the spring constant fluctuates in time. This leads to an effective Hamiltonian:

$$H = \frac{p^2}{2M} + \frac{1}{2}M\omega_{tr}^2[1 + \epsilon(t)]x^2$$

where  $\omega_{tr} = \sqrt{\frac{k_0}{M}}$  is the averaged trapping frequency and  $\epsilon(t) = \frac{I(t)-I_0}{I_0}$  is the fractional fluctuation of the spring constant due the laser intensity. Using the 1st order perturbation theory, one could find that the average energy increases exponentially:

$$\langle \dot{E} \rangle = \Gamma_\epsilon \langle E \rangle$$

where the rate constant  $\Gamma_\epsilon$  is

$$\Gamma_\epsilon = \pi^2 \nu_{tr}^2 S_\epsilon(2\nu_{tr})$$

Here the  $\nu_{tr}$  is the trapping frequency in Hz,  $S_\epsilon(2\nu_{tr})$  is the power spectral density at twice the trapping frequency and  $T_I = 1/\Gamma_\epsilon$  is the time to increase the energy by a factor of  $e$ , known as e-folding time. The energy e-folding time  $T_I$  directly limits the time that molecules can stay inside the trap. Molecules will leave the trap when their energy is similar to the trap depth. In a 3D trap, the heating rate will be the mean of the rates along all directions [152]. Similarly, pointing

fluctuation introduces heating with the effective Hamiltonian:

$$H = \frac{p^2}{2M} + \frac{1}{2}M\omega_{tr}^2[x - \epsilon(t)]^2$$

where  $\epsilon(t)$  is the fluctuation of the trap center [158]. We could get

$$\langle \dot{E} \rangle = \frac{\pi}{2}M\omega_{tr}^4 S_x(\omega_{tr})$$

where the heating is independent of the trap energy,  $S_x(\omega)$  is the power spectrum of the position fluctuations in the trap center.

Our optical trapping light is not suffering noticeable heating at the moment. The seed laser(Coherent Mephisto) has extraordinary low noise [159] and we're mostly limited by our fiber amplifier, characterized in [151]. Here I attach the relative intensity noise(RIN) spectrum of our trapping light and the calculated e-folding time  $T_I$ . In Figure 7.19 (a), we could see the intensity servo suppress the intensity noise thus the e-folding time  $T_I$  is not limiting the trap lifetime. It is worth mentioning that when the intensity is servoed, the witness photo diode observed more noises at several frequencies(466 Hz, 933 Hz, 1 kHz) and it is also much more noisier than the photo diode in the loop. The in loop photo diode detects the light from a fiber, which would convert the pointing noise into intensity noise. This can be solved by monitoring the intensity from free space.

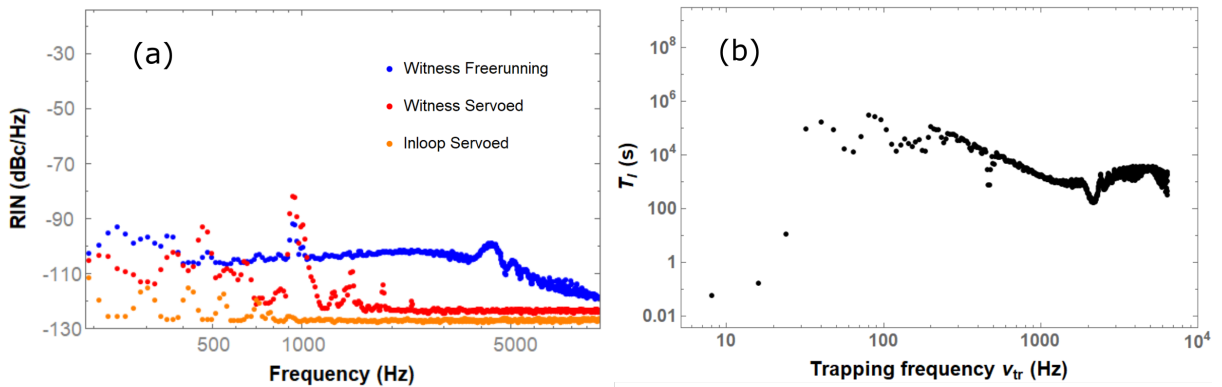


Figure 7.19: Relative intensity noise spectrum and e-folding time. (a). RIN of 1064 nm laser. (b). e-folding time  $T_I$  from intensity noise.



## Bibliography

- [1] Mike H Anderson, Jason R Ensher, Michael R Matthews, Carl E Wieman, and Eric A Cornell. Observation of bose-einstein condensation in a dilute atomic vapor. science, 269(5221):198–201, 1995.
- [2] Brian DeMarco and Deborah S Jin. Onset of fermi degeneracy in a trapped atomic gas. science, 285(5434):1703–1706, 1999.
- [3] Immanuel Bloch, Jean Dalibard, and Wilhelm Zwerger. Many-body physics with ultracold gases. Reviews of modern physics, 80(3):885, 2008.
- [4] Chris Monroe, David M Meekhof, Barry E King, Wayne M Itano, and David J Wineland. Demonstration of a fundamental quantum logic gate. Physical review letters, 75(25):4714, 1995.
- [5] Mark Saffman, Thad G Walker, and Klaus Mølmer. Quantum information with rydberg atoms. Reviews of modern physics, 82(3):2313, 2010.
- [6] Kihwan Kim, M-S Chang, Simcha Korenblit, Rajibul Islam, Emily E Edwards, James K Freericks, G-D Lin, L-M Duan, and Christopher Monroe. Quantum simulation of frustrated ising spins with trapped ions. Nature, 465(7298):590–593, 2010.
- [7] Markus Greiner, Olaf Mandel, Tilman Esslinger, Theodor W Hänsch, and Immanuel Bloch. Quantum phase transition from a superfluid to a mott insulator in a gas of ultracold atoms. nature, 415(6867):39–44, 2002.
- [8] Dmitry Budker and Michael Romalis. Optical magnetometry. Nature physics, 3(4):227–234, 2007.
- [9] Andrew D Ludlow, Martin M Boyd, Jun Ye, Ekkehard Peik, and Piet O Schmidt. Optical atomic clocks. Reviews of Modern Physics, 87(2):637, 2015.
- [10] Lincoln D Carr, David DeMille, Roman V Krems, and Jun Ye. Cold and ultracold molecules: science, technology and applications. New Journal of Physics, 11(5):055049, 2009.
- [11] John L Bohn, Ana Maria Rey, and Jun Ye. Cold molecules: Progress in quantum engineering of chemistry and quantum matter. Science, 357(6355):1002–1010, 2017.
- [12] David DeMille. Quantum computation with trapped polar molecules. Physical Review Letters, 88(6):067901, 2002.

- [13] SF Yelin, K Kirby, and Robin Côté. Schemes for robust quantum computation with polar molecules. Physical Review A, 74(5):050301, 2006.
- [14] Mallikarjun Karra, Ketan Sharma, Bretislav Friedrich, Sabre Kais, and Dudley Herschbach. Prospects for quantum computing with an array of ultracold polar paramagnetic molecules. The Journal of chemical physics, 144(9):094301, 2016.
- [15] Kang-Kuen Ni, Till Rosenband, and David D Grimes. Dipolar exchange quantum logic gate with polar molecules. Chemical science, 9(33):6830–6838, 2018.
- [16] Jacob A Blackmore, Luke Caldwell, Philip D Gregory, Elizabeth M Bridge, Rahul Sawant, Jesús Aldegunde, Jordi Mur-Petit, Dieter Jaksch, Jeremy M Hutson, BE Sauer, et al. Ultracold molecules for quantum simulation: rotational coherences in caf and rbcs. Quantum Science and Technology, 4(1):014010, 2018.
- [17] MS Safronova, D Budker, D DeMille, Derek F Jackson Kimball, A Derevianko, and Charles W Clark. Search for new physics with atoms and molecules. Reviews of Modern Physics, 90(2):025008, 2018.
- [18] David DeMille, John M Doyle, and Alexander O Sushkov. Probing the frontiers of particle physics with tabletop-scale experiments. Science, 357(6355):990–994, 2017.
- [19] Axel André, David DeMille, John M Doyle, Mikhail D Lukin, St Ex Maxwell, Peter Rabl, Robert J Schoelkopf, and Peter Zoller. A coherent all-electrical interface between polar molecules and mesoscopic superconducting resonators. Nature Physics, 2(9):636–642, 2006.
- [20] Andrea Micheli, GK Brennen, and Peter Zoller. A toolbox for lattice-spin models with polar molecules. Nature Physics, 2(5):341–347, 2006.
- [21] Roman V Krems. Cold controlled chemistry. Physical Chemistry Chemical Physics, 10(28):4079–4092, 2008.
- [22] N Balakrishnan. Perspective: Ultracold molecules and the dawn of cold controlled chemistry. The Journal of chemical physics, 145(15):150901, 2016.
- [23] Tetsu Takekoshi, Lukas Reichsöllner, Andreas Schindewolf, Jeremy M Hutson, C Ruth Le Sueur, Olivier Dulieu, Francesca Ferlaino, Rudolf Grimm, and Hanns-Christoph Nägerl. Ultracold dense samples of dipolar rbcs molecules in the rovibrational and hyperfine ground state. Physical review letters, 113(20):205301, 2014.
- [24] Peter K Molony, Philip D Gregory, Zhonghua Ji, Bo Lu, Michael P Köppinger, C Ruth Le Sueur, Caroline L Blackley, Jeremy M Hutson, and Simon L Cornish. Creation of ultracold rb 87 cs 133 molecules in the rovibrational ground state. Physical review letters, 113(25):255301, 2014.
- [25] Jee Woo Park, Sebastian A Will, and Martin W Zwierlein. Ultracold dipolar gas of fermionic na 23 k 40 molecules in their absolute ground state. Physical review letters, 114(20):205302, 2015.
- [26] Mingyang Guo, Bing Zhu, Bo Lu, Xin Ye, Fudong Wang, Romain Vexiau, Nadia Bouloufa-Maafa, Goulven Quéméner, Olivier Dulieu, and Dajun Wang. Creation of an ultracold gas of ground-state dipolar na 23 rb 87 molecules. Physical review letters, 116(20):205303, 2016.

- [27] JFE Croft, N Balakrishnan, and BK Kendrick. Long-lived complexes and signatures of chaos in ultracold  $k^+ + rb$  collisions. Physical Review A, 96(6):062707, 2017.
- [28] M-G Hu, Yu Liu, David D Grimes, Y-W Lin, Andrei H Gheorghe, Romain Vexiau, Nadia Bouloufa-Maafa, Olivier Dulieu, Till Rosenband, and K-K Ni. Direct observation of bimolecular reactions of ultracold  $krb$  molecules. Science, 366(6469):1111–1115, 2019.
- [29] Goulven Quemener and Paul S Julienne. Ultracold molecules under control! Chemical Reviews, 112(9):4949–5011, 2012.
- [30] Mikhail Lemeshko, Roman V Krems, John M Doyle, and Sabre Kais. Manipulation of molecules with electromagnetic fields. Molecular Physics, 111(12-13):1648–1682, 2013.
- [31] Jie Cui and Roman V Krems. Elastic and inelastic collisions of  $2\sigma$  molecules in a magnetic field. Physical Review A, 88(4):042705, 2013.
- [32] AV Gorshkov, P Rabl, G Pupillo, A Micheli, P Zoller, MD Lukin, and HP Büchler. Suppression of inelastic collisions between polar molecules with a repulsive shield. Physical review letters, 101(7):073201, 2008.
- [33] Giacomo Valtolina, Kyle Matsuda, William G Tobias, Jun-Ru Li, Luigi De Marco, and Jun Ye. Dipolar evaporation of reactive molecules to below the fermi temperature. Nature, 588(7837):239–243, 2020.
- [34] BC Regan, Eugene D Commins, Christian J Schmidt, and David DeMille. New limit on the electron electric dipole moment. Physical review letters, 88(7):071805, 2002.
- [35] Jacob Baron, Wesley C Campbell, David DeMille, John M Doyle, Gerald Gabrielse, Yulia V Gurevich, Paul W Hess, Nicholas R Hutzler, Emil Kirilov, Ivan Kozyryev, et al. Order of magnitude smaller limit on the electric dipole moment of the electron. Science, 343(6168):269–272, 2014.
- [36] Vitaly Andreev and NR Hutzler. Improved limit on the electric dipole moment of the electron. Nature, 562(7727):355–360, 2018.
- [37] William B Cairncross, Daniel N Gresh, Matt Grau, Kevin C Cossel, Tanya S Roussy, Yiqi Ni, Yan Zhou, Jun Ye, and Eric A Cornell. Precision measurement of the electron’s electric dipole moment using trapped molecular ions. Physical review letters, 119(15):153001, 2017.
- [38] Jonathan J Hudson, Dhiren M Kara, IJ Smallman, Ben E Sauer, Michael R Tarbutt, and Ed A Hinds. Improved measurement of the shape of the electron. Nature, 473(7348):493–496, 2011.
- [39] Huanqian Loh, Kevin C Cossel, MC Grau, K-K Ni, Edmund R Meyer, John L Bohn, Jun Ye, and Eric A Cornell. Precision spectroscopy of polarized molecules in an ion trap. Science, 342(6163):1220–1222, 2013.
- [40] K-K Ni, S Ospelkaus, MHG De Miranda, A Pe’Er, B Neyenhuis, JJ Zirbel, S Kotochigova, PS Julienne, DS Jin, and Jun Ye. A high phase-space-density gas of polar molecules. science, 322(5899):231–235, 2008.

- [41] Frauke Seeßelberg, Nikolaus Buchheim, Zhen-Kai Lu, Tobias Schneider, Xin-Yu Luo, Eberhard Tiemann, Immanuel Bloch, and Christoph Gohle. Modeling the adiabatic creation of ultracold polar 23 na 40 k molecules. Physical Review A, 97(1):013405, 2018.
- [42] Timur M Rvachov, Hyungmok Son, Ariel T Sommer, Sepehr Ebadi, Juliana J Park, Martin W Zwierlein, Wolfgang Ketterle, and Alan O Jamison. Long-lived ultracold molecules with electric and magnetic dipole moments. Physical review letters, 119(14):143001, 2017.
- [43] Luigi De Marco, Giacomo Valtolina, Kyle Matsuda, William G Tobias, Jacob P Covey, and Jun Ye. A degenerate fermi gas of polar molecules. Science, 363(6429):853–856, 2019.
- [44] Kyle Matsuda, Luigi De Marco, Jun-Ru Li, William G Tobias, Giacomo Valtolina, Goulven Quéméner, and Jun Ye. Resonant collisional shielding of reactive molecules using electric fields. Science, 370(6522):1324–1327, 2020.
- [45] Nicholas R Hutzler, Hsin-I Lu, and John M Doyle. The buffer gas beam: An intense, cold, and slow source for atoms and molecules. Chemical reviews, 112(9):4803–4827, 2012.
- [46] S Truppe, HJ Williams, NJ Fitch, M Hambach, TE Wall, EA Hinds, BE Sauer, and MR Tarbutt. An intense, cold, velocity-controlled molecular beam by frequency-chirped laser slowing. New Journal of Physics, 19(2):022001, 2017.
- [47] Stephen D Hogan, Michael Motsch, and Frédéric Merkt. Deceleration of supersonic beams using inhomogeneous electric and magnetic fields. Physical Chemistry Chemical Physics, 13(42):18705–18723, 2011.
- [48] Sebastiaan YT van de Meerakker, Hendrick L Bethlem, Nicolas Vanhaecke, and Gerard Meijer. Manipulation and control of molecular beams. Chemical reviews, 112(9):4828–4878, 2012.
- [49] Edvardas Narevicius and Mark G Raizen. Toward cold chemistry with magnetically decelerated supersonic beams. Chemical reviews, 112(9):4879–4889, 2012.
- [50] David Reens, Hao Wu, Alexander Aeppli, Anna McAuliffe, Piotr Wcisło, Tim Langen, and Jun Ye. Beyond the limits of conventional stark deceleration. Physical Review Research, 2(3):033095, 2020.
- [51] Hao Wu, David Reens, Tim Langen, Yuval Shagam, Daniela Fontecha, and Jun Ye. Enhancing radical molecular beams by skimmer cooling. Physical Chemistry Chemical Physics, 20(17):11615–11621, 2018.
- [52] Xing Wu, Thomas Gantner, Manuel Koller, Martin Zeppenfeld, Sotir Chervenkov, and Gerhard Rempe. A cryofuge for cold-collision experiments with slow polar molecules. Science, 358(6363):645–648, 2017.
- [53] MD Di Rosa. Laser-cooling molecules. The European Physical Journal D-Atomic, Molecular, Optical and Plasma Physics, 31(2):395–402, 2004.
- [54] Benjamin K Stuhl, Brian C Sawyer, Dajun Wang, and Jun Ye. Magneto-optical trap for polar molecules. Physical review letters, 101(24):243002, 2008.

- [55] JF Barry, DJ McCarron, EB Norrgard, MH Steinecker, and D DeMille. Magneto-optical trapping of a diatomic molecule. *Nature*, 512(7514):286–289, 2014.
- [56] S Truppe, HJ Williams, M Hambach, L Caldwell, NJ Fitch, EA Hinds, BE Sauer, and MR Tarbutt. Molecules cooled below the doppler limit. *Nature Physics*, 13(12):1173–1176, 2017.
- [57] Loïc Anderegg, Benjamin L Augenbraun, Eunmi Chae, Boerge Hemmerling, Nicholas R Hut- zler, Aakash Ravi, Alejandra Collopy, Jun Ye, Wolfgang Ketterle, and John M Doyle. Ra- dio frequency magneto-optical trapping of caf with high density. *Physical review letters*, 119(10):103201, 2017.
- [58] Alejandra L Collopy, Shiqian Ding, Yewei Wu, Ian A Finneran, Loïc Anderegg, Benjamin L Augenbraun, John M Doyle, and Jun Ye. 3d magneto-optical trap of yttrium monoxide. *Physical review letters*, 121(21):213201, 2018.
- [59] Shiqian Ding, Yewei Wu, Ian A Finneran, Justin J Burau, and Jun Ye. Sub-doppler cool- ing and compressed trapping of yo molecules at  $\mu$  k temperatures. *Physical Review X*, 10(2):021049, 2020.
- [60] Louis Baum, Nathaniel B Vilas, Christian Hallas, Benjamin L Augenbraun, Shivam Raval, Debayan Mitra, and John M Doyle. 1d magneto-optical trap of polyatomic molecules. *Physical review letters*, 124(13):133201, 2020.
- [61] Lawrence W Cheuk, Loïc Anderegg, Benjamin L Augenbraun, Yicheng Bao, Sean Burchesky, Wolfgang Ketterle, and John M Doyle.  $\lambda$ -enhanced imaging of molecules in an optical trap. *Physical review letters*, 121(8):083201, 2018.
- [62] L Caldwell, JA Devlin, HJ Williams, NJ Fitch, EA Hinds, BE Sauer, and MR Tarbutt. Deep laser cooling and efficient magnetic compression of molecules. *Physical review letters*, 123(3):033202, 2019.
- [63] DJ McCarron, MH Steinecker, Y Zhu, and D DeMille. Magnetic trapping of an ultracold gas of polar molecules. *Physical review letters*, 121(1):013202, 2018.
- [64] S Jurgilas, A Chakraborty, CJH Rich, L Caldwell, HJ Williams, NJ Fitch, BE Sauer, Matthew D Frye, Jeremy M Hutson, and MR Tarbutt. Collisions between ultracold molecules and atoms in a magnetic trap. *arXiv preprint arXiv:2101.01580*, 2021.
- [65] S Jurgilas, A Chakraborty, CJH Rich, BE Sauer, Matthew D Frye, Jeremy M Hutson, and MR Tarbutt. Collisions in a dual-species magneto-optical trap of molecules and atoms. *arXiv preprint arXiv:2104.09990*, 2021.
- [66] Loïc Anderegg, Lawrence W Cheuk, Yicheng Bao, Sean Burchesky, Wolfgang Ketterle, Kang- Kuen Ni, and John M Doyle. An optical tweezer array of ultracold molecules. *Science*, 365(6458):1156–1158, 2019.
- [67] Lawrence W Cheuk, Loïc Anderegg, Yicheng Bao, Sean Burchesky, S Yu Scarlett, Wolfgang Ketterle, Kang-Kuen Ni, and John M Doyle. Observation of collisions between two ultracold ground-state caf molecules. *Physical review letters*, 125(4):043401, 2020.

- [68] Loïc Anderegg, Sean Burchesky, Yicheng Bao, Scarlett S Yu, Tijs Karman, Eunmi Chae, Kang-Kuen Ni, Wolfgang Ketterle, and John M Doyle. Observation of microwave shielding of ultracold molecules. arXiv preprint arXiv:2102.04365, 2021.
- [69] Mark Yeo. The Laser Cooling and Magneto-Optical Trapping of the YO Molecule. PhD thesis, Citeseer, 2015.
- [70] Friedrich Hund. Allgemeine quantenmechanik des atom-und molekelbaues. In Quantentheorie, pages 561–694. Springer, 1933.
- [71] John Michael Brown, John M Brown, and Alan Carrington. Rotational spectroscopy of diatomic molecules. Cambridge University Press, 2003.
- [72] JL Dunham. The energy levels of a rotating vibrator. Physical Review, 41(6):721, 1932.
- [73] RF Curl Jr. The relationship between electron spin rotation coupling constants and g-tensor components. Molecular Physics, 9(6):585–597, 1965.
- [74] JM Brown, M Kaise, CML Kerr, and DJ Milton. A determination of fundamental zeeman parameters for the oh radical. Molecular Physics, 36(2):553–582, 1978.
- [75] MR Tarbutt, BE Sauer, JJ Hudson, and EA Hinds. Design for a fountain of ybf molecules to measure the electron’s electric dipole moment. New Journal of Physics, 15(5):053034, 2013.
- [76] EB Norrgard, DJ McCarron, MH Steinecker, MR Tarbutt, and D DeMille. Submillikelvin dipolar molecules in a radio-frequency magneto-optical trap. Physical review letters, 116(6):063004, 2016.
- [77] Timothy C Steimle and Jeffrey E Shirley. A molecular beam-optical stark study of the a  $2\pi-x$   $2\sigma$  band system of yo. The Journal of chemical physics, 92(6):3292–3296, 1990.
- [78] Carl L Chalek and James L Gole. Chemiluminescence spectra of sco and yo: Observation and analysis of the a  $2\delta-x$   $2\sigma+$  band system. The Journal of Chemical Physics, 65(7):2845–2859, 1976.
- [79] A Bernard, R Bacis, and P Luc. Fourier transform spectroscopy: Extensive analysis of the a $2ii-j$  x $2e+$  and b $2e+-j$  x $2e+$  systems of yttrium oxide. The Astrophysical Journal, 227:338–348, 1979.
- [80] A Bernard and R Gravina. The emission spectrum of yttrium monoxide-new rotational and vibrational results on the a $2pi-x2sigma+$  system. The Astrophysical Journal Supplement Series, 52:443–450, 1983.
- [81] Timothy C Steimle and Yahya Al-Ramadin. Fine and hyperfine structure in the x $2\sigma+$  state of gas-phase yttrium monoxide. Journal of molecular spectroscopy, 122(1):103–112, 1987.
- [82] RD Suenram, FJ Lovas, GT Fraser, and K Matsumura. Pulsed-nozzle fourier-transform microwave spectroscopy of laser-vaporized metal oxides: Rotational spectra and electric dipole moments of yo, lao, zro, and hfo. The Journal of chemical physics, 92(8):4724–4733, 1990.
- [83] Benoit Simard, Andrew M James, Peter A Hackett, and Walter J Balfour. On the a  $2\delta-x2\sigma+(0, 0)$  band of yo. Journal of Molecular Spectroscopy, 154(2):455–457, 1992.

- [84] J Hoeft and T Törring. The microwave rotational spectrum of  $x\ 2\sigma^+ y_0$ . Chemical physics letters, 215(4):367–370, 1993.
- [85] RR Reddy, Y Nazeer Ahammed, K Rama Gopal, P Abdul Azeem, and S Anjaneyulu. Rkrv potential energy curves, dissociation energies,  $\gamma$ -centroids and franck-condon factors of  $y_0$ , cro, bn, sco, sio and alo molecules. Astrophysics and space science, 262(2):223–240, 1998.
- [86] JW-H Leung, Tongmei Ma, and ASC Cheung. Cavity ring down absorption spectroscopy of the  $b2\sigma^+ \leftarrow x2\sigma^+$  transition of  $y_0$ . Journal of Molecular Spectroscopy, 229(1):108–114, 2005.
- [87] Deping Zhang, Qiang Zhang, Boxing Zhu, Jingwang Gu, Bingbing Suo, Yang Chen, and Dongfeng Zhao. High-resolution electronic spectra of yttrium oxide ( $y_0$ ): The  $d\ 2\ \sigma^+ \leftarrow x\ 2\ \sigma^+$  transition. The Journal of chemical physics, 146(11):114303, 2017.
- [88] Chaoqun Zhang, Hannah Korslund, Yewei Wu, Shiqian Ding, and Lan Cheng. Towards accurate prediction for laser-coolable molecules: relativistic coupled-cluster calculations for yttrium monoxide and prospects for improving its laser cooling efficiencies. Physical Chemistry Chemical Physics, 22(45):26167–26177, 2020.
- [89] S Truppe, M Hambach, SM Skoff, NE Bulleid, JS Bumby, RJ Hendricks, EA Hinds, BE Sauer, and MR Tarbutt. A buffer gas beam source for short, intense and slow molecular pulses. Journal of Modern Optics, 65(5-6):648–656, 2018.
- [90] Mark Yeo, Matthew T Hummon, Alejandra L Collopy, Bo Yan, Boerge Hemmerling, Eunmi Chae, John M Doyle, and Jun Ye. Rotational state microwave mixing for laser cooling of complex diatomic molecules. Physical review letters, 114(22):223003, 2015.
- [91] Matthew T Hummon, Mark Yeo, Benjamin K Stuhl, Alejandra L Collopy, Yong Xia, and Jun Ye. 2d magneto-optical trapping of diatomic molecules. Physical review letters, 110(14):143001, 2013.
- [92] Hsin-I Lu, Julia Rasmussen, Matthew J Wright, Dave Patterson, and John M Doyle. A cold and slow molecular beam. Physical Chemistry Chemical Physics, 13(42):18986–18990, 2011.
- [93] Frank Pobell. Matter and methods at low temperatures, volume 2. Springer, 2007.
- [94] Nicholas R Hutzler, Maxwell F Parsons, Yulia V Gurevich, Paul W Hess, Elizabeth Petrik, Ben Spaun, Amar C Vutha, David DeMille, Gerald Gabrielse, and John M Doyle. A cryogenic beam of refractory, chemically reactive molecules with expansion cooling. Physical chemistry chemical physics, 13(42):18976–18985, 2011.
- [95] JF Barry, ES Shuman, and D DeMille. A bright, slow cryogenic molecular beam source for free radicals. Physical Chemistry Chemical Physics, 13(42):18936–18947, 2011.
- [96] HC Hseuh, TS Chou, HA Worwetz, and HJ Halama. Cryosorption pumping of he by charcoal and a compound cryopump design for tsta. Technical report, Brookhaven National Lab., Upton, NY (USA), 1979.
- [97] Wesley C Campbell. Magnetic trapping of imidogen molecules. PhD thesis, Citeseer, 2008.
- [98] Eunmi Chae. Laser Slowing of CaF Molecules and Progress Towards a Dual-MOT for Li and CaF. 2016.

- [99] Loic Anderegg. Ultracold Molecules in Optical Arrays: From Laser Cooling to Molecular Collisions. PhD thesis, 2020.
- [100] RC Dye, RE Muenchausen, and NS Nogar. Laser ablation of  $\text{Y}_2\text{O}_3$  in an oxygen atmosphere. Chemical physics letters, 181(6):531–536, 1991.
- [101] Jack Ekin. Experimental techniques for low-temperature measurements: cryostat design, material properties and superconductor critical-current testing. Oxford university press, 2006.
- [102] Christopher J Foot et al. Atomic physics, volume 7. Oxford University Press, 2005.
- [103] DJ Wineland and H Dehmelt. Proposed  $1014\delta\nu/\nu$  laser fluorescence spectroscopy on  $\text{tl}^+$  mono-ion oscillator iii (side band cooling). Bull. Am. Phys. Soc, 20(4):637–637, 1975.
- [104] Theodor W Hänsch and Arthur L Schawlow. Cooling of gases by laser radiation. Optics Communications, 13(1):68–69, 1975.
- [105] David J Wineland and Wayne M Itano. Laser cooling of atoms. Physical Review A, 20(4):1521, 1979.
- [106] William D Phillips and Harold Metcalf. Laser deceleration of an atomic beam. Physical Review Letters, 48(9):596, 1982.
- [107] John V Prodan and William D Phillips. Chirping the light—fantastic? recent nbs atom cooling experiments. Progress in quantum electronics, 8(3-4):231–235, 1984.
- [108] Maurice Petzold, Paul Kaebert, Philipp Gersema, Mirco Siercke, and Silke Ospelkaus. A zeeman slower for diatomic molecules. New Journal of Physics, 20(4):042001, 2018.
- [109] Maurice Petzold, Paul Kaebert, Philipp Gersema, Timo Poll, Niklas Reinhardt, Mirco Siercke, and Silke Ospelkaus. Type-ii zeeman slowing: Characterization and comparison to conventional radiative beam-slowing schemes. Physical Review A, 98(6):063408, 2018.
- [110] Qian Liang, Wenhao Bu, Yuhe Zhang, Tao Chen, and Bo Yan. A general zeeman slower for type-ii transitions and polar molecules. arXiv preprint arXiv:1906.10797, 2019.
- [111] Graham P Greve, Baochen Wu, and James K Thompson. Laser cooling with adiabatic transfer on a raman transition. New Journal of Physics, 21(7):073045, 2019.
- [112] John P Bartolotta, Matthew A Norcia, Julia RK Cline, James K Thompson, and Murray J Holland. Laser cooling by sawtooth-wave adiabatic passage. Physical Review A, 98(2):023404, 2018.
- [113] John P Bartolotta, Jarrod T Reilly, and Murray J Holland. Speeding up particle slowing using shortcuts to adiabaticity. Physical Review A, 102(4):043107, 2020.
- [114] Alejandra Louise Collopy. A three-dimensional mot of yo towards narrow-line cooling. Ph. D. Thesis, 2018.
- [115] EL Raab, M Prentiss, Alex Cable, Steven Chu, and David E Pritchard. Trapping of neutral sodium atoms with radiation pressure. Physical Review Letters, 59(23):2631, 1987.



- [116] Kyle N Jarvis, JA Devlin, TE Wall, BE Sauer, and MR Tarbutt. Blue-detuned magneto-optical trap. Physical review letters, 120(8):083201, 2018.
- [117] Matthew Harvey and Andrew James Murray. Cold atom trap with zero residual magnetic field: The ac magneto-optical trap. Physical review letters, 101(17):173201, 2008.
- [118] MR Tarbutt and TC Steimle. Modeling magneto-optical trapping of caF molecules. Physical Review A, 92(5):053401, 2015.
- [119] Anne Cournol, Pierre Pillet, Hans Lignier, and Daniel Comparat. Bichromatic magneto-optical trapping for  $j \rightarrow j, j-1$  configurations. Physical Review A, 93(5):053423, 2016.
- [120] John F Barry. Laser cooling and slowing of a diatomic molecule. Technical report, YALE UNIV NEW HAVEN CT, 2013.
- [121] EB Norrgard, N Sitaraman, JF Barry, DJ McCarron, MH Steinecker, and D DeMille. In-vacuum scattered light reduction with black cupric oxide surfaces for sensitive fluorescence detection. Review of Scientific Instruments, 87(5):053119, 2016.
- [122] ED Erikson, DD Berger, and BA Frazier. A comparison of the outgassing characteristics of several solar absorbing coatings. Journal of Vacuum Science & Technology A: Vacuum, Surfaces, and Films, 3(3):1711–1714, 1985.
- [123] Sheldon M Smith and Richard V Howitt. Survey of material for an infrared-opaque coating. In Infrared, adaptive, and synthetic aperture optical systems, volume 643, pages 53–62. International Society for Optics and Photonics, 1986.
- [124] Paul J Kuzmenko, Daniel M Behne, T Casserly, W Boardman, D Upadhyaya, K Boinapally, M Gupta, and Y Cao. Hard infrared black coating with very low outgassing. In Advanced Optical and Mechanical Technologies in Telescopes and Instrumentation, volume 7018, page 701852. International Society for Optics and Photonics, 2008.
- [125] Bastian Engeser. A novel surface trapping apparatus for ultracold cesium atoms: and the investigation of an Efimov resonance. na, 2006.
- [126] Hamamatsu Photonics K.K. Photomultiplier tubes basics and applications. download from vendor site, 2007. 2007.
- [127] HJ Williams, S Truppe, M Hambach, L Caldwell, NJ Fitch, EA Hinds, BE Sauer, and MR Tarbutt. Characteristics of a magneto-optical trap of molecules. New Journal of Physics, 19(11):113035, 2017.
- [128] JA Devlin and MR Tarbutt. Three-dimensional doppler, polarization-gradient, and magneto-optical forces for atoms and molecules with dark states. New Journal of Physics, 18(12):123017, 2016.
- [129] MR Tarbutt. Magneto-optical trapping forces for atoms and molecules with complex level structures. New Journal of Physics, 17(1):015007, 2015.
- [130] K Liu and JM Parson. Laser fluorescence detection of nascent product state distributions in reactions of sc and y with o<sub>2</sub>, no, and so<sub>2</sub>. The Journal of Chemical Physics, 67(5):1814–1828, 1977.

- [131] DJ McCarron, EB Norrgard, MH Steinecker, and D DeMille. Improved magneto-optical trapping of a diatomic molecule. New Journal of Physics, 17(3):035014, 2015.
- [132] Wolfgang Petrich, Michael H Anderson, Jason R Ensher, and Eric A Cornell. Behavior of atoms in a compressed magneto-optical trap. JOSA B, 11(8):1332–1335, 1994.
- [133] Paul D Lett, Richard N Watts, Christoph I Westbrook, William D Phillips, Phillip L Gould, and Harold J Metcalf. Observation of atoms laser cooled below the doppler limit. Physical review letters, 61(2):169, 1988.
- [134] Jean Dalibard and Claude Cohen-Tannoudji. Laser cooling below the doppler limit by polarization gradients: simple theoretical models. JOSA B, 6(11):2023–2045, 1989.
- [135] J Dalibard, C Salomon, A Aspect, E Arimondo, R Kaiser, N Vansteenkiste, and C Cohen-Tannoudji. New schemes in laser cooling. Atomic Physics XI, page 199, 1989.
- [136] Matthias Weidemüller, Tilman Esslinger, Maxim A Ol’shanii, Andreas Hemmerich, and Theodor W Hänsch. A novel scheme for efficient cooling below the photon recoil limit. EPL (Europhysics Letters), 27(2):109, 1994.
- [137] Andrew T Grier, Igor Ferrier-Barbut, Benno S Rem, Marion Delehaye, Lev Khaykovich, Frédéric Chevy, and Christophe Salomon.  $\lambda$ -enhanced sub-doppler cooling of lithium atoms in d 1 gray molasses. Physical Review A, 87(6):063411, 2013.
- [138] JA Devlin and MR Tarbutt. Laser cooling and magneto-optical trapping of molecules analyzed using optical bloch equations and the fokker-planck-kramers equation. Physical Review A, 98(6):063415, 2018.
- [139] J Lim, JR Almond, MA Trigatzis, JA Devlin, NJ Fitch, BE Sauer, MR Tarbutt, and EA Hinds. Laser cooled ybf molecules for measuring the electron’s electric dipole moment. Physical review letters, 120(12):123201, 2018.
- [140] Ivan Kozyryev, Louis Baum, Kyle Matsuda, Benjamin L Augenbraun, Loic Anderegg, Alexander P Sedlack, and John M Doyle. Sisyphus laser cooling of a polyatomic molecule. Physical review letters, 118(17):173201, 2017.
- [141] B Sheehy, SQ Shang, P Van Der Straten, S Hatamian, and H Metcalf. Magnetic-field-induced laser cooling below the doppler limit. Physical review letters, 64(8):858, 1990.
- [142] Olivier Emile, Robin Kaiser, Christoph Gerz, Hartmut Wallis, Alain Aspect, and Claude Cohen-Tannoudji. Magnetically assisted sisyphus effect. Journal de Physique II, 3(12):1709–1733, 1993.
- [143] Edward S Shuman, John F Barry, and David DeMille. Laser cooling of a diatomic molecule. Nature, 467(7317):820–823, 2010.
- [144] Matthew H Steinecker, Daniel J McCarron, Yuqi Zhu, and David DeMille. Improved radio-frequency magneto-optical trap of srf molecules. ChemPhysChem, 17(22):3664–3669, 2016.
- [145] LR Liu, JD Hood, Yichao Yu, JT Zhang, NR Hutzler, Till Rosenband, and K-K Ni. Building one molecule from a reservoir of two atoms. Science, 360(6391):900–903, 2018.

- [146] David Reens, Hao Wu, Tim Langen, and Jun Ye. Controlling spin flips of molecules in an electromagnetic trap. Physical Review A, 96(6):063420, 2017.
- [147] Rudolf Grimm, Matthias Weidemüller, and Yurii B Ovchinnikov. Optical dipole traps for neutral atoms. In Advances in atomic, molecular, and optical physics, volume 42, pages 95–170. Elsevier, 2000.
- [148] Andrey Kobayakov, Michael Sauer, and Dipak Chowdhury. Stimulated brillouin scattering in optical fibers. Advances in optics and photonics, 2(1):1–59, 2010.
- [149] Richard G Smith. Optical power handling capacity of low loss optical fibers as determined by stimulated raman and brillouin scattering. Applied optics, 11(11):2489–2494, 1972.
- [150] Nelson Darkwah Oppong. TOWARDS A DEGENERATE FERMI GAS OF STRONTIUM-IN-AD OPTICAL LATTICE. PhD thesis, ETH Zurich, Switzerland.
- [151] A Mazurenko, Sebastian Blatt, F Huber, MF Parsons, CS Chiu, G Ji, D Greif, and Markus Greiner. Implementation of a stable, high-power optical lattice for quantum gas microscopy. Review of Scientific Instruments, 90(3):033101, 2019.
- [152] TA Savard, KM O’hara, and JE Thomas. Laser-noise-induced heating in far-off resonance optical traps. Physical Review A, 56(2):R1095, 1997.
- [153] G Janik, W Nagourney, and H Dehmelt. Doppler-free optical spectroscopy on the  $ba+$  monion oscillator. JOSA B, 2(8):1251–1257, 1985.
- [154] Sara Rosi, Alessia Burchianti, Stefano Conclave, Devang S Naik, Giacomo Roati, Chiara Fort, and Francesco Minardi.  $\lambda$ -enhanced grey molasses on the  $d\ 2$  transition of rubidium-87 atoms. Scientific reports, 8(1):1–9, 2018.
- [155] D Rio Fernandes, Franz Sievers, Norman Kretzschmar, Saijun Wu, Christophe Salomon, and Frédéric Chevy. Sub-doppler laser cooling of fermionic 40k atoms in three-dimensional gray optical molasses. EPL (Europhysics Letters), 100(6):63001, 2012.
- [156] A Kastberg, William D Phillips, SL Rolston, RJC Spreuw, and PS Jessen. Adiabatic cooling of cesium to 700 nk in an optical lattice. Physical review letters, 74(9):1542, 1995.
- [157] Jian Chen, J Greg Story, Jeffrey J Tollett, and Randall G Hulet. Adiabatic cooling of atoms by an intense standing wave. Physical review letters, 69(9):1344, 1992.
- [158] SR Wilkinson, CF Bharucha, KW Madison, Qian Niu, and MG Raizen. Observation of atomic wannier-stark ladders in an accelerating optical potential. Physical review letters, 76(24):4512, 1996.
- [159] Coherent. Mephisto lasers – ultra-low noise and narrow linewidth. download from vendor site, 2019. 2019.
- [160] MA Ali, J Moghaddasi, and SA Ahmed. Temperature effects in rhodamine b dyes and improvement in cw dye laser performance. Laser Chemistry, 11(1):31–38, 1991.
- [161] John P Bartolotta and Murray J Holland. Sawtooth-wave adiabatic passage in a magneto-optical trap. Physical Review A, 101(5):053434, 2020.

- [162] Alejandra L Collopy, Matthew T Hummon, Mark Yeo, Bo Yan, and Jun Ye. Prospects for a narrow line mot in yo. New Journal of Physics, 17(5):055008, 2015.

## Appendix A

### YO Molecular Structures and Spectroscopy

In this appendix, we show all the spectroscopies we've taken in the past few years. We modulated the detection beam frequency at kHz and collect the fluorescence by photon multiplier tube(PMT). The detection beam is perpendicular to the molecular beam to reduce the Doppler shift. The YO energy level have been shown in Figure 2.3 and the relevant constants have been detailed in [69, 78, 79, 80, 81, 82, 83, 84, 85, 86, 87, 88].

#### A.1 $X^2\Sigma^+ \rightarrow A^2\Pi_{1/2}$ Transition( $v=0$ )

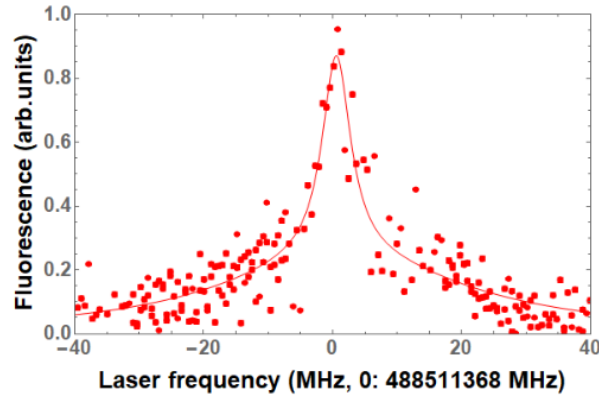


Figure A.1:  $X^2\Sigma^+ N=0(+)$   $G=F=0 \rightarrow A^2\Pi_{1/2} J'=1/2(-)$   $F'=0,1$  spectroscopy.  $F'=0$  and 1 are within the linewidth.

$X^2\Sigma^+ \rightarrow A^2\Pi_{1/2}$  is the main cycling transition for slowing, trapping and cooling. We choose  $X^2\Sigma^+ N=1(-) \rightarrow A^2\Pi_{1/2} J'=1/2(+)$  as our main cycling transition to prevent the rotational leakage [54].  $X^2\Sigma^+ N=2(+)$   $\rightarrow A^2\Pi_{1/2} J'=3/2(-)$  is chosen to decouple  $N=2$  from cycling transition.

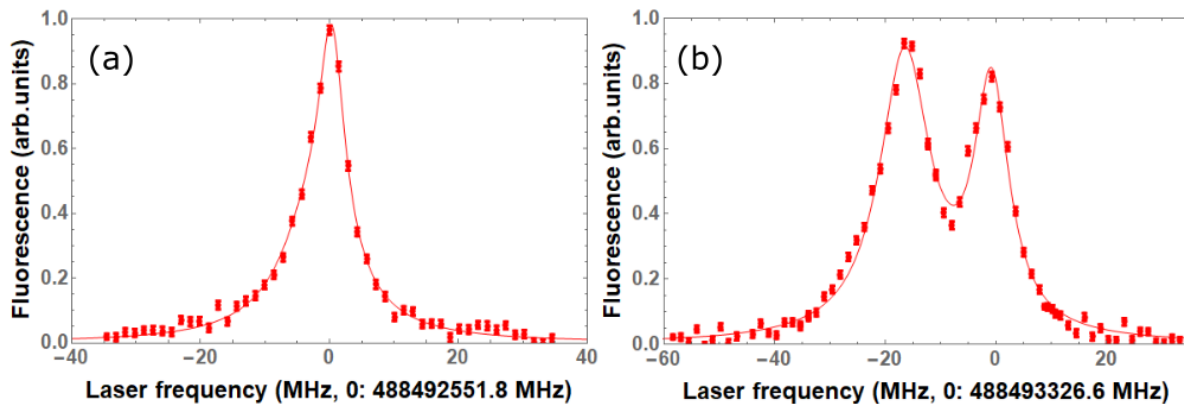


Figure A.2:  $X^2\Sigma^+ N=1(-) \rightarrow A^2\Pi_{1/2} J'=1/2(+)$  spectroscopy. (a).  $G=0 \rightarrow F'=0,1$ . (b).  $G=1 \rightarrow F'=0,1$ . The left peak is  $G=1, F=0 \rightarrow F'=0,1$

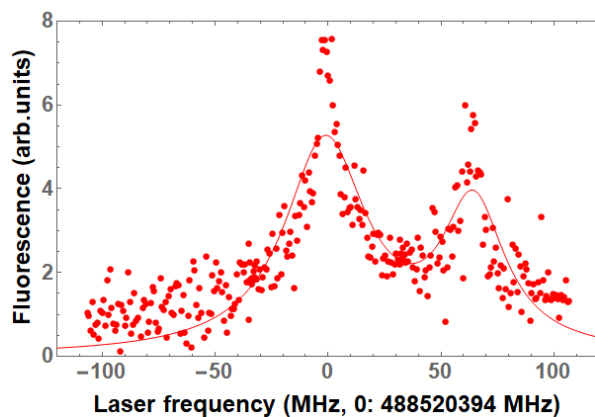


Figure A.3:  $X^2\Sigma^+ N=1(-) \rightarrow A^2\Pi_{1/2} J'=3/2(+)$  spectroscopy.  $G=0 \rightarrow F'=1,2$

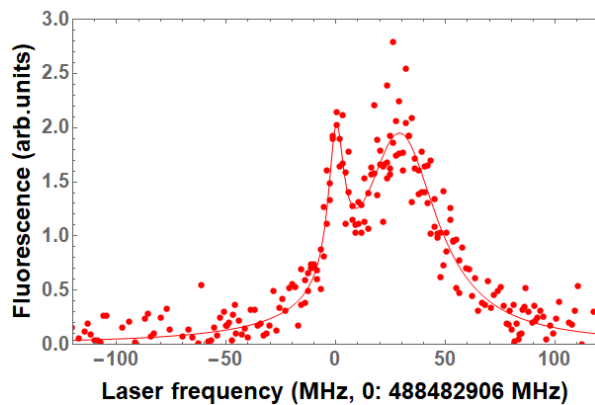


Figure A.4:  $X^2\Sigma^+ N=2(+)$  spectroscopy.  $G=0 \rightarrow F'=1,2$

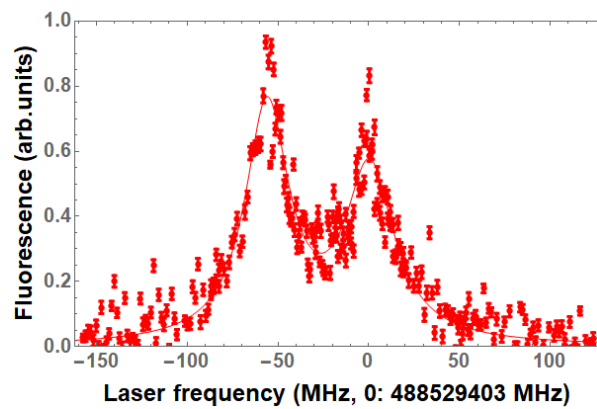


Figure A.5:  $X^2\Sigma^+ N=2(+)\rightarrow A^2\Pi_{1/2} J'=5/2(-)$  spectroscopy.  $G=0\rightarrow F'=2,3$

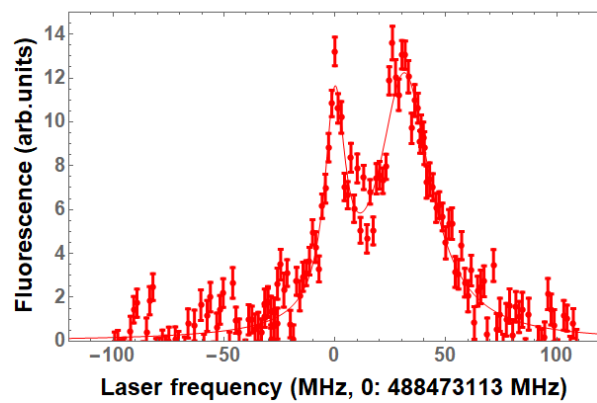


Figure A.6:  $X^2\Sigma^+ N=3(-)\rightarrow A^2\Pi_{1/2} J'=5/2(+)$  spectroscopy.  $G=0\rightarrow F'=2,3$

## A.2 $X^2\Sigma^+ \rightarrow A'^2\Delta_{3/2}$ Transition

Based on the initial calculation [78] and proposal [162], the  $A'^2\Delta_{3/2}$  has a narrow linewidth which can be used for further cooling. Therefore, we first determined the linewidth of  $A'^2\Delta_{3/2}$  by measuring the decay of the light induced fluorescence after switching off the laser light. We assume the fluorescence to decay exponentially and extract the lifetime to be  $23(2) \mu\text{s}$ . The linewidth is  $2\pi \times 6.9(6)$  kHz, much narrower than the previous calculation ( $2\pi \times 160$  kHz). Our measurement matches the most recent calculation [88]. This narrow linewidth can be used for narrowline cooling and SWAP cooling [111, 112, 161].

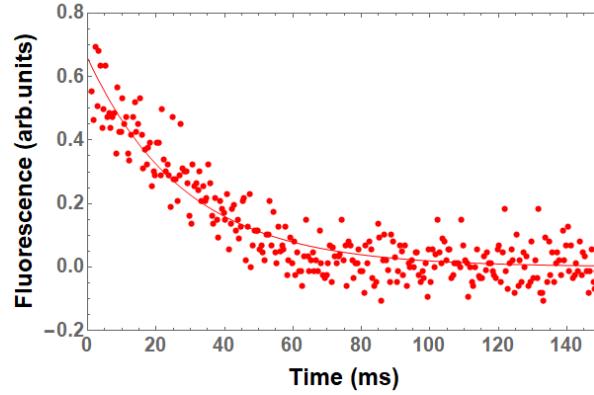


Figure A.7:  $A'^2\Delta_{3/2} J' = 3/2(-)$  lifetime. The decay lifetime from the exponential fit is  $23(2) \mu\text{s}$ .



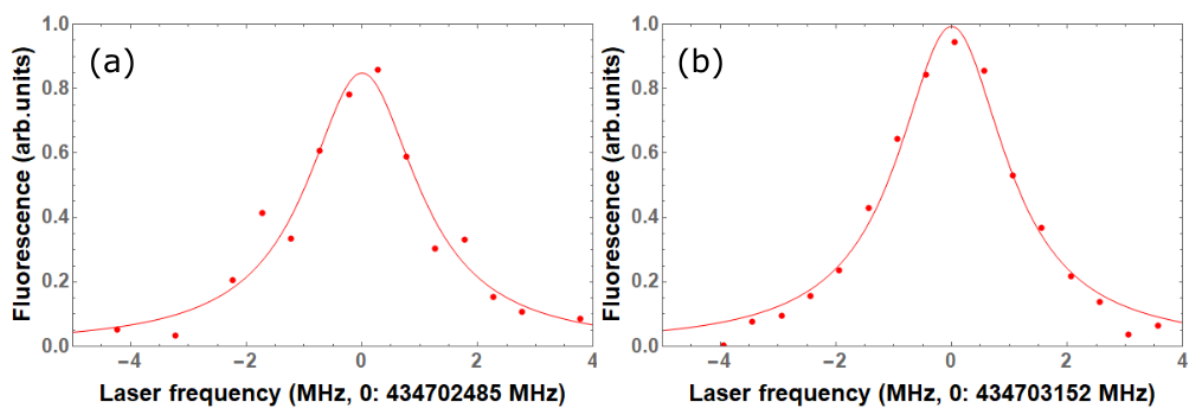


Figure A.8:  $X^2\Sigma^+ N = 0(+)$   $\rightarrow$   $A'^2\Delta_{3/2} J' = 3/2(-)$  spectroscopy. (a).  $N=G=F=0 \rightarrow F'=1$ . (b).  $N=0$   $G=F=1 \rightarrow F'=2$ .

## Appendix B

### Dye Lasers - How to Make it Happy

#### B.1 Why Dye Laser

Our main cooling transition  $X^2\Sigma^+ \rightarrow A^2\Pi_{1/2}$  is 614 nm. There is not any high power laser diode or amplifier system available at 614 nm. To generate high power at 614 nm, people need to amplify at 1228 nm and then double the frequency to get 614 nm. We have four different systems in our lab and each generates 1 watts of 614 nm laser, they are Raman fiber amplifier, solid state laser employing second harmonic generation, dye laser and SFG laser. The first three lasers are very expensive and each of them takes more than \$150k. The last SFG laser was purchased very recently from Precilasers at a much lower price. Currently we're testing its performance.

Raman fiber amplifier(MPB-Communications) takes a 20 mW 1228 nm seed from a home built ECDDL, then amplify to  $\sim 10$  W in a  $P_2O_5$  doped fiber pumped by a ytterbium fiber laser. Then, the 1228 nm light is frequency doubled to generate 1 W of 614 nm light. The entire system is fiber coupled and very robust in the experiment. This system generates the beams for slowing.

Another way is to amplify the 1228 nm light with tapered amplifier and then get 1228 nm light frequency doubled by a nonlinear crystal in a cavity. We bought an entire setup including seed, tapered amplifier, doubling crystal from Toptica photonics and it worked robustly. Currently it provides the beams for trapping and cooling. However, the tuning range of these lasers are typically limited to hundreds of GHz, which is too narrow to perform any broad tuning for spectroscopy measurement. A dye laser normally has a much broader tuning range than these two laser systems.

## B.2 Sirah Matisse DR 2 Laser

A dye laser uses an organic dye as the lasing medium. Compared to other lasers, dye laser offers exceptional tuning wavelength that is typically tens or even hundreds of nanometers. We use Rhodamine B mixed in ethylene glycol with a concentration of 0.57 g/L. It takes at least one hour for the dye to fully dissolve in the solvent. The dye is cooled to  $\sim 15^\circ\text{C}$  to lower the pumping threshold and increase the output power [160]. The cold temperature also changes the viscosity of the ethylene glycol and extend the shelf life. The dye runs through a slit nozzle at a pressure close to 15 bar, beyond which the turbulence introduces bubbles into the dye making the laser unstable.

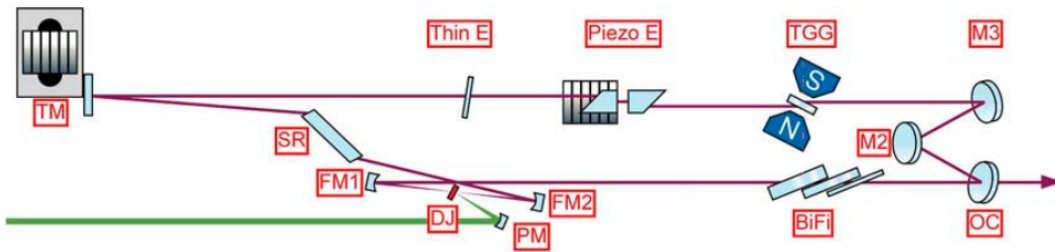


Figure B.1: A simplified optical layout of Sirah Dye laser. **PM**: Pump mirror(reflect and focus pump to dye jet). **DJ**: Thin slit dye jet. **FM**: Folding mirror(Bow-tie cavity mirror). **SR**: Rhombus crystal to displace the beam. **TM**: Tuning mirror(Big mirror used for slow feedback). **Thin E**: Thin etalon(A bandpass filter. A step motor controls the horizontal tilt angle of the etalon that control the transmission wavelength). **Piezo E**: Thick etalon(Thick etalon selects a single longitudinal mode from the spectral range that is determined by the configuration of output coupler, birefringence filter, and thin etalon. It's locked to the intensity maximum). **TGG**: Terbiu-Gallium-Garnet plate(Act as Faraday-rotator under a strong magnetic field. The combination of M2 and the TGG plate forms an optical diode supporting lasing in counter clockwise direction). **M3**: A small mirror used for fast feedback. **M2**: Out of plane mirror(This mirror transmits some light for locking the thick etalon and also forms an optical diode together with TGG plates). **OC**: Optical coupler(Transmits part of the beam and reflects the rest back into the ring cavity. The beam polarization is horizontal). **BiFi**: Birefringence filter(Coarse band pass filter). Image credit: Sirah.

The simplified layout of all optics is shown in Figure C.1. The laser is pumped by a 7 W of 532 nm light from a Coherent Verdi V-10, shown in green. The pump needs to be aligned parallel to the ring cavity and the polarization should be linear to match the lasing cavity. The ring cavity enables the lasing and the single frequency operation is achieved together with filters. The gain of Rhodamine B in ethylene glycol is tens of nm wide. The mirror sets and coating first limit the

lasing range to  $\sim 60$  THz. Then, the birefringence filters narrow the range down to  $\sim 200$  GHz. The free spectral range(FSR) of thin etalon, thick etalon and cavity are 250 GHz, 20 GHz and 160 MHz respectively. The single mode operation is maintained by locking the thick etalon to the maximum transmission of the longitudinal cavity mode. An optical diode is used to avoid lasing in both clockwise and counter clockwise directions. The beam propagating in clockwise direction suffers more loss at each brewster surfaces. In addition, the thick etalon is slightly tilted to suppress lasing in the clockwise direction. For normal operation, only M1(next to OC, not shown in the figure) and M3 should be tuned to optimize the laser output. If the ring cavity is pretty tilted, TM, M1 and M3 should be walked to make the cavity parallel to the baseplate. This is achieved by putting caps on FM1, FM2 and then adjust TM, M1, M3 to overlap the fluorescence spots propagating in both directions. After the rough alignment, we should remove the caps and adjust M1(or M3) to see the lasing behaviour. If the cavity is still tilted with respect to the baseplate, the thick etalon requires an out of cavity alignment. The entire process is documented in the manual. It is worth mentioning that although the ring cavity has an optical diode rejecting lasing in unwanted direction, an optical isolator should still be installed outside the cavity to prevent any reflection from entering the cavity. We observed that the reflection from the angled fiber tip affects the stability of the laser.

## Appendix C

### Magnetic Coil

The first generation of in-vacuum magnetic coil was described previously [114]. In the new design, we made the following changes:

- (1) We increased the coil aperture by  $\sim 30\%$ . This allows a larger MOT beam for trapping more molecules in our setup .
- (2) To maintain similar Q factor and magnetic field gradient( $\sim 10$  gauss/(cm·A)), we increased the number of turns to 12 on each coil.
- (3) An extra layer of copper is placed on the edge of the board to provide a better thermal conductance between boards.

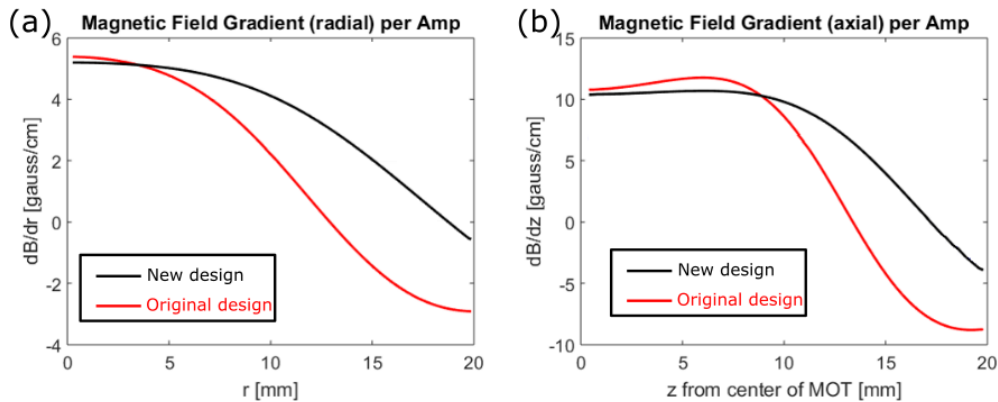
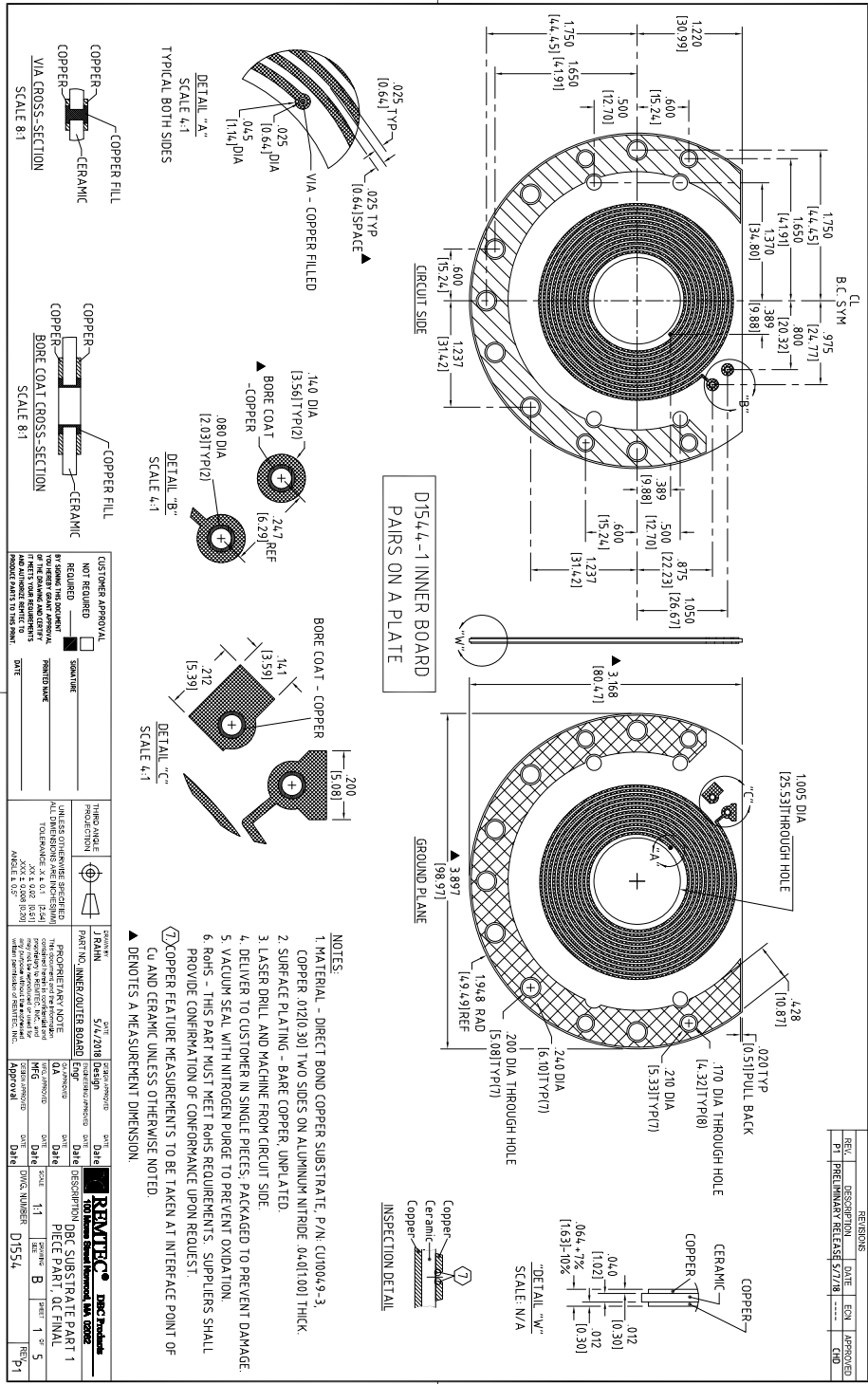


Figure C.1: Calculated coil performances. Two pairs of coils are used (four coil total), coil pairs are separated by  $\sim 30$  mm. The new coils provide better homogeneity based on the geometry.



REV	DESCRIPTION	DATE	EN	APPROVED
P1	PERMANENT RELEASE 5/17/8			

D1544 - 1 INNER BOARD  
PAIRS ON A PLATE

- NOTES:
1. MATERIAL - DIRECT BOND COPPER SUBSTRATE, P/N: CU0049-3, COPPER 0.07/0.300 TWO SIDES ON ALUMINUM NITRIDE 0.04/0.100 THICK.
  2. SURFACE PLATING - BARE COPPER, UNPLATED
  3. LASER DRILL AND MACHINE FROM CIRCUIT SIDE
  4. DELIVER TO CUSTOMER IN SINGLE PIECES, PACKAGED TO PREVENT DAMAGE.
  5. VACUUM SEAL WITH NITROGEN PURGE TO PREVENT OXIDATION.
  6. ROHS - THIS PART MUST MEET ROHS REQUIREMENTS, SUPPLIERS SHALL PROVIDE CONFIRMATION OF CONFORMANCE UPON REQUEST.
  7. COPPER FEATURE MEASUREMENTS TO BE TAKEN AT INTERFACE POINT OF CU AND CERAMIC UNLESS OTHERWISE NOTED.
- ▲ DENOTES A MEASUREMENT DIMENSION

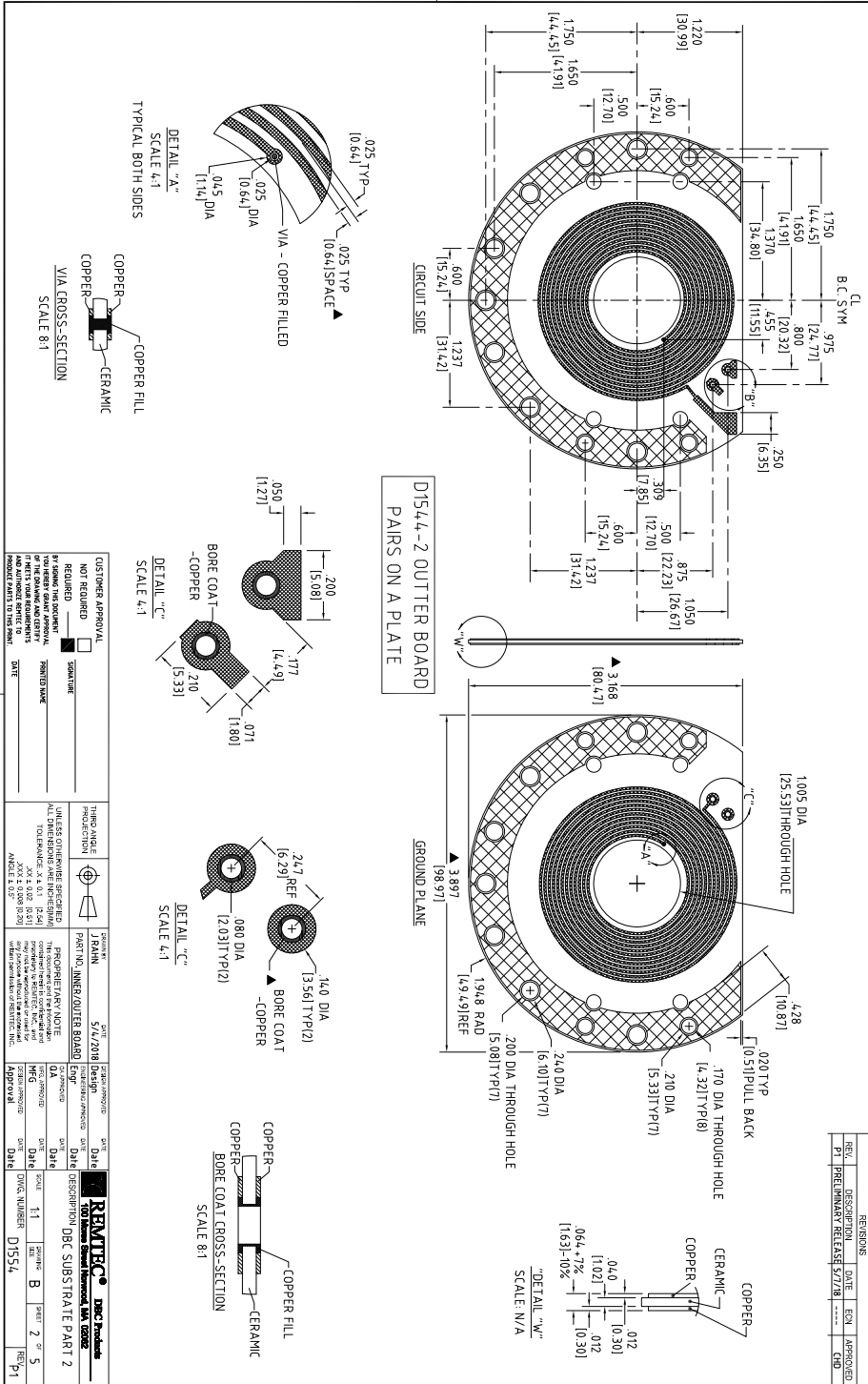
CUSTOMER APPROVAL	NOT REQUIRED	SIGNATURE
BY SIGNING THIS DOCUMENT I AGREE TO THE TERMS AND CONDITIONS OF THE DRAWING AND CERTIFY THAT THE PARTS MANUFACTURED HEREON SHALL BE IDENTICAL TO THE PARTS SHOWN ON THIS DRAWING AND SHALL BE IDENTICAL TO THE PARTS SHOWN ON THIS DRAWING.		

THIRD ANGLE PROJECTION	PRINTED NAME	DATE

DESIGN	DATE	SCALE	REV
JEBAN	5/17/2018	1:1	B

REVISIONS	DATE	EN	APPROVED
P1	5/17/2018		

REV	DESCRIPTION	DATE	EN	APPROVED
P1	PERMANENT RELEASE 5/17/8			



REV	DESCRIPTION	DATE	EN	APPROVED
F1	PERMANENT RELEASE 5/7/18			

REVISIONS

CUSTOMER APPROVAL	REQUIRED	SIGNATURE	DATE
NOT REQUIRED			
BY SIGNING THIS DOCUMENT I AGREE TO THE TERMS AND CONDITIONS OF THE DRAWING AND CERTIFY THAT I AM AWARE OF THE CONTENTS AND AM AUTHORIZED TO SIGN FOR THIS PART.	PRINTED NAME		DATE

THIRD ANGLE PROJECTION	APPROVED
UNLESS OTHERWISE SPECIFIED, ALL DIMENSIONS ARE IN INCHES AND DECIMALS THEREOF. ANGLES & 0.03"	DATE

DESIGNED BY	DATE	DESIGNED BY	DATE	DESIGNED BY	DATE
DESIGNED BY	DATE	DESIGNED BY	DATE	DESIGNED BY	DATE
DESIGNED BY	DATE	DESIGNED BY	DATE	DESIGNED BY	DATE
DESIGNED BY	DATE	DESIGNED BY	DATE	DESIGNED BY	DATE
DESIGNED BY	DATE	DESIGNED BY	DATE	DESIGNED BY	DATE
DESIGNED BY	DATE	DESIGNED BY	DATE	DESIGNED BY	DATE

RENTREC DMC Products	100
DESCRIPTION	DBC SUBSTRATE PART 2
SCALE	1:1
SCALE	8
SCALE	2
SCALE	5
SCALE	F1

The detailed drawings of new coil are shown above. There are two types of designs: inner and outer board. Care must be taken when assembling the coils. Two different pairs of coils are first assembled together to form the half of the entire assembly. A metal wire is used to connect the two board through the via. A hot plate is required for this process due to the high thermal conductance of the board. In order to avoid the unwanted shorting and arcing, a Kapton film is sandwiched between the coils. At the edge of the coils, an indium foil is sandwiched between coils to increase the thermal conductance at the joint. To mount the coil inside the chamber, we first machined the copper into a horseshoe shape. Each half of the coil assembly is mounted on this horseshoe copper and then attached to the copper cold fingers, as shown in Figure 5.2 (c). This configuration ensures the coil center is well overlapped with the center of the vacuum chamber. The top and bottom coil pairs are then connected outside the vacuum chamber, allowing both series and parallel connections. The only drawback of this configuration is the limited access due to the presence of cold fingers and electric feedthroughs, leaving a CF 2.75" vacuum flange on each side. This is undesired if a large pumping conductance or the collection efficiency is needed. Therefore, we came up with the second mounting scheme where all coils are installed on the single side of the flange, as shown in Figure 5.2 (d). In this configuration, the bottom coils are still mounted on the horseshoe copper but the top coils are supported by C-shape copper connectors. The C-shape is designed to leave the connectors away from the detection region. It is worth mentioning that the center of the current MOT coils is offsetted compared to the geometric center of the chamber. This is due to the mismeasurement of the copper finger length. Currently, we shift the center of the MOT by providing imbalanced currents into the coils. This should be fixed in the future since an imbalance field gradient would result in an asymmetric MOT shape.



## Appendix D

### Compression Timing Diagram

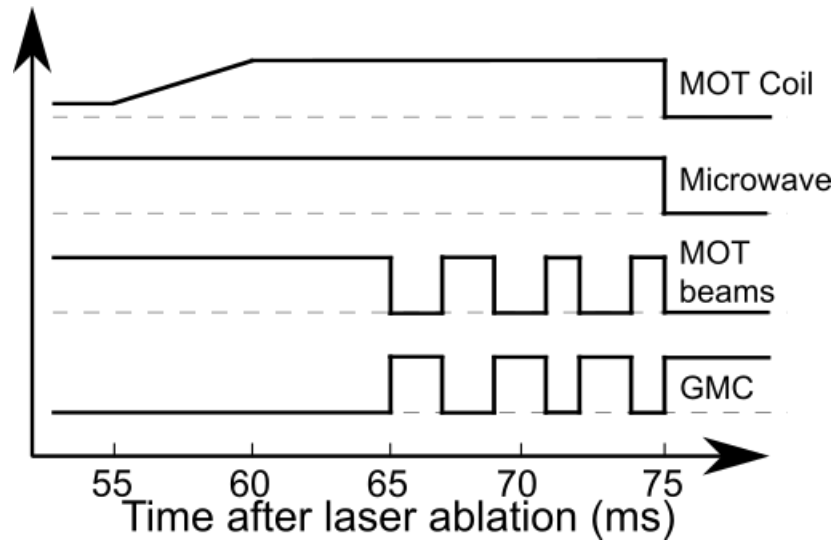


Figure D.1: Timing sequence for optimized compression of molecular clouds.

We repeat the GMC-MOT cycle three times after the initial 5 ms MOT hold pulse, as shown in Figure D.1. The GMC pulse is always set at 2 ms, and the MOT pulse follows 2 ms, 1 ms, and 1 ms. The decreasing MOT pulse duration accounts for the shrinking cloud after previous compression cycles. This timing sequence reduces the trapping volume by a factor of 10.

ProQuest Number: 28546441

INFORMATION TO ALL USERS

The quality and completeness of this reproduction is dependent on the quality and completeness of the copy made available to ProQuest.



Distributed by ProQuest LLC (2021).

Copyright of the Dissertation is held by the Author unless otherwise noted.

This work may be used in accordance with the terms of the Creative Commons license or other rights statement, as indicated in the copyright statement or in the metadata associated with this work. Unless otherwise specified in the copyright statement or the metadata, all rights are reserved by the copyright holder.

This work is protected against unauthorized copying under Title 17, United States Code and other applicable copyright laws.

Microform Edition where available © ProQuest LLC. No reproduction or digitization of the Microform Edition is authorized without permission of ProQuest LLC.

ProQuest LLC  
789 East Eisenhower Parkway  
P.O. Box 1346  
Ann Arbor, MI 48106 - 1346 USA